
THE UNIVERSITY *of* EDINBURGH

UNIVERSITY OF EDINBURGH

# Osmotaxis in *Escherichia coli*

Jerko Rosko

*A thesis submitted in fulfillment of the requirements*
*for the degree of Doctor of Philosophy*

*in the*

September 7, 2017

# Abstract

Bacterial motility, and in particular repulsion or attraction towards specific chemicals, has been a subject of investigation for over 100 years, resulting in detailed understanding of bacterial chemotaxis and the corresponding sensory network in many bacterial species including *Escherichia coli*.

*E. Coli* swims by rotating a bundle of flagellar filaments, each powered by an individual rotary motor located in the cell membrane. When all motors rotate counter-clockwise (CCW), a stable bundle forms and propels the cell forward. When one or more motors switch to clock-wise (CW) rotation, their respective filaments fall out of the bundle, leading to the cell changing orientation. Upon switching back to CCW, the bundle reforms and propels the cell in a new direction. Chemotaxis is performed by the bacterium through prolonging runs by suppressing CW rotation when moving towards nutrients and facilitating reorientation by increasing CW bias when close to a source of a harmful substance.

Chemicals are sensed through interaction with membrane bound chemosensors. These proteins can interact with a very specific set of chemicals and the concentrations they are able to sense are in the range between $10^{-6}$ and $10^{-2}$ M. However, experiments have shown that the osmotic pressure exerted by large ($> 10^{-1}$ M) concentrations of solutes, which have no specificity for binding to chemosensors (e.g. sucrose), is able to send a signal down the chemotactic network. Additionally, clearing of bacterial density away from sources of high osmolarity has been previously observed in experiments with agar plates. This behaviour has been termed osmotaxis.

The aim of this doctoral thesis work is to understand how different environmental cues influence the tactic response and ultimately, combine at the network output to direct bacterial swimming. As tactic responses to chemical stimuli have been extensively studied, I focus purely on the response to non-specific osmotic stimuli, using sucrose to elevate osmolarity. I monitor the chemotactic network output, the rotation of a single bacterial flagellar motor, using Back Focal Plane Interferometry over a variety of osmotic conditions. Additionally, in collaboration with Vincent Martinez, I studied the effect of elevated osmolality on swimming speed of large ($10^4$) bacterial populations, using differential dynamic microscopy (DDM).

I have found that sudden increases in media osmolarity lead to changes of both

motor speed and motor clockwise bias, which is the fraction of time it spends rotating clockwise. Changes in CW Bias proceed in two phases. Initially, after elevating the osmolarity, CW Bias drops to zero, indicating that the motor is exclusively in the 'cell run' mode. This phase lasts from 2-5 minutes depending on the magnitude of the change in solute concentration. What follows then is a distinct second phase where the CW Bias is elevated with respect to the initial levels and this phase lasts longer than 15-20 minutes. In comparison, for defined chemical stimuli, the motor output resets after several seconds, a behaviour termed perfect adaptation.

For changes of 100 mOsm/kg and 200 mOsm/kg in magnitude the motors speed up, often by as much as a factor of two, before experiencing a gradual slow down. Despite the slow down, motors still rotate faster 15-20 minutes after the change in osmolarity, than they did before. For changes of 400 mOsm/Kg in magnitude the motors decrease sharply in speed, coming to a near halt, recovering after 5 minutes and eventually, on average, speeding up. DDM studies of free swimming bacteria have shown that elevated osmolality leads to higher swimming speeds, in agreement with single motor data. Using theoretical models of bacterial swimming from the literature, it is discussed how this motor output, although different to what is expected for chemotaxis, is able to drive bacteria away from regions of space with high osmolalities.

Additionally, I have started extending the work done with sucrose, to another solute often used to elevate osmolality, sodium chloride. While sucrose is outer membrane impermeable, NaCl can cross the outer membrane into the periplasmic space. Another layer of complexity is that NaCl has some specificty for the chemoreceptors. The preliminary results are shown and qualitatively agree with those obtain with sucrose.

# Declaration

Except otherwise stated, the research undertaken in this thesis was the work of the author. Where work was done in collaboration with others, a significant contribution was made by the author. Collaborative work is indicated as such at the beginning of the relevant section.
Jerko Rosko

07. September 2017.

# Acknowledgements

I would like to thank my supervisor, Dr. Teuta Pilizota, for the assistance and guidance provided to me throughout this work. I would like to thank Dr. Vincent Martinez and Dr. Jana Schwartz-Linek and Prof. Wilson Poon for their help and collaboration on DDM experiments, Dr. Filippo Menolascina and Dr. Alex McVey for their comments on the text and members of the Pilizota group for the useful discussions, support and being a fun bunch of people to work with.

I would like to specially thank Tsveti for the therapy, the 5 am copy editing service and excursions into the exclusion zone. Ultimately, I am very grateful to my family and friends for their patience and support.

*"Satius est supervacua scire quam nihil."*

Seneca

# Contents

# Chapter 1

# Introduction

## 1.1 A rotary motor propels *Escherichia coli*

### 1.1.1 Structure of the motor

*Escherichia coli* is propelled through its environment by a rotating bundle of flagellar filaments. Each individual filament is driven by a rotary nano machine, the bacterial flagellar motor (BFM), embedded in the cell wall. BFMs are not unique to *E. coli* and drive flagella of many other bacteria, with varying degrees of structural similarity (Chen et al., 2011). Figure 1.1 B shows averaged cryo-electron microscopy tomograms of motors from several different species. Those of *E. Coli* and *Salmonella* have a very similar structure and, in literature, insights gained from the study of one are often applied to the other. On the other hand, they are significantly structurally different to motors of *Treponema* and *Borrelia*. Here I concentrate on the progress made understanding the BFM of *E. Coli*, supplementing with work done on *Salmonella*. When data obtained with motors of other species is used, I explicitly state so.
The dimension of an *E. Coli* motor is approximately 45 nm (Sowa et al., 2008; Chen et al., 2011) but the filament that is being driven by it can be as long as 10 $\mu$m. A schematic representation of the motor, taken from a recent publication is shown in Figure 1.1 A and a 3D partial reconstruction from cryo electron microscopy is presented in Figure 1.2. Like macroscopic mechanical motors, the BFM comprises a rotor and a stator. Additionally, it is a bidirectional motor, being able to drive its filament clockwise (CW) or counter clockwise (CCW) (Sowa et al., 2008).

The rotor structure consists of two rings, the cytoplasmic (C) ring and the membranous/supramembranous (MS) ring. The C ring (Francis et al., 1994) is a stack of 3 layers, each built from a different protein. Closest to the cytoplasm

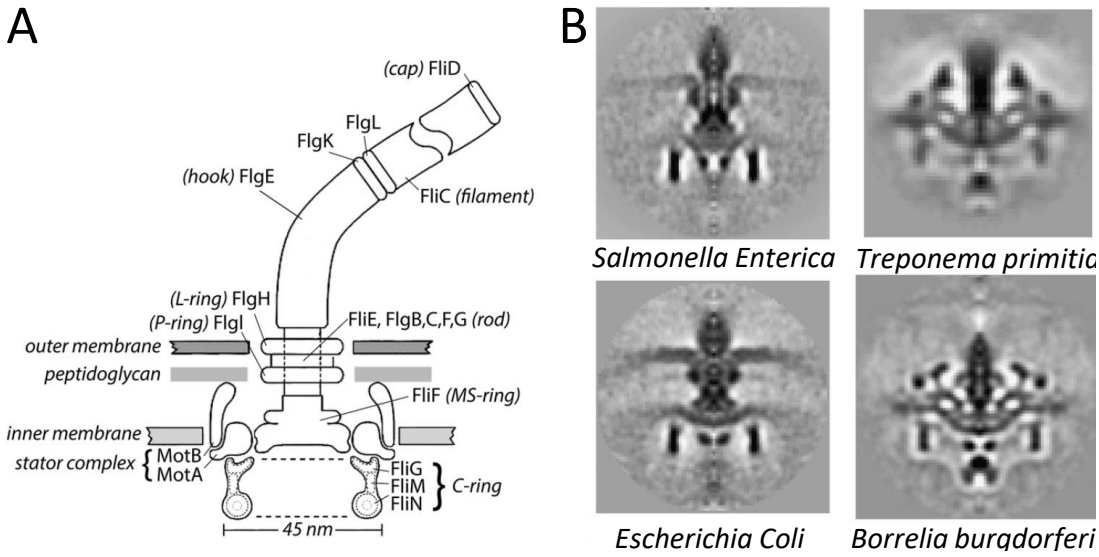


FIGURE 1.1: A: A sketch of the structure of the flagellar motor, reproduced from a recent publication (Hosu et al., 2016) B: Averaged Cryo Electron Microscopy Tomographs of BFM's in four different bacterial species (Chen et al., 2011).

is FliN, followed by FliM, interacting with each other in a $\mathrm{FliN}_4 - \mathrm{FliM}_1$ stoichiometry (Delalez et al., 2014). Electron microscopy studies have found that they have a 32-36 fold rotational symmetry (Thomas et al., 1999; Thomas et al., 2006), but a recent fluorescence microscopy study has found evidence for $28 \pm 4$ FliM molecules in the rotor when rotating clockwise and $36 \pm 6$ when rotating counter-clockwise (Delalez et al., 2014). Interestingly, the third layer of the C ring, composed of FliG, has the 24-26 fold (Levenson et al., 2012; Lynch et al., 2017) symmetry of the MS ring (Thomas et al., 2006; Suzuki et al., 2004). The MS ring, assembled on top of the C ring, is composed of $\sim 26$ copies of the protein FliF (Ueno et al., 1992; Suzuki et al., 2004). This ring sits in the inner membrane and partially extends into the periplasmic space. The rotary motion is transmitted via the rod to the hook (Fig 1.1 A) , the former being analogous to a drive shaft and the latter to a universal joint (Sowa et al., 2008). The hook can bend considerably, enabling filaments driven by motors all over the cell body to come together into a single bundle. Lodged in the inner membrane, around the MS ring, are the torque generating units of the flagellar motor (Sowa et al., 2008). These are known as the stator units and each is formed from two proteins, MotA and MotB, functioning together as a single unit in the $\mathrm{MotA}_4\mathrm{MotB}_2$ stoichiometry (Kojima et al., 2004).

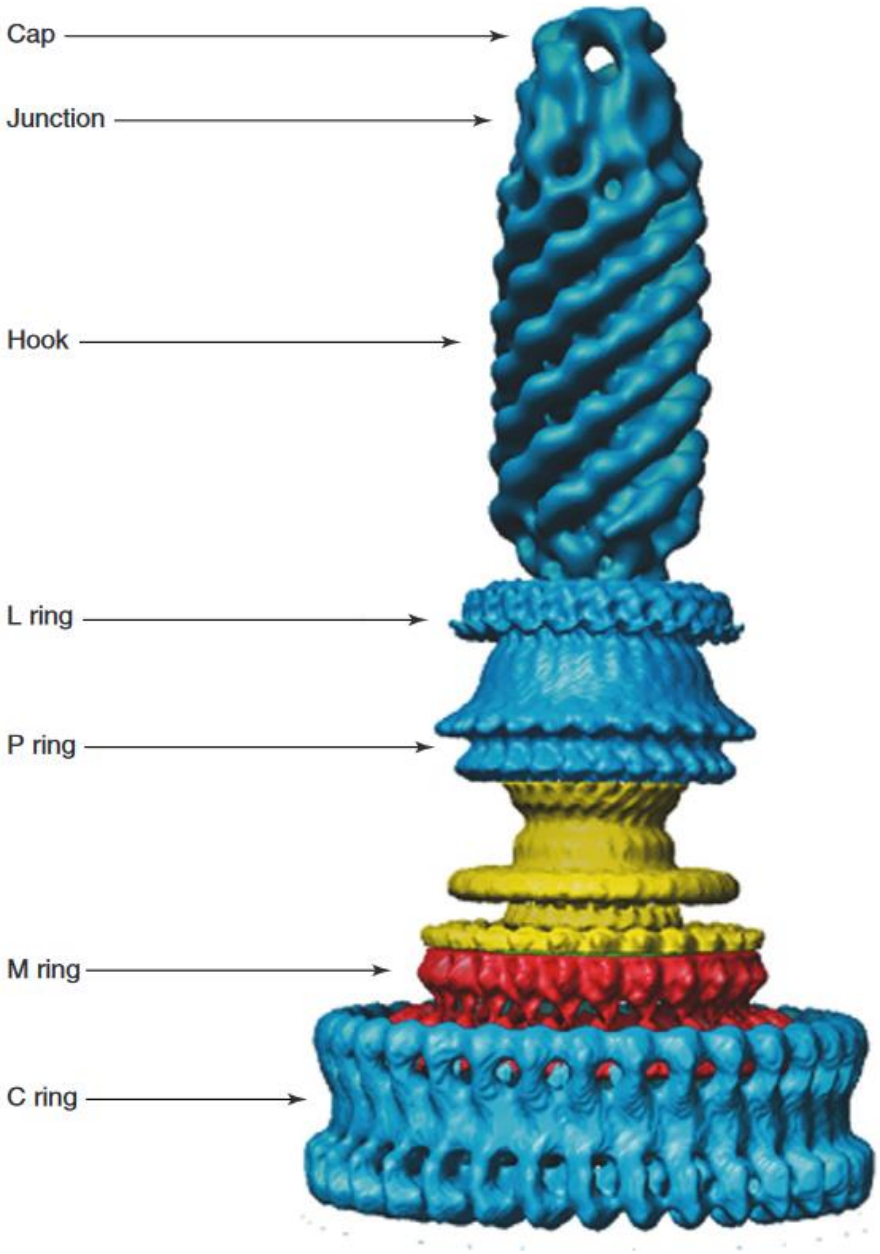


FIGURE 1.2: Electron microscopy 3D reconstruction of an isolated rotor of *Salmonella Typhimurium*. The strain used is a mutant which does not produce FliC, therefore there is no filament between the junction and the cap. (DeRosier, 2006)

### 1.1.2 Torque generation

#### An electrochemical potential fuels the force generators

An electrochemical potential drives ion flux through a channel on MotB (Braun et al., 2004), resulting in a conformational change in MotA, which leads to an interaction between the stator and FliG (Kojima et al., 2001; Sowa et al., 2008). This potential, the ion motive force (IMF)

$$IMF = V_m + \frac{k_B T}{q} \ln \frac{C_i}{C_o} \tag{1.1}$$

is the sum of membrane voltage ($\mathrm{V_m}$) and a term proportional to the ratio of concentration of the driving ion inside and outside the cell. In the latter term, $\mathrm{k_B}$ is the Boltzmann constant, $\mathrm{T}$ the temperature in degrees Kelvin, $\mathrm{C_i}, \mathrm{C_0}$ are the concentrations inside and outside and $\mathrm{q}$ is the charge. In the case of *E Coli*, the driving ions are protons and the potential is known as the proton motive force (PMF), which has a value of $\sim -140\mathrm{mV}$ for fully energized cells (Sowa et al., 2008). The speed of the BFM has been found to be proportional to PMF (Fig. 1.3 A) for both small and large loads (Gabel et al., 2003). However, work done on chimaeric *E. Coli* motors which incorporate $\mathrm{Na^+}$ driven stators from *Vibrio alginolyticus* has demonstrated a nonequivalence of $\mathrm{V_m}$ and the $\mathrm{Na^+}$ gradient as driving forces for the BFM at low loads (Lo et al., 2007). Keeping the external $\mathrm{Na^+}$ concentration, which corresponds to the second term in equation 1.1, fixed while changing $\mathrm{V_m}$ gives a linear relationship between motor speed and PMF. At high load, scanning the same range of $\mathrm{V_m}$ at different $\mathrm{Na^+}$ concentrations shifts the measured points up or down on the same line, indicating that both terms in equation 1.1 have the same proportionality factor to motor speed (Figure 1.3 B). However, at low loads, the points are not only shifted with changing $\mathrm{Na^+}$ concentration but are not on the same line. The slope changes as $\mathrm{C_{Na^+}}$ is changed, showing that the speed has distinct proportionality factors for each of the two terms of the PMF (Figure 1.3 C). Since the work of Gabel and Berg (Gabel et al., 2003) monitored both a large and a small load, it is unknown why they did not notice differences in proportionality, but they have not quantified relative contributions of $\mathrm{V_m}$ and the proton gradient in their experimental conditions.

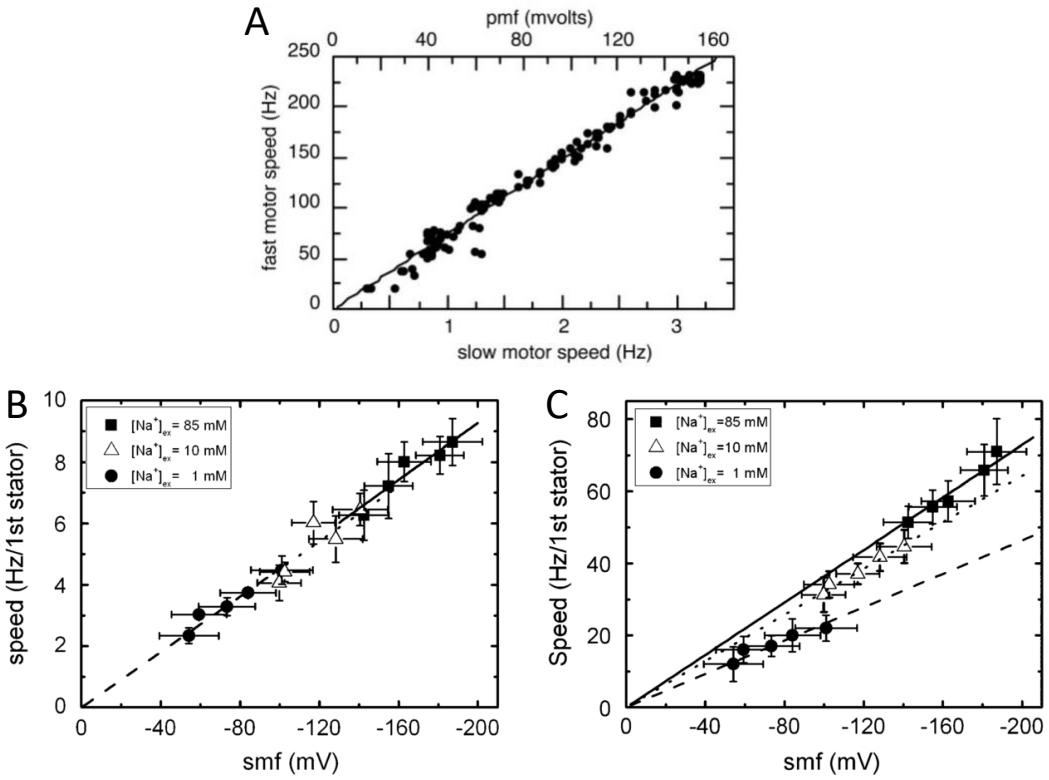


FIGURE 1.3: A: Experiment on a cell that has been tethered to the microscope cover glass with one flagellum and consequently the motor is driving the cell body, a high load. On the same cell, another flagellar motor is driving an 0.4 micron latex bead, a considerably lower load. PMF is gradually lowered using Sodium azide or carbonyl- cyanide m-chlorophenylhydrazone (CCCP) and both speeds are recorded. Previous work found a proportionality between high load speed and PMF controlled through membrane voltage (Fung et al., 1995). Thus, the slow speed is rescaled between 0 and 160 mV to yield an approximate PMF. The proportionality of slow speed to fast speed is then taken as evidence that speeds at low loads are proportional to PMF (Gabel et al., 2003). B and C are experiments where Lo et al. have independently varied the two components of the sodium motive force on sodium driven chimaeric motors (Lo et al., 2007). The membrane voltage was controlled through pH and the ion gradient, $pNa$, was controlled with three different external sodium concentrations. Panel B shows proportionality at high load and panel C shows that at low load, membrane voltage and ion gradient have different proportionality factors.

**relationship between torque and speed**

The torque-speed curve is a hallmark of performance characterization of mechanical motors and this method has been successfully applied to the bacterial flagellar motor. Being the product of the motor's internal mechanics, it often

serves as a gateway to finding out what lies *"under the hood"*. Almost all the information in the literature concerns the relationship between CCW speed and torque, possibly due to the wild type motor spending most of the time rotating CCW. Pioneering investigations of this relationship were conducted before it was known that motors can have a different number of stator units depending on the load they are driving (Lele et al., 2013; Tipping et al., 2013a). Therefore, it is possible that some of these curves include data from motors with different numbers of stator units, which could influence the shape of the relationship. These measurements revealed a motor characteristic with two distinct regimes, a low speed one where torque is relatively constant and a high speed regime where it monotonously decreases to zero (Fig. 1.4 A) (Berg et al., 1993a; Chen et al., 2000a). Although still not aware of the load dependence, Ryu et al. performed experiments on a strain with defective stator units while expressing functioning ones from a plasmid (Ryu et al., 2000). The experiment showed step increases in motor speed, attributed to gradual replacement of defective stators in a process called *"motor ressurection"* (Yuan et al., 2008; Reid et al., 2006; Ryu et al., 2000; Lele et al., 2013). Using this information they separated their data according to the number of stator units present. Resulting torque-speed relationships of motors with 1-5 stators provided evidence that the torque output of an N unit stator is approximately N times that of a single unit one (Fig. 1.4 B). More recent experiments have shown the torque-speed curve of a single stator chimaeric motor (Lo et al., 2013). Chimaeric motors are *E. Coli* motors with their native stator units replaced by $Na^+$ powered units from *Vibrio Algynoliticus*. The torque-speed curve is shown in Figure 1.4 D and does not have a very distinct plateau, except in the case of the highest sodium motive force.

While all the CCW characteristics have a concave-down shape of some sort, the CW characteristic appears to be a monotonously decreasing line, at least in the range between 60 and 300 Hz (Yuan et al., 2010), as shown in Figure 1.4 C. The asymmetry in the torque speed relationship is also accompanied by slower CW rotational speeds than their CCW counterparts when spinning faster than 60 Hz (Yuan et al., 2010), hinting that perhaps there is an intrinsic asymmetry in the way the BFM rotates. Some more evidence in favour of asymmetry comes from work on *E. Coli* with chimaeric motors (Sowa et al., 2005). In this study, it was discovered that the CCW rotation happens in steps of $13.7^o$ while

the CW step was $10.3^{o}$ but the authors noted that the difference could be attributed to their method, rather than to an underlying asymmetric mechanism in the BFM. More recent measurements with proton driven *Salmonella*, which are very similar to wild type *E. Coli* motors, revealed a CCW step of $14.4^{o}$ and a CW step of $13.5^{o}$ (Nakamura et al., 2010). This three times smaller discrepancy lead the authors to suggest that the elementary process of torque generation is symmetrical in CCW and CW rotation. A further argument for symmetry is made by Mandadapu et al. while constructing their model of torque generation based on currently available structural data (Mandadapu et al., 2015). Thus, the question of symmetry is still open and awaits further experimental evidence.

#### stator unit number fluctuates and depends on load

What makes replacing defective stators in resurrection experiments possible is that stator units are constantly associating and dissociating from the motor.By working with fluorescent MotB, Leake et al. found that a single $\mathrm{MotA_4MotB_2}$ complex remains bound to the BFM, on average, for $30$ seconds before returning to a pool of $\sim 100$ units floating in the membrane (Leake et al., 2006). The maximum number of stators connected to a wild type motor at any given time has been found to be 11-12 (Reid et al., 2006; Lele et al., 2013). Additionally, PMF and functional proton channels have been found necessary to keep stators bound to a motor and they remain so even if the motor is at stall torque, having no rotation (Tipping et al., 2013a; Tipping et al., 2013b). Furthermore, if the motor is not running at maximum stator number, it was shown to make use of stator turnover by integrating more torque generating units if the external load increases (Tipping et al., 2013a; Lele et al., 2013). Thus, stators act as mechanosensors.

#### stators deliver a contact force to the rotor

Up until recently, the small amount of information about the atomic level structure and interactions between the stator units and the rotor precluded proposing any physical mechanism of force transmission. While all major mathematical models of the last 10 years incorporate the conformational change within the stator as the event driving a single step in rotation, the details of how this change transmits force to the rotor have mostly been left vague (Nirody et al.,

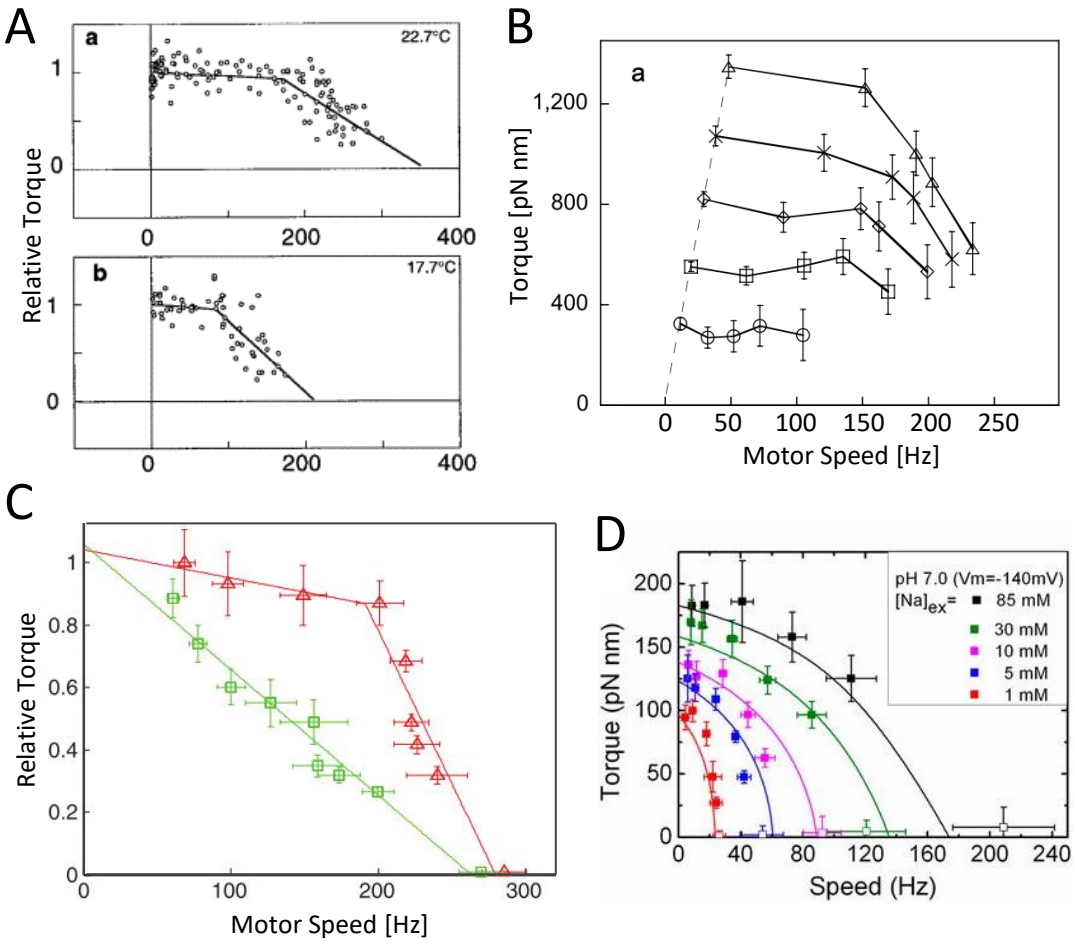


FIGURE 1.4: Various torque-speed curves. A: Curve for the proton driven bacterial flagellar motor of *Escherichia Coli* at 17.7°C (lower) and 22.7°C (upper) measured on motors without controlling for the number of stator units present. Adapted from (Chen et al., 2000a) B: Torque-speed curves of motors with 1 (lowest) to 5 (upper most) stator units . Stators were counted in " ressurection experiments" (Section 1.1.2) (Ryu et al., 2000) C: CCW (red) and CW (green) torque-speed curves for *E. Coli* motors without controlling for the number of stators. (Yuan et al., 2010) D: Torque-speed curves for single stator chimaeric ($Na^+$) driven motors in *E. Coli* at various values of sodium motive force, controlled through pNa by varying the external $Na^+$ concentration. (Lo et al., 2013)

2017). Only recently, a model was put forward that incorporates the current structural knowledge which, although incomplete, still allowed the authors to propose a plausible physical mechanism (Mandadapu et al., 2015). Central to the mechanism are the two Asp32 residues on the two MotB sub-units of a stator and two Pro173 residues located on two separate MotA sub-units on the cytoplasmic loops connecting helix bundles A2 and A3. These are illustrated on

Figure 1.5, panel A showing a schematic side view of a single MotA and MotB, explicitly showing the Asp32 proton binding site on MotB (Kojima et al., 2001) and the cytoplasmic loop of MotA that interacts with FliG. Panel B shows a top-down view of a whole $\mathrm{MotA_4MotB_2}$ unit. Only two MotA's are assumed active during rotation, the other two engage when the rotor flips geometry in order to rotate the other way (Mandadapu et al., 2015). The proposed motor power stroke is illustrated in Figure 1.5 C and proceeds as follows: Electrostatic interactions between charged residues position the stators with respect to the FliG part of the rotor ring (Zhou et al., 1998; Mandadapu et al., 2015). Ion channels on MotB open in the presence of a membrane potential allowing two protons to bind to negatively charged Asp32 residues. Re-organization of the hydrogen bonds in the vicinity of MotA's Pro173 residue induces elastic strain in the straight cytoplasmic loops, bending them. This physical motion of the loops delivers a steric (contact) force to FliG by one of the participating loops, making the first half of the power stroke. At the same time, the same strain induced change lowers the stator and exposes the ion binding pocket to the cytoplasm. This causes the proton to dissociate, inverting the strain and straightening the kink in the MotA loops. Thus, the loop on the second MotA delivers the second part of the power stroke to the FliG ring (Mandadapu et al., 2015).

This model reproduces the experimentally observed shape of the CCW torque-speed relationship. However, this is due to the separation of the mechanochemical cycle into two time scales (Meacci et al., 2009; Mandadapu et al., 2015; Nirody et al., 2017). One is the waiting time between the proton binding events and the other is the time required to complete a mechanical step. At high load and low speed mechanical step time is longer than the waiting time, while at low load and high speed the opposite is true. These timescales can be implemented regardless of the underlying mechanism and as a consequence most of recent models are able to reproduce the CCW torque-speed relationship (Meacci et al., 2009; Mandadapu et al., 2015; Nirody et al., 2017). The validation of this model thus awaits further comparisons with the wider body of experimental evidence.

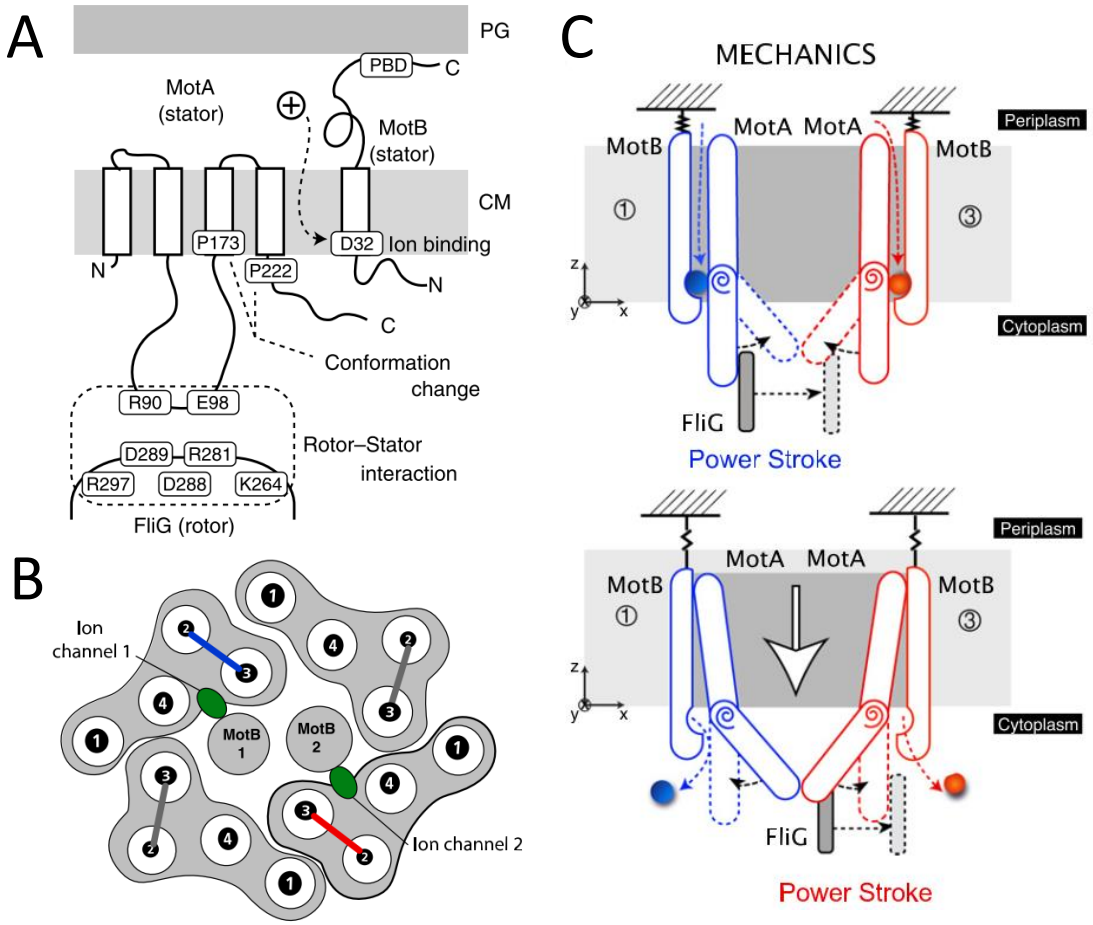


FIGURE 1.5: A: Schematic membrane section showing one MotA and one MotB unit and a part of the rotor (FliG). CM stands for cytoplasmic membrane and PG for peptidoglycan. MotA consists of four transmembrane helix bundles, while MotB comprises only one. Additionally both MotA and MotB contain cytoplasmic/periplasmic regions. The cytoplasmic loop of MotA is thought to interact with FliG and the Asp32 (D32) residue of MotB is involved in proton translocation. (Sowa et al., 2008). B: Schematic top view of a complete $\mathrm{MotA_4B_2}$ stator complex. Cytoplasmic loops are annotated between bundles 2 and 4 for each MotA and a putative ion binding site (D32) is shown as a green ellipse. (Mandadapu et al., 2015). C: Proposed model of a rotor power stroke outlined in Section 1.1.2 (Mandadapu et al., 2015)

### 1.1.3 The rotor and switching of direction of rotation

#### Conformation of the rotor biases the rotation

The ability of the rotor ring to spin both ways originates from a conformational change and thus altered geometry of interaction with the stator units. A helix in the C terminal domain of FliG has been shown to change position and orientation when FliG undergoes a conformational change that is thought to be the root of the transition from CCW to CW rotation (Lee et al., 2010). It was this repositioning that has led the authors of the recent power stroke model to propose that two out of four MotA units drive either direction of rotation (Mandadapu et al., 2015). Motor switches happen when phosphorylated CheY protein (CheY-P) interacts with the C ring, leading to the aforementioned conformational change in FliG. At this time, the exact details of the interaction are not known and both FliM and FliN have been implicated in the interaction (Toker et al., 1997; Sarkar et al., 2010). The BFM rotates predominantly CCW, with occasional switches to CW rotation (Bai et al., 2013). Switching is often quantified in terms of clockwise bias, a fraction of time spent spinning CW during a given interval. For an interval of length $\mathrm{T}$ seconds, it is measured how much of that was spent in the CW direction, yielding $T_{cw}$ and then the CW Bias is computed as

$$CW\,Bias = T_{cw}/T \tag{1.2}$$

In a population of wild type motors, the CW Bias exhibits a bi-modal distribution (Figure 1.6 A). The actual positions of the peaks can vary strain to strain and over experimental conditions but generally one is larger and at low bias, around 0.1 and the second peak, in the vicinity of 0.9, is much smaller.

#### Rotational Direction is Ultrasensitive to CheY-P Concentration

The motor has been found to possess a narrow operating range where the CW Bias is ultrasensitive to CheY-P concentration (Fig. 1.7 A). As can be seen from Figure 1.7 B, the range merely extends over a $\sim 2\mu\mathrm{M}$ span in concentration of CheY-P (Cluzel, 2000). This would mean that cells need to have a very precisely defined concentration of CheY-P so that the chemotactic network can effectively modulate the CW Bias in order to direct swimming. A cell with a baseline concentration of CheY-P of $\sim 4\mu\mathrm{M}$ would be seriously impaired in this regard. To make the steady state CW Bias insensitive to small variations

in this baseline concentration, which could happen due to strain differences or environmental factors, the rotor of the BFM undergoes adaptive remodelling (Branch et al., 2014). By integrating more FliM units into the C ring, the motor is able to place the current $\sim 4\mu\mathrm{M}$ CheY-P concentration into the sensitive operating range. This remodelling occurs on the time scale of minutes and has been shown to partially compensate for changes in the CheY-P baseline. Experimental data and modelling show that a motor rotating with a CW Bias of $\sim 0.8$ suddenly drops to $\sim 0.2$ when the internal CheY-P is changed by $\sim 0.5$ $\mu\mathrm{M}$ (Branch et al., 2014). The subsequent slow adaptation is not able to fully restore the original bias but only bring it back to $\sim$0.45. It should be noted that the experiments were performed in a strain with a naturally high CheY-P concentration and thus CW Bias. It has not been directly shown that these concentrations are in the most sensitive region of the dose-response curve. It could be possible that cells with wild type biases ($\sim 0.1$) could fully compensate for a $\sim$ 0.5 $\mu\mathrm{M}$ CheY-P increase. Additionally, the CheY-P concentrations were not empirically measured but were inferred from the dose-response curve measured elsewhere (Cluzel, 2000).

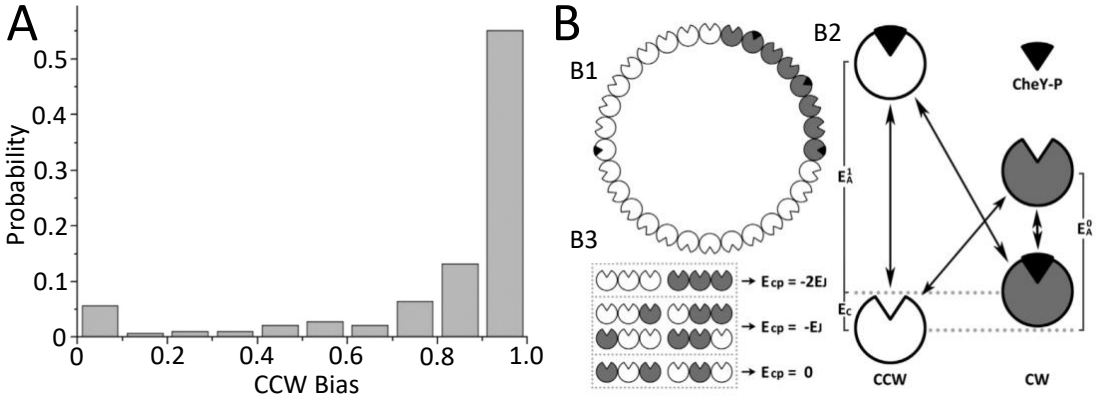


FIGURE 1.6: A: A distribution of CCW Biases for a strain derived from AW405 (chemotactic wild type), 281 cells were analysed. CCW and CW Bias are related by CCW+CW=1. Adapted from Bai et al. (Bai et al., 2013) B: The conformational spread model of BFM switching. Panel B1 shows the 34 site FliM/FliN ring to which CheY-P binds. Panel B2 shows the allowed transitions involving units in CCW and CW conformations and with CheY-P bound and un-bound. Panel B3 illustrates the basis for conformational spread where the transition barrier to the opposite state is lowered if a neighbor is already in that state. Adapted from Ma et al. (Ma et al., 2016).

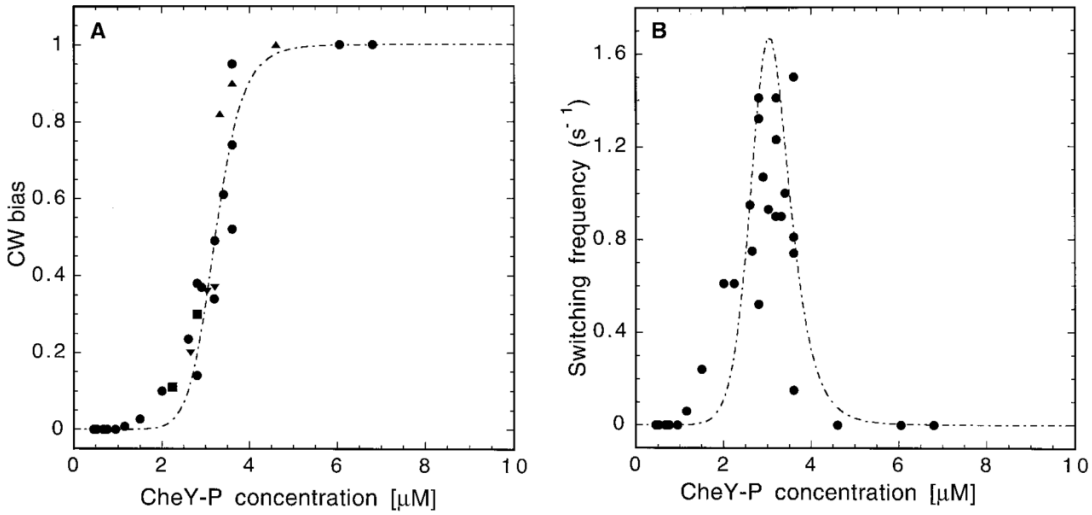


FIGURE 1.7: A: The dose response curve for CW Bias against CheY-P concentration. The concentration of fluorescently labelled CheY-P was quantified using Fluorescence Correlation Spectroscopy. Motor rotation was monitored using dark field microscopy while microspheres were attached to motors to make them visible. Each data point is a measurement in an individual bacterium. (Cluzel, 2000) B: The same measurement as in (A) just presented in terms of switching frequency (motor reversals per second), an alternate quantification of motor switching.(Cluzel, 2000)

**How many CheY-P's does it take to flip the rotor conformation?**

On average, $\sim$ 13, it turns out according to a recent experiment where GFP tagged CheY was imaged in living cells (Fukuoka et al., 2014). This is in contrast with the 34-fold periodicity of the FliM and FliN rings with which CheY-P has been shown to interact (Lee et al., 2010). This, and high resolution recordings of motor rotation, provide evidence for the conformational spread model of switching (Bai et al., 2010; Ma et al., 2016). In brief, it is assumed that the interaction of a single CheY-P with one of the $\sim$ 34 units of the C ring causes the said unit to flip to the CW conformation. Not all of the 34 sites need to be occupied because domains of CW conformation are able to spread along the ring. Figure 1.6 B1 shows the 34 unit ring. Units in the CW state are shaded in grey and CheY-P is shown as a black triangle. A free energy diagram, with all possible states and transitions of a single unit, is shown in Figure 1.6 B2. In brief, the free energy of conformational change is $\pm E_A^0$ when no CheY-P is bound and $\pm E_A^1$ when CheY-P is bound. Thus, binding of CheY-P makes the CW state energetically favourable. The basis for the conformational spread is presented

in Figure 1.6 B3. Units along the ring interact with a coupling energy $E_{cp}$. Having one neighbour in the opposite conformation increases the coupling energy, and having two neighbours in the opposite conformation further increases the coupling energy. Thus, binding of more CheY-P units increases the probability of the whole ring finding itself in the CW orientation.

The conformational spread model reproduces experimentally observed slowdowns, pauses, incomplete switches and ultrasensitivity to CheY and agrees with recent measurement of only $\sim 13$ CheY-P bound to the rotor during CW rotation (Ma et al., 2016). Taken together, these results favour the conformational spread model over other models of switching such as the Monod-Wyman-Changeux (MWC) model and the Koshland-Nemethy-Filmer (KNF) model (Ma et al., 2016).

#### A range of other factors influence the CW Bias

The dominant modifier of the CW Bias is CheY-P, which is under control of the chemotactic network, which actively directs swimming (Section 1.2). However, several other factors affect CW Bias to varying degrees at the level of the BFM itself, without any *"help"* from chemotaxis. One such mechanism, the remodelling of the FliM ring has already been described earlier when addressing the sensitivity of the CW Bias to CheY-P. Another way to affect bias is through changing the external load on the motor. It has been shown that as motors are increasingly loaded to slow them down below 50 Hz, the CW Bias starts rising through lengthening of the average CW interval. The motor torque over the 0-50 Hz range was estimated to vary only by 5%, leading the authors to rule out the torque as the signal (Fahrner et al., 2003). On the other hand, in the low load regime where the torque depends on speed, as the speed is increased by lowering the load, both CCW and CW intervals lengthen but without overall change to the CW Bias (Yuan et al., 2009). These results fit into the later discovered picture of stators as mechano-sensors for external load (Lele et al., 2013; Tipping et al., 2013a). Load is not the only variable that appears to be able to perturb the stator-rotor interaction to produce CW Bias changes. Recently FliL, a protein thought to sit between the stator unit and the FliF/FliG rings, has been shown to have strong interactions with the stator and cells lacking it are slower and have lower values in CW Bias (Partridge et al., 2015). Also, on the more extreme side of things, high hydrostatic pressure (>120MPa) was

observed to increase the number of motor switches to CW rotation, possibly by affecting the hydration of the C ring (Nishiyama et al., 2013).

## 1.2 The chemotactic network directs *E. coli* swimming

### 1.2.1 The network controls the BFMs through phosphorylation of CheY

Fluorescence microscopy images of the flagellar bundle that propels *Escherichia coli* cells are given in Figure 1.8 A-D. While all of the individual flagellar motors are driving their filaments CCW, the rotating bundle is stable and drives the cell forward. Individual motors stochastically switch their rotation to CW for brief periods of time (Bai et al., 2010), forcing their filaments out of the bundle. This leads to a situation illustrated on Figure 1.8 E, where the cell *"tumbles"* and undergoes a change in orientation. After the motor in question switches back to CCW direction, the respective filament rejoins the bundle and swimming resumes (Turner et al., 2000; Sowa et al., 2008). This kind of motion results in a random walk of the bacterial cell and Figure 1.9 illustrates this by showing three trajectories obtained by tracking single cells (Berg et al., 1972)

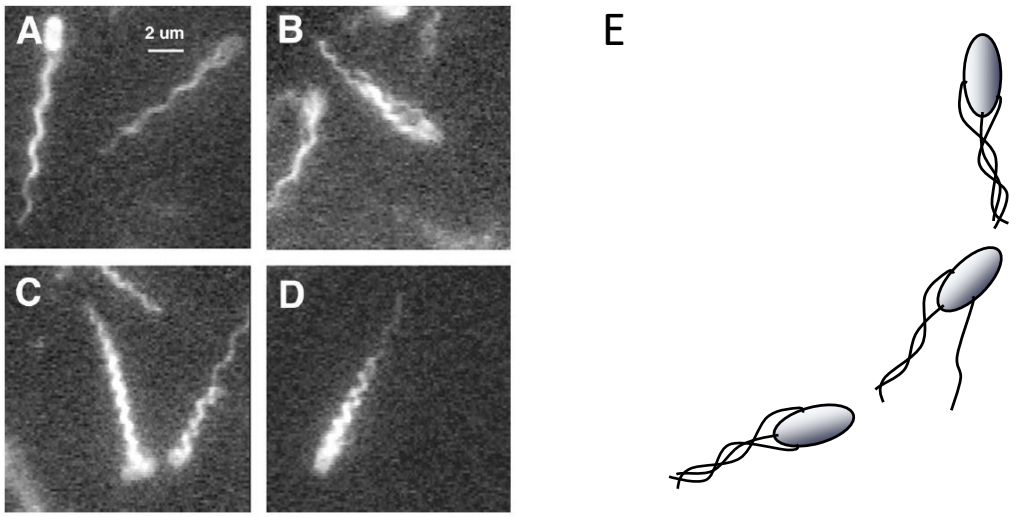


FIGURE 1.8: A: *Escherichia coli* cells with fluorescently labelled flagellar filaments, taken from (Turner et al., 2000). B: A cartoon showing a cell run interrupted by one of the flagellar motors switching to CW rotation, disrupting the bundle and causing a change in direction of swimming after the bundle reforms.

*Escherichia coli* navigates by biasing its random walk. By transiently elevating or lowering the cytoplasmic ratio of phosphorylated CheY (CheY-P) to

CheY, the chemotactic network is able to bias the random walk towards or away from very specific substances, termed attractants or repellents (Cluzel, 2000; Adler, 1975). A short list of some of the chemicals that *E. coli* can detect and are commonly used in experiments is given in Table 1.1.

The chemotactic network is a sensing and signalling network that can, by

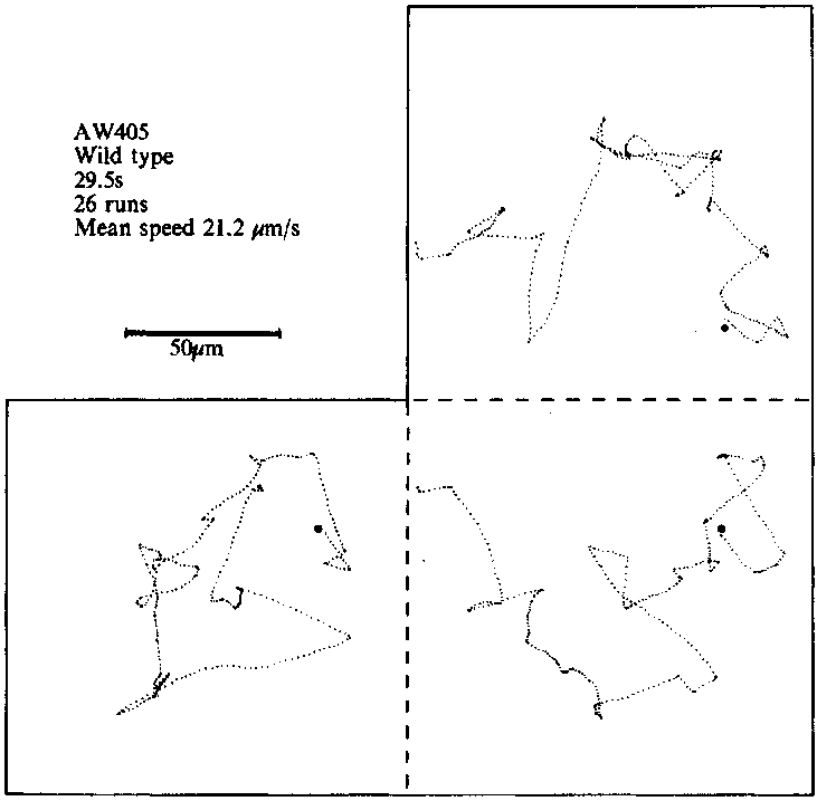


FIGURE 1.9: 3 tracks of *Escherichia coli* swimming recorded in a customised microscope specifically modified for tracking single cells. The strain used, AW405, is a wild type for chemotaxis.(Berg et al., 1972)

functionality, be broken down into three main components, membrane bound chemosensors, which serve as the input, a phosphorelay subsystem that transduces the signal and ultimately the BFM, the destination of the signal and the network output (Wadhams et al., 2004). In *E. Coli* there are five different membrane bound sensors, four methyl accepting chemotaxis proteins (MCPs) and one MCP like protein, termed Aer. The four MCPs span the inner membrane and extend into the cyto- and periplasm and sense specific chemicals in the extracellular environment either by binding them directly or indirectly, through periplasmic binding proteins (Wadhams et al., 2004). Aer is a transmembrane

TABLE 1.1: Some common attractants and repellents and their respective chemosensors. Glucose is not only sensed by an MCP protein but also by the phosphotransferase system, which then feeds the signal into the chemotactic network by interacting with the MCPs.

| Chemical | Receptor | Reference | |
|---|---|---|---|
| Aspartate | Tar | (Clarke et al., 1979) | Attr |
| $\alpha$-Me-Asp | Tar | (Clarke et al., 1979) | Attr |
| $Co^{2+}$ | Tar | (Reader et al., 1979) | Rep |
| $Ni^{2+}$ | Tar | (Reader et al., 1979) | Rep |
| Serine | Tsr | (Mesibov et al., 1972) | Attr |
| Acetate | Tsr | (Reader et al., 1979) | Rep |
| Indole | Tsr | (Reader et al., 1979) | Rep |
| D-Glucose | Trg<br>PTS* | (Adler et al., 1973; Kondoh et al., 1979)<br>(Lux et al., 1999; Neumann et al., 2012) | Attr |
| Dipeptides (eg. Gly-L-Leu) | Tap | (Manson et al., 1986) | Attr |

protein, structurally similar to MCP, that appears to be sensing oxygen concentration through the rate of respiratory electron transport (Bibikov et al., 2004). Most abundant MCP proteins in the cell, Tsr and Tar, are 5-10 times more numerous than the remaining two, Trg and Tap (Hazelbauer et al., 1981a; Hazelbauer et al., 1981b; Wang et al., 1982; Barnakov et al., 1998). Ligand specificities for the four MCP proteins are given in Table 1.1. This table lists common attractants and repellents that elicit strong responses from their respective sensors but is by no means complete. Several extensive surveys of chemotactically active chemicals have been made, although not many of the compounds have been accurately assigned a specific receptor (Mesibov et al., 1972; Adler et al., 1973; Tso et al., 1974).

An overview of the network architecture is given in Figure 1.10. The MCP forms a complex with CheW and CheA (Li et al., 2004). CheA is a histidine protein kinase that phsophorylates CheY-P using ATP as a phosphodonor (Hess et al., 1988). To examine the sequence of events in the signalling cascade let us assume that a repellent has bound to the MCP. When this happens, a signal is transmitted through the MCP-CheW-CheA complex through structural changes, promoting the 'ON' state of CheA (Parkinson et al., 2015). This leads to an increased phosphorylation of CheY, which then diffuses to the BFM, where it initiates cell reorientations (Sarkar et al., 2010). Meanwhile, CheZ, a phosphatase, begins dephosphorylating CheY-P and is able to terminate the

CheY-P signal within $\sim$ 200 $-$ 400ms (Sagawa et al., 2014; Wadhams et al., 2004). Without this mechanism, the lifetime of CheY-P would be $\sim$ 20s (Wadhams et al., 2004). Moreover, CheA not only phosphorylates CheY but also CheB, a methyesterase. CheB removes methyl groups from defined sites on the MCP protein, rendering it less sensitive to ligand binding and thus shifting the sensor operating range in case of persistent stimulus, like a permanent shift in background concentration. Another protein, CheR, a methyltransferase, methylates the the chemoreceptor, which increases its sensitivity if the repellent levels are low (Kehry et al., 1984; Kehry et al., 1985). These two mechanisms are important for keeping the steady state CheY-P concentration in the narrow operating range of the bacterial flagellar motor (Cluzel, 2000). The time scales of receptor methylation and demethylation are at least several seconds, an order of magnitude longer than the CheY-P signal termination time. This is addressed in more detail in Section 1.2.3.

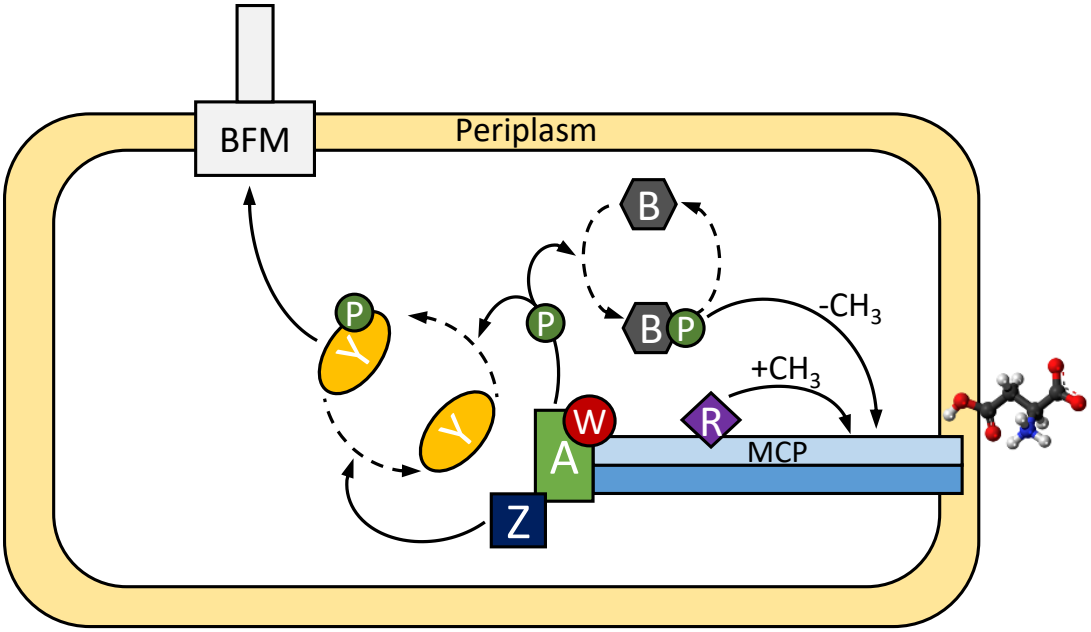


FIGURE 1.10: Overview of the chemotactic network components, drawn using information from (Wadhams et al., 2004).

To illustrate what the above described sequence of event means in terms of cell swimming, let's assume that the initial receptor stimulation by a repellent was a consequence of the bacterium transitioning from a region of lower concentration to a region of higher concentration of some repelling substance. This could, for example, be a part of an acetate gradient (Tso et al., 1974). Upon

detection of an increase in concentration, there will be a rise in CheA activity, ultimately manifesting itself in a transient jump in intracellular CheY-P concentration and, consequently, a short lived increase in CW Bias, leading to a couple of reorientation events. Let us assume that, unluckily, this time the cell was served with a direction that does not lead it out of the elevated repellent region. While this was happening, the slower kinetics of receptor demethylation caught up and the network had adjusted its sensitivity to the new background concentration of ligands, desensitising the receptors and accepting the new environment as the background concentration. Eventually, by nature of random walk, the cell will cross again into the region of lower repellent concentration, suddenly having its receptors less stimulated. Because methylation may take several seconds, the receptors are going to spend this time in the state of reduced sensitivity. Combined with reduced stimulation, CheY-P levels are going to be lower, and the cell run will prolong into the low concentration region. Soon after, methylation is complete and CheY-P, and thus CW Bias levels are once again in the steady state. The difference between these two time scales is essential for successful navigation of gradients by bacterial cells as it enables *E. coli* to perform temporal comparisons between the concentration of a chemical it has encountered a “moment ago" and the one it is experiencing right now, constituting a short term “memory" (Vladimirov et al., 2009).

### 1.2.2 Structure and membrane organisation of the chemosensors

Structurally, MCPs are homodimers formed of two protomers, composed of $\alpha$-helical segments (Fig. 1.11 A). It is thought that a $\sim$ 2 Å inward piston movement in one of the TM2 transmembrane helices is crucial for signalling. This movement occurs following attractant binding to one of the sites in the periplasmic ligand binding domain. This could lead to structural changes in the control cable that connects the TM2 domain and the HAMP domain, and thus affect the HAMP region in a way that disrupts kinase activity, consequently rendering the MCP unable to phosphorylate CheY (Parkinson et al., 2015).

Homodimers of MCPs are further organised into mixed trimers of dimers (Studdert et al., 2004; Li et al., 2004). Together with a CheA dimer and a CheW monomer, they comprise the sensory “core complex" (Li et al., 2004). Only

the most abundant MCPs ,Tar and Tsr, have the NWETF motif required for docking with CheR and CheB, illustrated on Figure 1.11 A. Participation of Trg and Tap in mixed clusters therefore brings them in proximity with Tar and Tsr and enables the regulation of their sensitivity by methylation (Barnakov et al., 1998; Feng et al., 1999; Wu et al., 1996). Trimers of dimers further arrange into hexagonal complexes (Figure 1.11 B), which then form even larger arrays composing thousands of proteins (Briegel et al., 2012; Greenfield et al., 2009). Interestingly, CheZ, the CheY-P signal terminator has been found to co-localise with the receptor arrays (Cantwell et al., 2003).
Ligand occupancy of one MCP dimer has been linked to an amplification of CheA kinase activity expected from an occupancy of $\sim 35$ (Sourjik et al., 2002). Subsequent work suggests that this high gain is a consequence of long range cooperative interactions between receptors in large sensory arrays (Sourjik et al., 2004; Parkinson et al., 2015). These arrays have been found, in *E. coli*, to be largest at the cell poles with additional smaller lateral clusters (Kentner et al., 2006; Greenfield et al., 2009). An example of cluster positioning is shown in Figure 1.11 C.
Another contribution to the gain of the chemotactic network is a factor of $\sim 10$ introduced at the output, at the level of the BFM. The ultrasensitivity of the CW Bias to the concentration of CheY-P (Cluzel, 2000) brings the total gain to a factor of $\sim 100$ (Vladimirov et al., 2009). A remarkable consequence of such high gain is the ability of the cell to respond to a concentration of aspartate as low as 3nM (Mao et al., 2003). If we take a 0.1 $\mu$m thick shell around a hypothetical cell, approximated by a cylinder of 2 $\mu$m in height and 1 $\mu$m in width, a concentration of 3nM amounts to only $\sim 2$ molecules in this volume.

### 1.2.3 Characteristics of chemotactic adaptation

Adaptation to persisting stimuli is one of the defining characteristics of the chemotactic network. It enables keeping of CheY-P levels in the sensitive range of the BFM (Cluzel, 2000), over a range of external ligand concentrations, spanning orders of magnitude, from the nanomolar to the millimolar range (Mao et al., 2003; Neumann et al., 2014). Adaptation has been characterized in terms of network activity, using a FRET assay where the green fluorescent protein and the yellow fluorescent protein have been fused to CheY and its phosphatase,

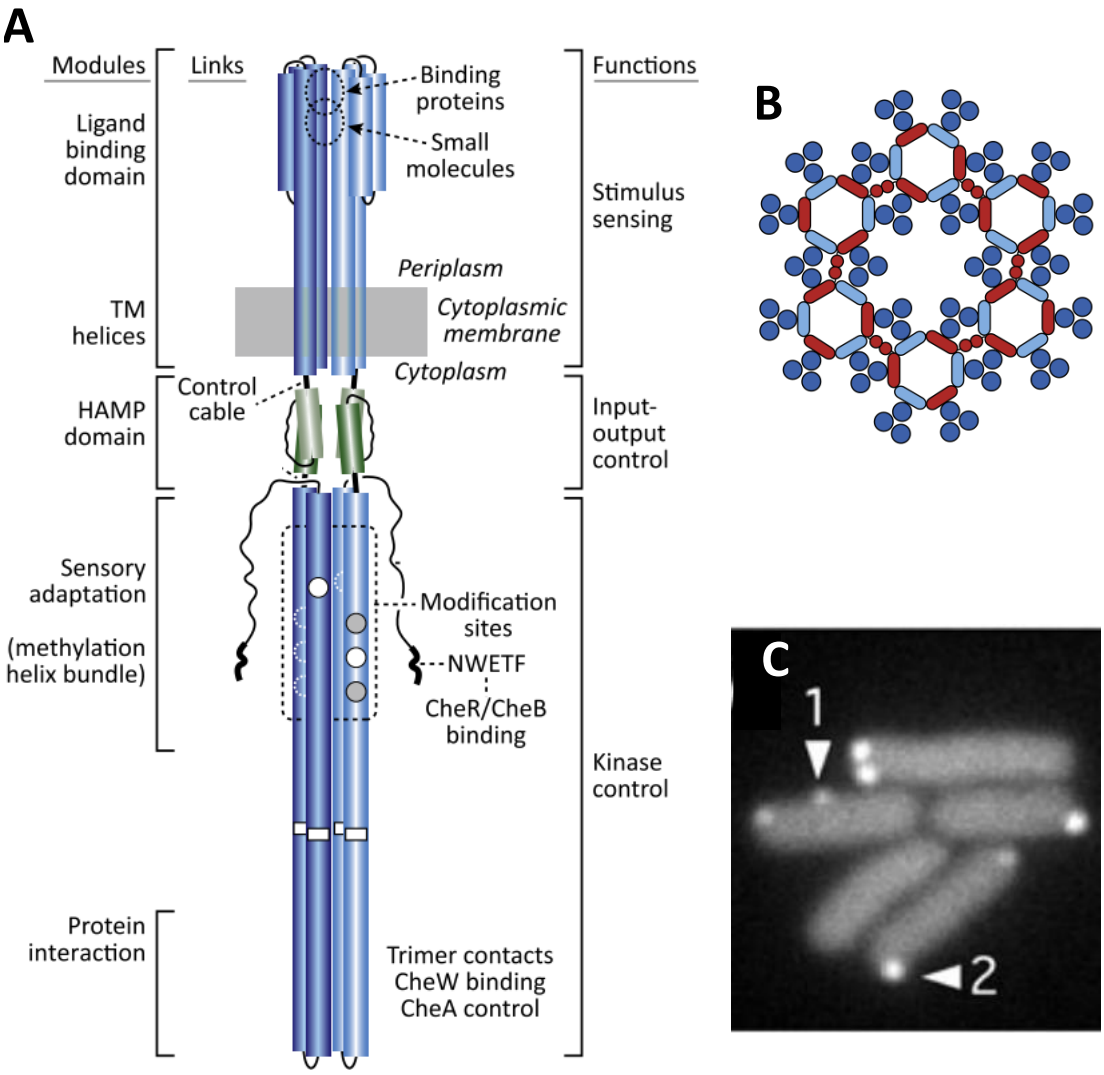


FIGURE 1.11: A: A dimer consisting of two MCP monomers, showing its position relative to the membrane and highlighting various structural features and their function. Adapted from (Parkinson et al., 2015) B: A "unit cell" of the mixed chemoreceptor cluster in the membrane, viewed top down. Dark blue circles are receptor dimers, CheA monomers are shown in red and CheW is shown in light blue. Taken from (Jones, 2015). C: A fluorescence microscopy image showing receptor cluster localization within the membrane of *E. coli* cells. (Kentner et al., 2006)

CheZ. By measuring the FRET signal, one can quantify how much these two proteins associate and gauge the activity in the network.
With the FRET assay, changes in aspartate concentration are detectable from $\sim$ 0.1 $\mu$M (Krembel et al., 2015; Neumann et al., 2014; Jasuja et al., 1999; Meir et al., 2010). Serine elicits a response with steps as low as $\sim$0.03 $\mu$M (Krembel et al., 2015). The kinase activity saturates around 10-20 $\mu$M for aspartate and around 1.5 $\mu$M for serine (Meir et al., 2010; Krembel et al., 2015). When chemotactic wild type cells were exposed to sub-saturating steps in concentration, it took up to several minutes for the FRET signal to return the to pre stimulus level (termed adaptation), depending on the step magnitude as shown on Figure 1.12 A (Krembel et al., 2015; Neumann et al., 2014). In another kind of assay, an experiment measuring how cells accumulate in chemotactic gradients using microfluidic devices, bacteria were shown to be able to detect changes in aspartate concentration as fine as 3nM (Mao et al., 2003). This kind of a change is more representative of what one would expect in practical continuous spatial gradients. Examining Figure 1.12 A, we find that an aspartate step under 10 nM would have a kinase activity adaptation time under 5 seconds. This is in agreement with previous tethered cell rotation measurements where CW Bias adapted within seconds of *E. coli* being exposed to a small step in aspartate (Segall et al., 1986). Adaptation on the scale of seconds, rather than minutes is thought to be necessary for bacteria to be able to navigate gradients by making temporal comparisons (Vladimirov et al., 2009).
When the step concentrations go beyond saturation, for example 1 mM aspartate, the adaptation is only partial, not proceeding over 80% of the original kinase ativity for that particular step (Neumann et al., 2014). The consequences of diminished adaptation were explored with computer simulations and it was shown that lower levels of adaptation come with lower precision with which the cells can locate the concentration peak in an attractant gradient (Neumann et al., 2014).
Results in agreement with the FRET experiment have been obtained by monitoring the output of the chemotactic network, the tumble bias of swimming cells (Min et al., 2012). The authors performed steps in aspartate concentration larger than 1 $\mu$M and found that the timescales of adaptation of the tumble bias were similar to those for kinase activity. For example, from Figure 1.12A we can read that the adaptation time for kinase activity in the case of a 1 $\mu$M step up in aspartate is approximately 20 seconds, in agreement with the 1 $\mu$M bias

trace on Fig. 1.12 B.

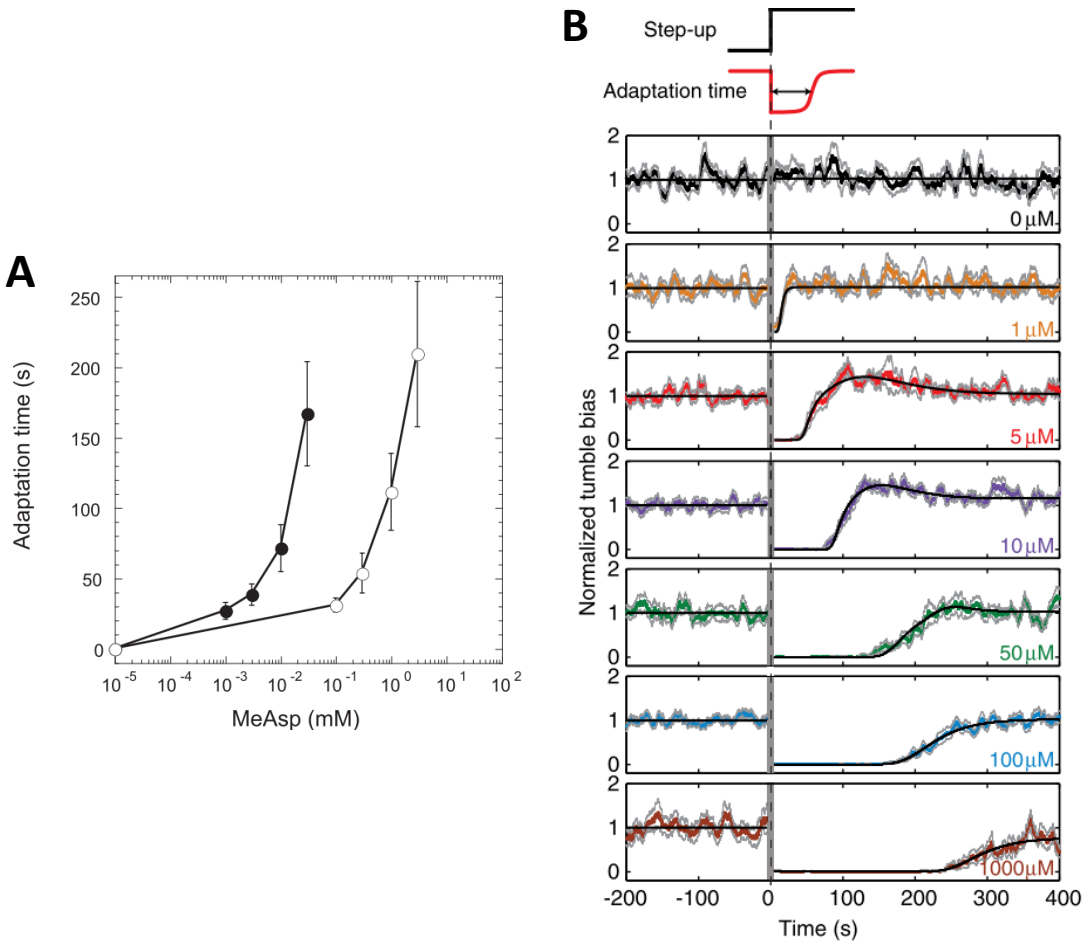


FIGURE 1.12: A: CheZ-CheY kinase activity adaptation times given against the magnitude of the step in methyl-aspartate concentration. Adaptation time is defined as the time neccessary to recover half of the FRET signal magnitude. Black points represent steps from no aspartate to the given concentration, while empty circles are cells that were already in the background of 1mM me-asp, an amount that saturates the receptors. (Krembel et al., 2015) B: Adaptation of tumble bias for swimming *E. coli* after being exposed to various upshifts in concentration of aspartate. (Min et al., 2012)

## 1.3 *E. Coli* lives in a fluctuating environment

*Escherichia coli* is normally found in the gastrointestinal tracts of humans and other warm blooded animals (Savageau, 1983; Bettelheim et al., 1974), and is one of the causes of urinary tract infections in humans (Bower et al., 2005). It can also be found in samples of soil, water and even on algae (Ishii et al., 2008; Elsas et al., 2011). Wherever the temperature is sufficiently high and nutrients abundant, *E. coli* can survive, and grow outside a warm blooded host. Thus, it needs to be able to cope with spatial and temporal changes of its surroundings. Some of those changes take the form of shifts in the extracellular osmolality. Examples include dry periods and excessive rainfall in soil and aqueous environments, different osmolalities throughout the urinary tract and complex spatiotemporal osmotic changes in the gastrointestinal system. The human ileum, the part of the small intestine preceeding the colon, seems to be one of the preferred sites of colonisation of *E. coli* O157:H7 , an enterohaemorrhagic strain which is a common foodborne pathogen (Moxley, 2004; Chong et al., 2007). In colonoscopic measurements (Fig. 1.13), just having breakfast

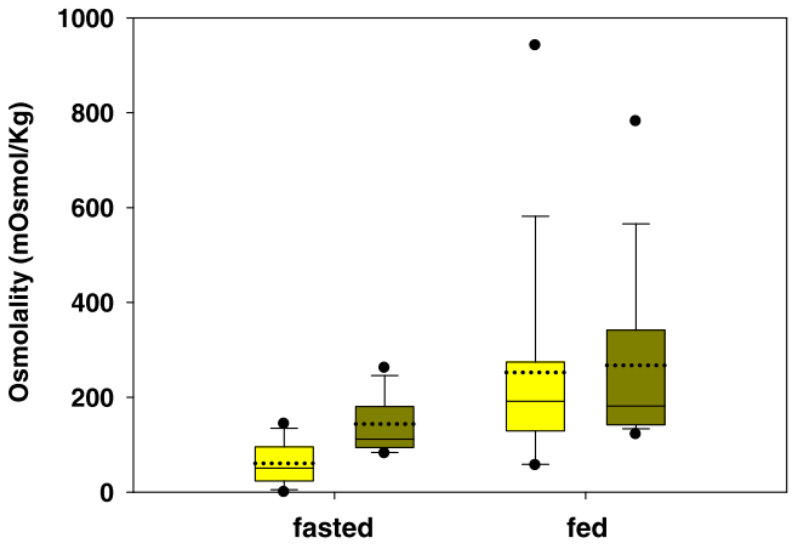


FIGURE 1.13: Ileum (light yellow) and caecum (dark yellow) osmolalities obtained by colonoscopy on a group of 12 males. Fasted: Subjects were asked to fast overnight and not eat breakfast. Fed: On another day, the same group underwent colonoscopy 4.5 hours after breakfast. Dashed lines are means, solid median, box represents the interquartile range and whiskers 10-90th percentile. The change in mean ileum osmolality between fed and fasted conditions is $\sim 190\mathrm{mOsmol/kg}$ (Reppas et al., 2015)

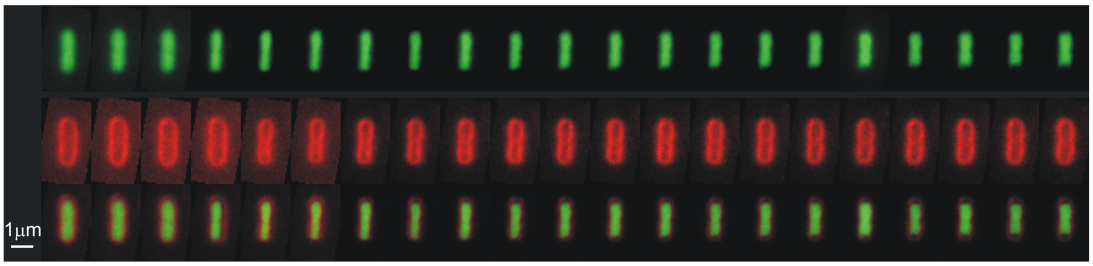


FIGURE 1.14: A sequence of fluorescence images showing different stages of the cell size and volume following an osmotic shock with 470 mM sucrose. Top: Cytoplasmic volume marked by an enhanced green fluorescent protein (EGFP); Middle: Total cell volume marked with the dye FM4-64; Bottom: Top and Middle overlayed. Frames are 1.6 seconds apart. (Pilizota et al., 2012).

4.5 hours before the procedure revealed a $\sim$ 190 mOsm/kg increase in ileal osmolality (Reppas et al., 2015). Among detrimental effects of osmotic stress are a slower growth rate (Baldwin et al., 1995; Cayley et al., 2000; Pilizota et al., 2014), decreased protein stability (Stadmiller et al., 2017) and a likely energetic cost of maintaining internal pressure by active pumping and synthesis of certain chemical species (Perroud et al., 1985; Wood, 1999). Especially stark are the consequences to the intracellular pressure, and consequently volume, when the rise in external osmolality is sudden (Pilizota et al., 2012). These rises, termed osmotic upshifts or osmotic shocks, cause water efflux and the cell shrinks by an amount depending on the magnitude of the upshift. Figure 1.14 exemplifies this by showing a series of fluorescence images of a single cell undergoing a shock administered by addition of 470 mM Sucrose (Pilizota et al., 2012). In that study, the authors find that an upshift in sucrose osmolality of 400 mOsm/kg causes a volume reduction of $\sim$ 30%, which takes $\sim$ 5-6 minutes to recover before the cell resumes growth. To cope with such changes, *E. coli* are able to recover their volume by pumping in and synthesising compounds. These are termed osmoprotectants and can be accumulated into the cytoplasm without toxicity to increase the internal osmolality and draw water back in. Those that are taken up through transporters include $K^+$ and glycine betaine, while trehalose can be synthesised in the cytoplasm from glucose (Csonka et al., 1991). Glycine betaine has been shown to be transported into the cell against a concentration gradient, exemplifying the energetic cost associated with volume regulation (Perroud et al., 1985). Additionally, it not only serves as a passive means of elevating intracellular concentration but also

has a role in stabilising proteins under conditions of increased osmotic pressure (Stadmiller et al., 2017).

## 1.4 Navigational sensors detect more than just chemicals

Since osmotic changes can be a large burden on the cell, a question arises whether they can swim away to evade it, just like they would evade a source of $Co^{2+}$ ions (Tso et al., 1974). Supporting this idea is the detection of activity in the chemotactic network using FRET during an osmotic upshift performed with 100 mM Sucrose. Dynamics in association of CheY with its phosphatase CheZ were observed in a manner that is consistent with a repelling substance (Fig. 1.15). Furthermore, the authors suggest that osmotic pressure could mechanically perturb the MCP proteins, bringing structural changes that mimic binding of ligands (Vaknin et al., 2006).

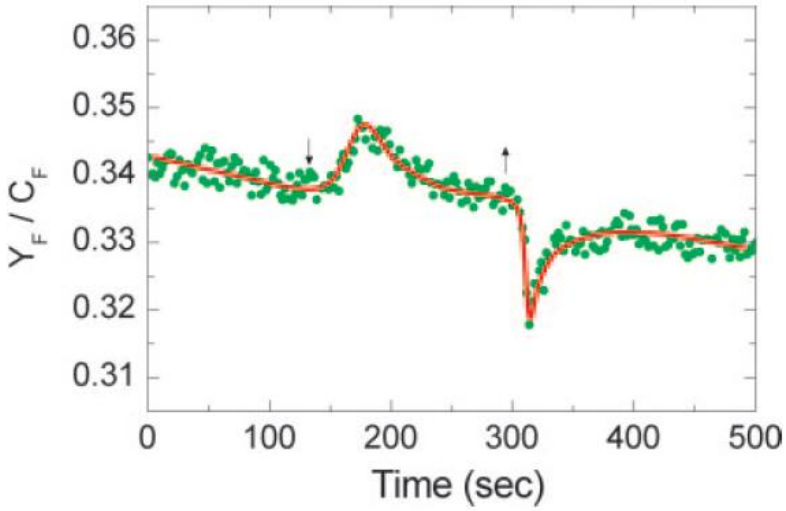


FIGURE 1.15: A measurement of the CheY-GPF CheZ-YFP FRET signal (y axis) against time for an osmotic upshift with 100 mM Sucrose. Black arrows indicate elevation of osmolality and subsequently bringing it back to buffer levels (Vaknin et al., 2006)

## 1.5 Previous observations of tactic behaviour in response to high osmolality

One of the oldest ways of studying bacterial taxis is the capillary assay. Employed as early as 1888 by Pfeffer and further developed by Adler, it consists of a capillary tube filled with a solution of some chemical of interest and a "pond" of bacteria into which the tube is inserted (Pfeffer, 1888; Adler, 1973). After some time the contents of the capillary are plated onto agar plates and, following an incubation, colonies are counted to infer the number of bacteria that entered the capillary (Adler, 1973). If the number is higher than that when the tube contains the exact same medium as the pond, the chemical is classed as a chemoattractant and if it is lower, a chemorepellent. A schematic of the capillary assay is pesented on Figure 1.16 A. This assay had also been used to quantitatively study bacterial accumulation in the presence of varying osmolalities. Adler et al. filled capillaries with concentrations of sucrose and ribitol ranging up to 800 mM and immersed them into a pond of bacteria for 30 minutes (Adler et al., 1988).

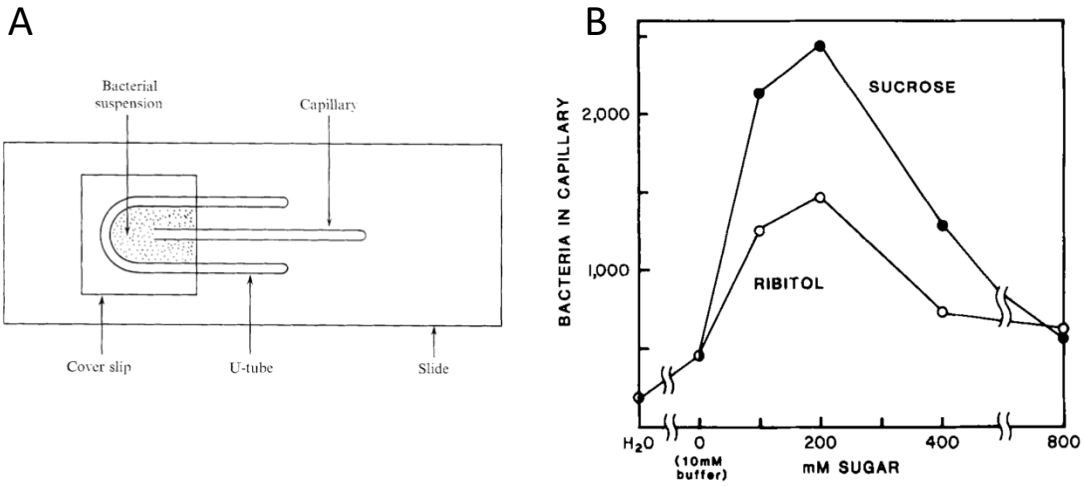


FIGURE 1.16: A: A schematic of the capillary assay used by Adler (Adler et al., 1973) B: Number of cells that migrated from the pond into the capillary for two different solutes, sucrose and ribitol, given against the concentration of the solution inside of the capillary. Actual concentration at the capillary-pond interface is smaller than the bulk capillary concentration due to diffusion (Adler et al., 1988)

They found that *E. coli* won't enter the tube if it is filled with pure water

and that there exists an optimal concentration of sugar where the accumulation peaks before falling off again at high concentrations. By performing the assay with single chemoreceptor mutants missing either Tar, Tsr, Trg, Tap or the phosphotransferase system enzyime I and finding the same result in every case, they concluded that no single chemoreceptor is involved. Thus they suggest that the attraction is non-specific and results from osmotaxis, the search for an optimum water activity. Their result is presented on Figure 1.16 B. Apart from sugars like sucrose and ribitol, medium osmolality in experiments is often elevated using sodium chloride. However, there is some evidence for involvement of chemoreceptors in taxis specifically towards or away from salts. $LiCl$ and $MgCl_2$ attraction relies heavily on Tsr and to a lesser extent on Tar, although these data have not been corrected for chemoreceptor abundances (Figure 1.17,Qi et al., 1989). While the peak attraction for both sucrose and NaCl happens at $\sim$ 200 mOsmol/kg, NaCl attracts 10 fold more bacteria, indicating that there is more than just osmotaxis at play (Adler et al., 1988; Qi et al., 1989). Additionally, presence of merely 10 mM of NaCl in the pond has been shown to inhibit salt taxis to the capillary by 50-90%, while that to serine and asprartate (main ligands of Tsr and Tar) dropped by 26 % and 7% respectively but presence of 50mM sucrose in the pond did not significantly hamper taxis to NaCl Qi et al., 1989. In summary, capillary assays suggest that there is an optimum osmolality the cells are attracted to and that there exists a class of compounds non-specific to any chemorecepor that produce an effect that could be purely due to water activity.

Another common way to investigate spatial patterns in bacterial motility utilises soft agar plates. In these, 0.3 % agar is poured into a petri dish and, in case of chemotaxis, a hard agar plug containing the test chemical is inserted into the soft agar. The chemical diffuses somewhat from the hard plug, creating a gradient throughout the plate. A suspension of motile bacteria is then poured over the plate and, after an incubation period, it is checked whether their density around the plug has increased, decreased or remained the same. From this, it is inferred whether the chemical is an attractant, repellent or has no specificity. Analogously, reaction to high osmolality has also been studied using the "plug assay" (Li et al., 1988; Adler et al., 1988). Plugs were made containing various concentrations of ribitol and clearings were observed around high concentration plugs (>0.3M), which the authors suggest to be due to repulsion

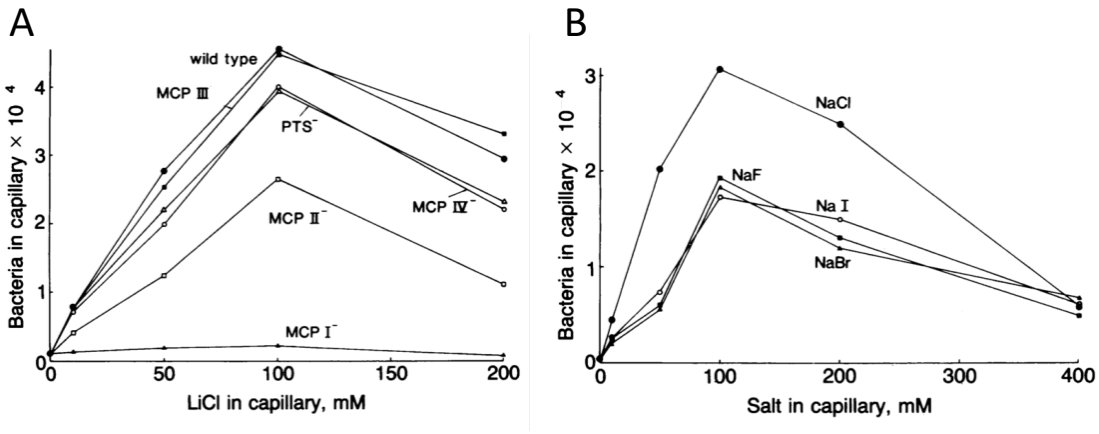


FIGURE 1.17: A: Number of bacteria in the capilary given against LiCl concentration in the bulk of the capilary. Curves are given for the chemotactic wild type and receptor mutants. MCPI, II, III and IV stand for Tsr, Tar, Trg and Tap respectively. PTS is a mutant lacking enzyme I of the phosphotransferase system. (Qi et al., 1989) B: Number of bacteria in the capillary given against salt concentration in the capillary for various sodium halide salts. (Qi et al., 1989). A schematic of the capillary assay is given on Fig. 1.16.

from high osmolality (Fig. 1.18 A). In comparison, D-Ribose, a chemoattractant, forms both clearings around high concentrations and also accumulates in rings around lower concentrations. When Trg, the ribose receptor, is knocked out, only the high concentration clearing remains (Fig.1.18 B and C). This is taken to indicate that the low concentration ring is indeed due to chemoattraction and the high concentration clearing is due to a chemical non-specific repulsion mechanism, namely osmotaxis away from high osmolalities (Li et al., 1988; Adler et al., 1988).

Analysis of videos of swimming bacteria was also used to characterize the reaction of bacteria to an elevation in medium osmolality (Li et al., 1988; Li et al., 1993). Li et al. imaged cells for several minutes after an osmotic upshift with KCl, and analysed the videos with motion analysis software to extract average linear and angular speeds of cells (Li et al., 1988). The latter are taken to correlate to the amount directional switching. There appears to be a small increase in swimming speed and a decrease in tumbling at an "optimum" osmolality, in agreement with the capillary assay (Li et al., 1988). The data from this study is presented on Figure 1.19 A and B. Although, it's difficult to say with such small differences how significant the change is. A much stronger

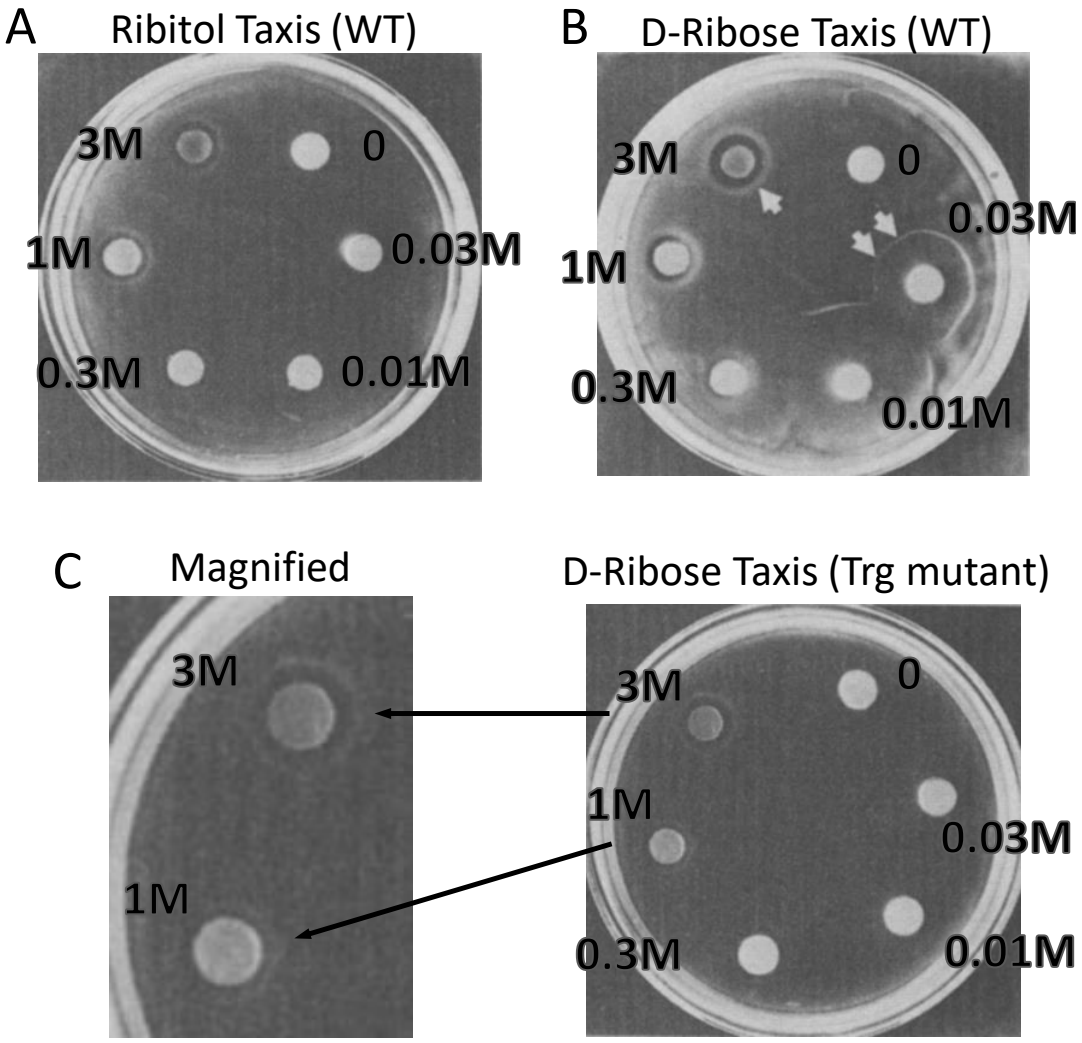


FIGURE 1.18: Hard agar plugs containing various concentrations of chemicals embedded in soft agar plates containing swimming bacteria. A: Ribitol plugs with a chemotactic wild type. Chemosensors are not able to detect ribitol and the clearings around the high concentration plugs have been attributed to taxis away from high osmolality. B: Chemotactic wild type with D-Ribose plugs. D-Ribose is detected by the Trg chemosensor. Clearings are present against high concentration plugs, like for 3M, indicated by the arrow. Lower concentration plugs have accumulation rings characteristic for chemotactic behaviour (0.03M, double arrow). C: A mutant lacking the Trg receptor (ribose sensor) used with D-Ribose, showing only clearings attributed to taxis away from high osmolality. (Adler et al., 1988; Li et al., 1988)

signal is an increased amount of tumbling when the upshift magnitude exceeds $\sim 100\mathrm{mOsmol/kg}$, inferred from the angular velocity data. The amount of tumbling continues to rise with increasing osmolality. In another study, Li and Adler characterized the angular speed of cells from 10s long videos of *E. coli* swimming post osmotic upshift using $\mathrm{NaNO_3}$ and found that the chemotactic wild type, when the osmolality rises over 200 mOsm/kg, tumbles more with increasing amount of solute in its surroundings (Li et al., 1993). A mutant missing all four MCP's and six Che proteins from the chemotactic signal phosphorelay entered a regime of increased tumbling when the osmolality surpassed 300 mosm/kg (Figure 1.19 C). It is unknown why the authors of these two studies used salt to elevate osmolality in lieu of their previous research (Qi et al., 1989) outlining some differences between salt taxis and pure osmotaxis. However, since their base buffer contains 10 mM of potassium phosphate, it is likely that the salt taxis is sufficiently inhibited for osmotaxis to be the dominant effect because they had to lower the base buffer concentration to 1mM in order to observe salt taxis (Qi et al., 1989).

Another way of investigating the tactic behaviour is by looking at the rotation of the flagellar motor. From the speed of the motor and the proportion of time it spends in CW (Tumble) mode we can obtain information about whether the cell would swim towards or away from a given stimulus. One way of realising this experiment is by allowing cells to tether to glass cover slips with their flagella and observe the rotation of the cell body. In response to osmotic stimuli delivered using high (0.1-0.8 M) concentrations of KCl, NaCl and sucrose, motors rotated in the CCW direction corresponding to cell runs (Adler et al., 1988). Even a tumbly mutant, that lacks all four MCPs and CheA,CheB,CheR,CheW,CheZ but contains CheY, rotated counter clockwise in response to 0.2 M KCl. A completely gutted, smooth swimming, mutant lacking all four MCPs and six Che proteins remained in the CCW mode of rotation in response to 0.2M KCl (Adler et al., 1988). Since CCW rotation is associated with stable bundle formation and cell runs, this is in contradiction with microscopic observations of shocked cells where experimenters have noticed that the cells are tumbling rather than running. Tumbling in response to osmolality is seen even in gutted mutants which should not be able to switch BFM direction, when looked at under the microscope (Adler et al., 1988). There is another apparent contradiction between the spatial accumulation assays and

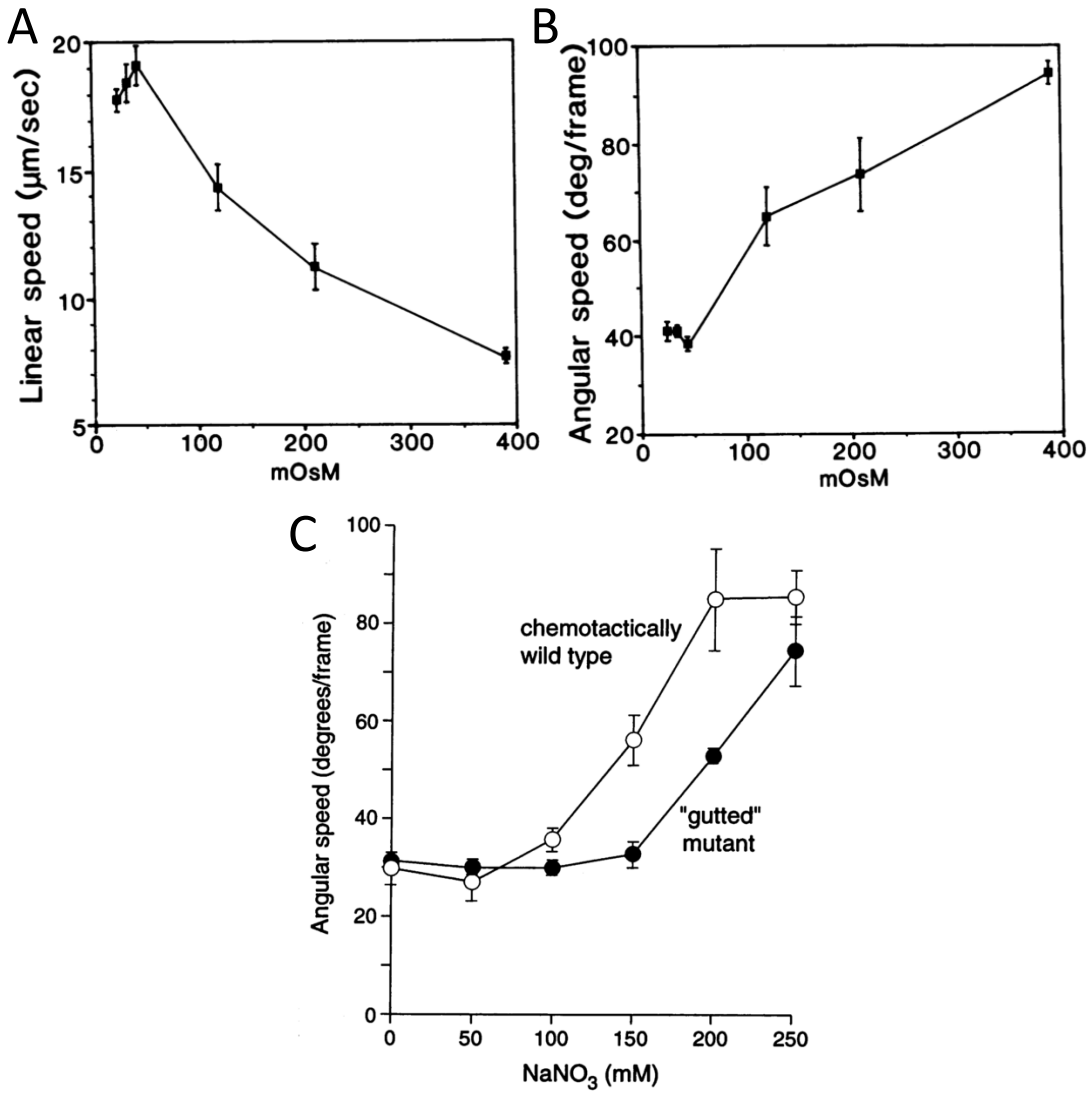


FIGURE 1.19: A: Average swimming speeds of chemotactic wild type *E. coli* cells sampled calculated from videos of cells swimming, several minutes in length, following osmotic shocks with KCl. B: Angular speeds, a quantity related to the amount of directional switching and thus tumbling, calculated for the same samples as in (A). (Li et al., 1988) B: Osmolalities were elevated using $NaNO_3$ and swimming bacteria were recorded for 10 seconds. Anglular speeds, relating to the amount of tumbling, were calculated. The figure compares a chemotactic wild type to a mutant lacking chemoreceptors and Che proteins (Li et al., 1993).

observations of swimming cells and tethered cells. In the spatial assays, clearing around a plug of high osmolality requires parts of the chemotactic network, although not any specific receptor but at least one of the major MCPs (Tsr, Tar) and an intact sensory phosphorelay to the BFM (Adler et al., 1988; Li et al., 1988). While CCW rotation accompanied tumbling,termed pseudotumbling (Li et al., 1993) behaviour seems to proceed even in mutants completely gutted of all chemotactic machinery. The length of this behaviour shows some dependence on the strength of the osmotic shock and it is possible that something structurally happens to the flagellar motor by the osmotically induced changes in the shape of the membrane. Perhaps the flagella remain locked in the CCW rotation as a consequence of these and are also unable to form stable bundles (Li et al., 1993) until the cell reinflates (Pilizota et al., 2012) and restores motor function. Since chemotactic mutants respond by pseudotumbling but don't perform spatial taxis, it is likely that pseudotumbling is a transient behaviour that is not relevant for spatial accumulation and is more of a consequence of a sudden change in osmolality. Indeed, in these experiments sudden steps in osmolality were at least 200 mOsm/kg in magnitude and often there were no osmoprotectants in the buffer, hampering the volume recovery of cells and possibly prolonging the artificial response.

## 1.6 Motivation for this thesis

### 1.6.1 *E. coli* motility in context of realistic environments

Studies of *E coli* chemotaxis have been extensively performed in dilute buffers, which allowed for administration of sub-saturating inputs of isolated chemicals. This approach generated a lot of information regarding sensor specificities, sensitivities and network response functions, integral for making bacterial chemotaxis one of the best studied and understood signalling networks in biology. However, the natural environment of *E. coli*, the intestinal system of humans and other warm blooded animals (Bettelheim et al., 1974; Savageau, 1983), is rich in nutrients and other chemicals and features spatial and temporal variations in nutrient content and osmolality. How motility contributes to *E. coli*'s life in the gut in not known. In mice, commensal MG1655 cells have been found to maintain a $\sim$ 10% motile subpopulation, after two weeks from their introduction, leading the authors to suggest a niche in the GI tract where

motility is important. Tamar et al. contributed to this idea by making an experiment where they have shown that two common laboratory strains (MG1655 and RP437) accumulated differently in a hydrogel that was in contact with an oxygenated surface (Tamar et al., 2016). They have proposed that different swimming characteristics can help certain strains reach niches such as oxygen rich epithelial tissue that is protected by a layer of mucus (Tamar et al., 2016). Studies of pathogenic strains revealed that Enterohaemorrhagic (O157:H7) *Escherichia Coli* shows a 1.5-4.3 fold upregulation of flagellar genes in response to a short chain fatty acid mixture characteristic of that found in the small intestine, and a 23 fold downregulation when exposed to a mixture characteristic of that found in the large intestine (Lackraj et al., 2016). Additionally, Chong et al. has a demonstrated a preference for O157 colonization of the human tissue from the distal part of the small intestine (terminal ileum) to human colonic tissue, ex vivo (Chong et al., 2007). They suggest that the infection might start in the terminal ileum and then spread throughout the intestinal system. Furthermore, O157 has been shown to have specificity for a particular kind of tissue that is abundant in the ileum, the folicle associated epithelium, where it forms attaching and effacing lesions (Moxley, 2004; Chong et al., 2007). Taken together, all of these results point towards a role of motility in the life of *E. Coli* within the host. Whether this role is reaching protected surfaces, outcompeting other bacteria in the fight for resources or something else, is at present not known.

Studying the response to sudden increases in osmolality is a first step towards understanding how do different environmental signals combine within the processing machinery of the chemotactic network and jointly affect the motor speed and bias. Some other stimuli like temperature, pH and oxygen levels have also been shown to feed into the same system (Armitage, 1999).

### 1.6.2 The aim of this thesis

The aim of this thesis is to understand the behavioural changes at the level of single motors and populational swimming when osmolality is increased and to address the contradictory observations about the involvement of the chemotactic network in the response to pure osmotic stimuli (Section 1.5). For example, why do all cells appear to tumble when exposed to an osmotic upshift under the microscope, but only those with an intact signalling phosphorelay

and at least Tsr or Tar chemosensor are able to perform spatial taxis (Adler et al., 1988; Li et al., 1988)? To answer this question I employ a technique which allows me to monitor the motor rotation with a high temporal resolution and over intervals of 20-30 minutes. Another interesting issue is the observation that, unlike for chemoattractants, the chemosensors show reduced methylation 30 minutes after exposure to 100 mM sucrose when compared to an unstimulated control, characteristic of adaptation to a repellent (Qi et al., 1989). However, 100 mM sucrose has also been shown to attract cells into a capillary, 30 minutes after inserting the capillary into a pond of a swimming bacteria (Adler et al., 1988). The response to an increased osmolality might proceed in several phases that are not visible in these measurements.

Specifically, I aim to characterize the temporal dynamics of CW Bias and to investigate when do cells run and when they tumble. I concentrate on pure osmotic stimulation of cells, achieved with sucrose, which has been shown to have no specificity for chemoreceptors in strain AW405, which is a parent of the KAF84 and KAF95 strains used here (Berg et al., 1993b). The concentrations of sucrose used for osmotic upshifts have been inspired by the changes *E. coli* encounters in the ileum and to correspond to ranges used in previous work, for easier comparison. Of interest are also the dynamics of motor and swimming speed, as they have also shown to drive accumulation of swimming bacteria, for example in shallow temperature gradients (Demir et al., 2012). Ultimately, the goal is to gain insight about how the response on the single motor level drives accumulation away from high concentrations and compare it with what we know about chemotactic responses as a first step towards studying how multiple inputs combine at the level of the flagellar motor.

# Chapter 2

# Materials and Methods

## 2.1 Bright field imaging

To study the rotation of the motor I have built an inverted bright field microscope. Figure 2.1 shows a schematic of the optical components. The bright field optical path is traced in orange, the upper part starts with a white LED (Luxeon Star, USA) driven by a computer controlled current source (A011-D-V-700 FlexBlock$^{TM}$, Luxdrive, USA). When driven with maximum current (700mA), the diode outputs 220 lm of luminous flux. It has been mounted a on top of a 10.7 $^{o}C/W$ heatsink which leads to a heatsink-LED junction temperature of 97 $^{o}C/W$, below the maximum operating temperature of 150 $^{o}C/W$ for that diode model. The light then passes through a f=15mm lens which focuses the image of the LED onto the back-focal plane of the condenser (Nikon, Japan; NA 1.45), which then maximally defocuses the light in the sample plane, setting up Kö hler illumination. Just after the f=15mm lens, a neutral density (ND) filter with a 100-fold attenuation makes sure that the sample is not over exposed. A field iris is placed between the ND filter and mirror M1, at a position where it's being imaged in the sample plane. To image the sample, I use a Nikon CFI Plan Apochromat Lambda 100x objective, with an NA of 1.45. After the objective, the bright field image is passed through a telescope formed of an f200 lens and one of three flippable (f50,f100,f150) lenses depending on the desired change in magnification. At the end of the beam path is a CCD camera with an f100 infinity lens.

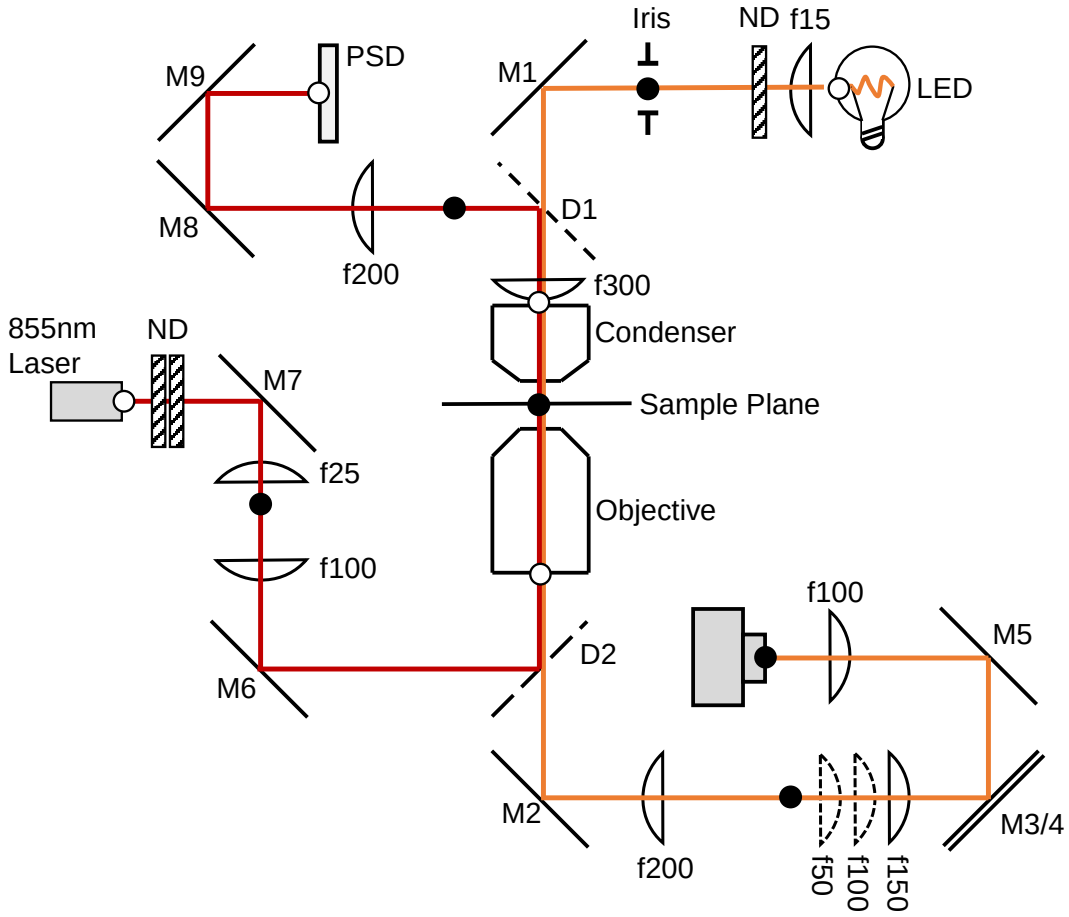


FIGURE 2.1: A schematic of the microscope including the bright field optical path (yellow) and the IR Laser optical path (red) which is used both for optical trapping and position detection. Black and white circles mark the two sets of conjugate planes. When a beam is focused in one set, it is collimated in the other. Optical elements: Mirrors are desigated by 'M', polychroic mirrors are marked by 'D' - D1 and D2 reflect IR light and let visible light trough. Lenses are denoted with 'f' followed by the focal length in millimiters. Neutral density filters, used to attenuate light are marked 'ND'. The double line, M3/4, is a periscope consisting of two mirrors M3 and M4, serving to lift the beam to the height of the camera. Details about the function of each element are given in sections 2.1 for bright field and 2.2 for the trapping and position detection

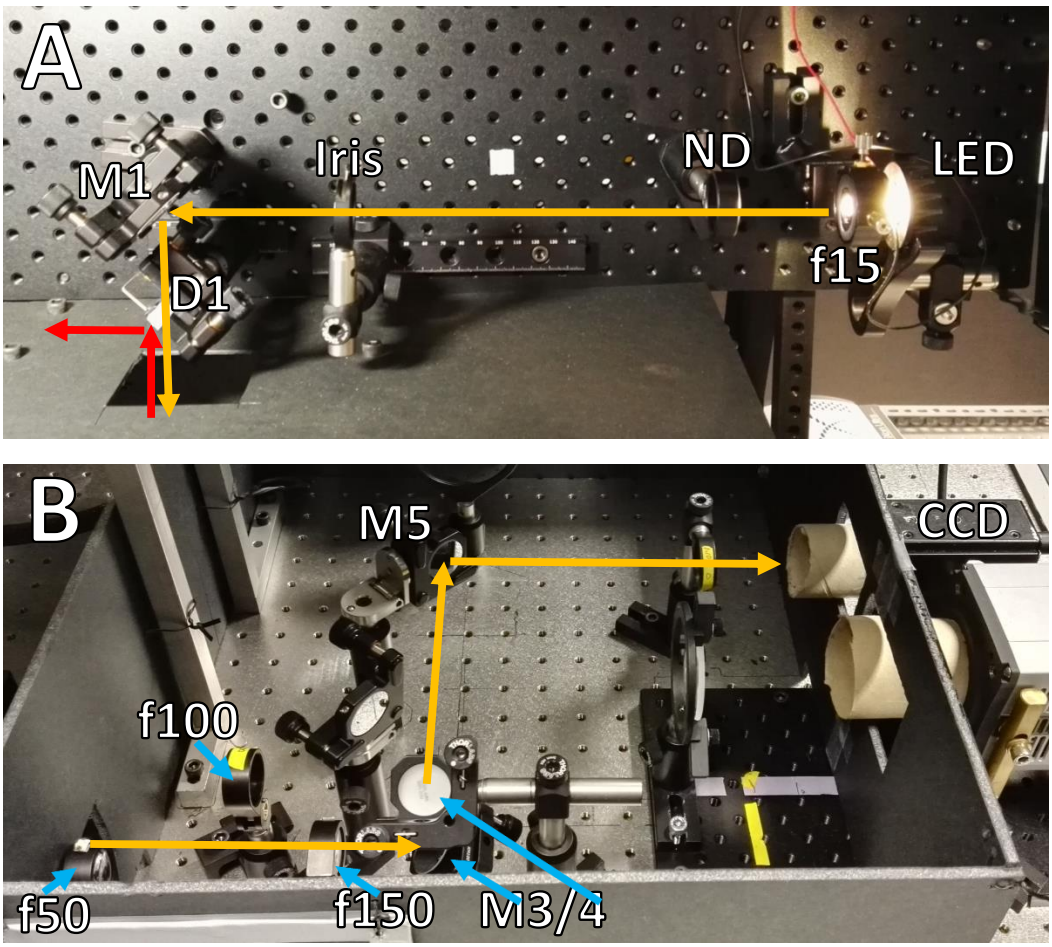


FIGURE 2.2: Images accompanying the microscope layout presented in Figure 2.1. Panel A shows the light source and Panel B the magnification lenses and the camera.

## 2.2 Optical Trapping and Position Detection

### 2.2.1 The Optical Trap

Trapping of micron sized objects in two counter propagating laser beams was first achieved in 1970 by Ashkin. Subsequently, it was demonstrated that a single laser focus could entrap dielectric particles sizing from only 25nm to 10$\mu$m (Ashkin et al., 1986). Since then, uses of optical traps have included manipulating bacteria and viruses (Ashkin et al., 1987b), moving organelles within cells (Ashkin et al., 1987a), studying kinesin movement along microtubules (Block et al., 1990) and pulling on bacterial flagellar fillaments (Darnton et al., 2007). An optical trap is formed by tightly focusing a laser beam using a lens of high

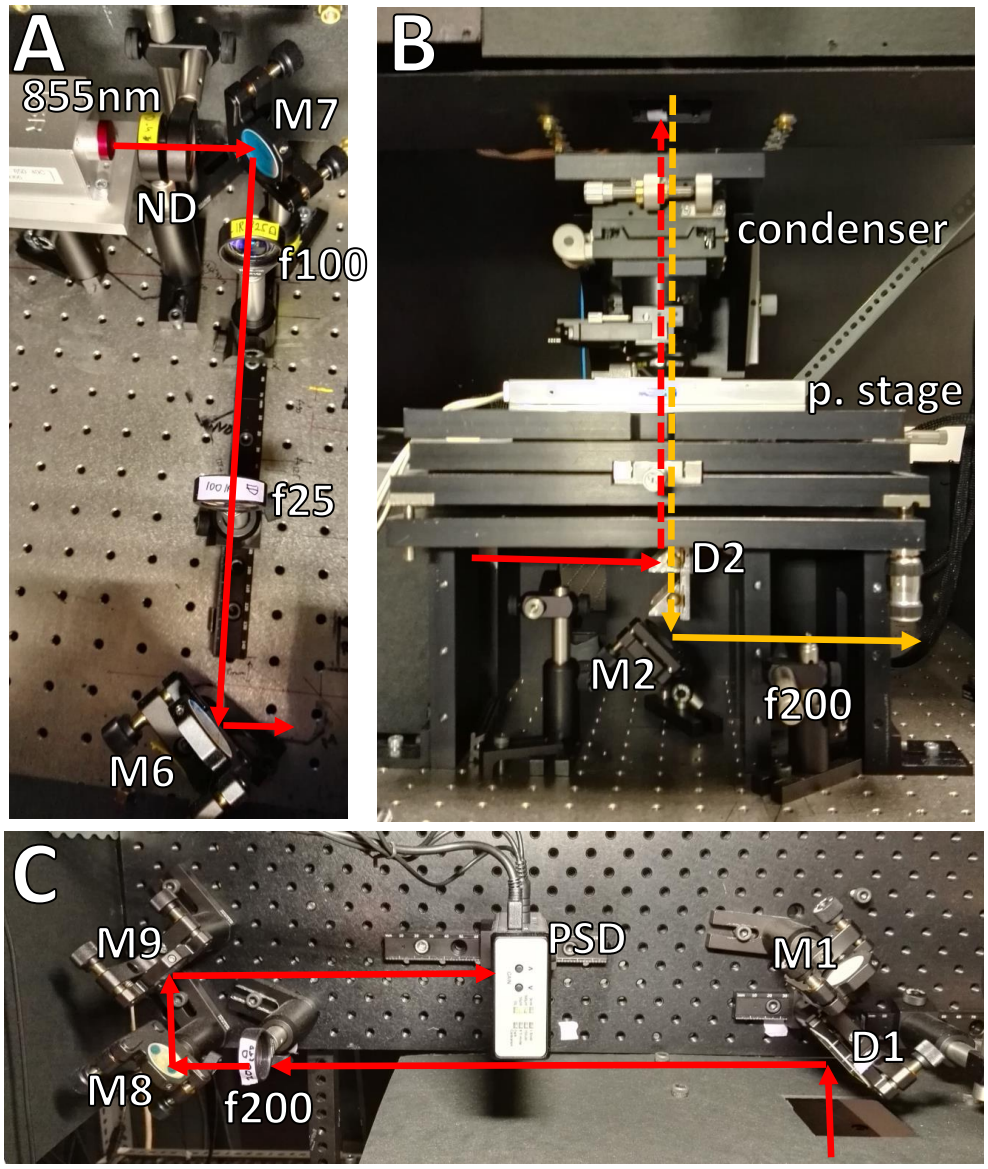


FIGURE 2.3: Images accompanying the microscope layout presented in Figure 2.1. Panel A shows the 855 nm laser with the associated mirrors and beam forming lenses. Panel B shows the main part of the microscope, including the coarse movement stages (black plates) and the nanometer resolution piezoeletric stage (MCL, USA). The microscope objective is located in the hollow middle of the coarse stages.

numerical apperture (Neuman et al., 2004). Figure 2.4 A shows a drawing of a single beam optical trap. To illustrate the forces at work, we resort to a simple case when the trapped particle is small compared to the wavelength of the laser. We are then in the Rayleigh regime where the optical force separates into

two distinct contributions, the scattering force and the gradient force (Neuman et al., 2004; Ashkin et al., 1986). The scattering force is often thought as a photon "fire hose" pushing in the direction of light propagation with magnitude $F_{scatt} \propto I_{in}$ proportional to the incident light intensity. The gradient force $F_{grad} \propto \pm\nabla I_{in}$ is proportional to the spatial gradient of incident light intensity with the $+$ sign if the refractive index of the particle is greater than the surrounding medium. In this work that is the case and thus the gradient force acts to pull the particle towards the focus.

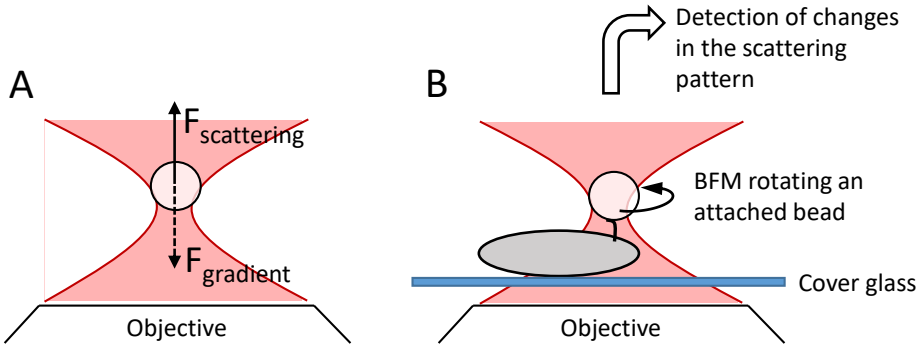


FIGURE 2.4: A: Sketch of an optical trap formed by focusing a laser beam, through an inverted objective, into the sample plane of a microscope. A microsphere is shown trapped in the laser focus at a height where the scattering and gradient forces balance each other. B: The laser is heavily attenuated and a sample is inserted where an *E Coli* cell is attached to a surface of a cover glass and a microsphere is attached to a truncated flagellar filament. The BFM is rotating the spherical bead and thus causing changes in the way the bead scatters laser light.

### Layout of the optical trap

The optical trap is formed using an 855 nm continous wave diode laser (Blue Sky Research, USA) with a nominal pointing stability of less than 10 $\mu\mathrm{rad}/^{\circ}\mathrm{C}$ and power stability of under 0.5 % change over 2 hours. Figure 2.5 shows the calibration line for the laser power in mW against control voltage, supplied from a PC using a DAQ board (DAQmx, National Instruments, USA). In the inset I verify that the laser power is indeed stable in the long term.

Since the majority of time, the trap is used for position detection as opposed to trapping, the beam is by default attenuated as soon as it leaves the laser.

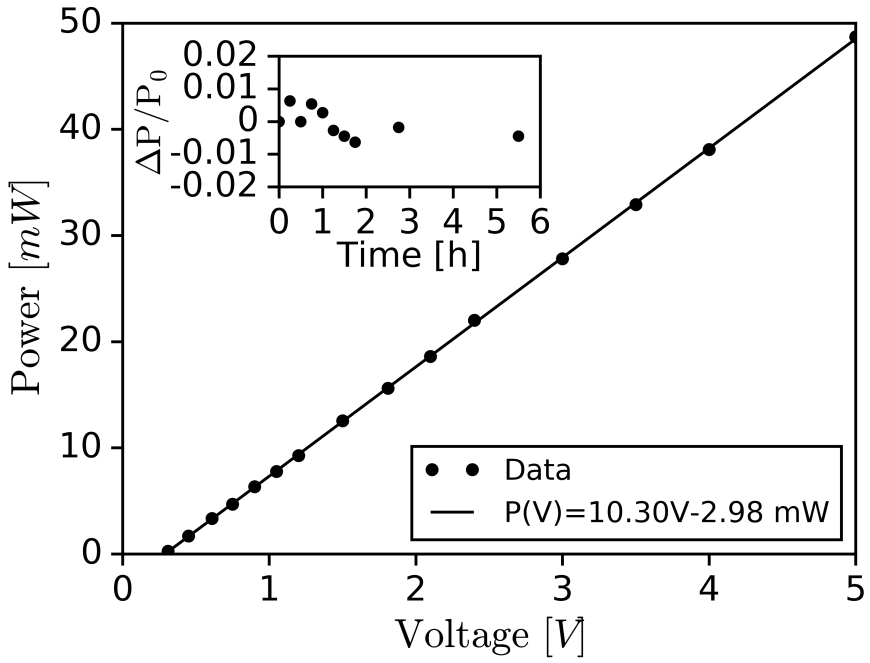


FIGURE 2.5: Power in the laser beam at the exit pupil of the laser, given versus control voltage. The points represent measurements with a photo diode power sensor (Thorlabs, USA) and the line is a best fit. Line parameters are given in the legend. The inset represents the percentage change of the laser power, relative to the initial power, over 5.5h of observation.

Two ND filters reduce the intensity by a factor of $1.55 \cdot 10^{-3}$ (Fig. 2.1) and then the beam is expanded 4 times by passing it through a telescope formed with an f=25mm and f=100mm lens. Thereafter, it is steered to the back aperture of the objective, overfilling it in order to be able to achieve good trapping of objects when desired. With the ND filters removed to provide enough power, overfilling and a high NA objective are instrumental in trapping, since that way a good balance of forward scattering and backwards restoring gradient force is achieved within the beam focus (Ashkin, 1992).

Most high NA objectives (including one used here) are corrected for spherical aberration only at a certain working depth (Fällman et al., 2003; Ghislain et al., 1994), usually at the cover-glass surface and the trap quality falls victim to focal imperfections if one ventures more than 20 $\mu$m into the bulk of the sample (Grange et al., 2002). However, here we only go at most 10 to 20 percent of that depth.

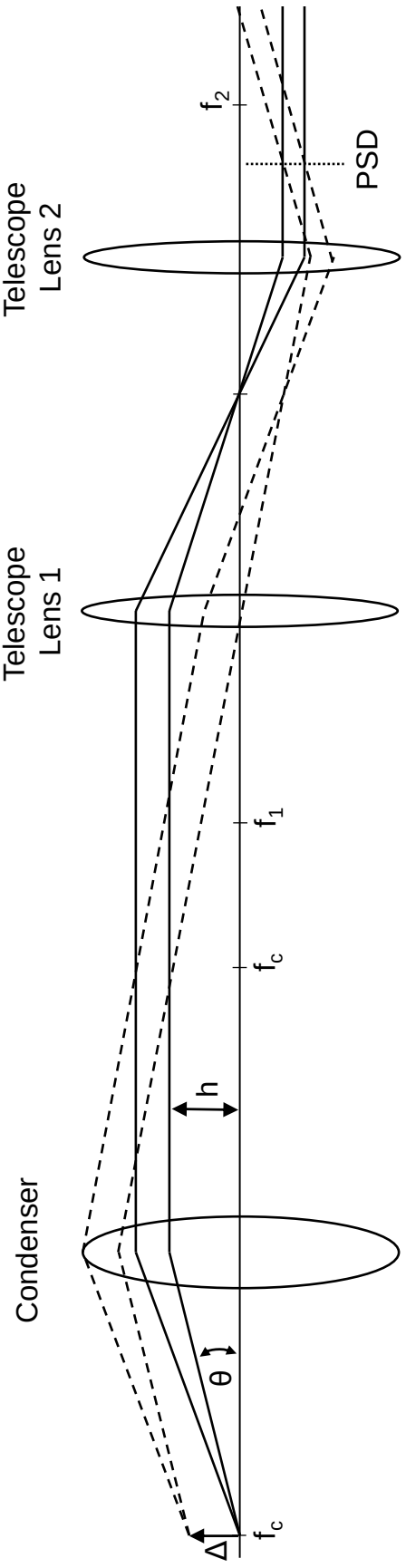


FIGURE 2.6: A schematic of the optical elements and rays in the IR laser path between the image plane and the position sensitive detector. A micron sized object scatters laser light on the left hand side of the condenser lens (image plane). The scattered and unscattered laser light interfere in space and this pattern propagates down the optical train through a pair of telescope lenses before being imaged by a PSD placed at such a position that it images the back focal plane of the condenser, $f_c$. For details see section 2.2.2

### 2.2.2 Back Focal Plane Interferometry

A single bacterial flagellar motor drives its filament at a speed in excess of 100 Hz (Min et al., 2009; Sowa et al., 2008) and can not be observed in a microscope due to its sub diffraction limit dimensions. One way of giving it a tangible spatial dimension is attachment of polystyrene or latex beads to a truncated flagellar filament. The diameters of the microspheres commonly range between 0.3 $\mu$m, which spin at speeds up to $\sim$ 300Hz (Chen et al., 2000a), to 1.5 $\mu$m with speeds $\sim$ 25Hz (Bai et al., 2013). Rotation of spheres at these frequencies can be captured by using a fast camera, but at the expense of generating large quantities of image data which puts constraints of the duration of imaging. To circumvent this limitation, I used a heavily attenuated optical trap to detect position of an object relative to the axis of the laser beam, a technique termed Back Focal Plane (BFP) interferometry. (Neuman et al., 2004; Gittes et al., 1998). BFP has previously been used to measure the motion of beads driven by molecular rotary motors such as the bacterial flagellar motor (Chen et al., 2000a; Pilizota et al., 2007), the $F_1F_0$ ATP-ase (Pilizota et al., 2007) and linear motors like NCD, a member of the kinesin family (Allersma et al., 1998).

A microscopic object in the focus of a laser will scatter the light and the unscattered and scattered beams will interfere in space to produce an angle dependant intensity pattern (Gittes et al., 1998). Because the sample plane is in focus of the condenser, the pattern will appear at the back-focal plane of the condenser as collimated light. For rays originating from a small object and impinging on a thick lens with considerable inclination, as is the case here due to the high NA of the condenser, the sine condition describes propagation of such rays in the regime of geometric optics. For a ray passing through the focal point of a lens of focal length $f$, closing an angle $\theta$ with the optical axis, the condition states that the ray emerging on the other side of the lens will be parallel to the axis and at distance $h = f \sin\theta$ from it (Born et al., 1999; Gittes et al., 1998). (See Figure 2.6)

The technique gets its name from the beneficial property of imaging the scattering pattern at the back focal plane of the condenser ($f_c$ on Fig. 2.6). This is illustrated on Fig. 2.6 where we can see that even if the source of scattered light in the image plane is moved by a distance $\Delta$, the rays after the condenser will still intersect the back focal plane (at $f_c$) at the same points. Thus the signal will only be sensitive to the relative positioning of the scattering particle with

respect to the laser beam and not on the absolute position of the laser beam within the image plane.

**Implementation in the microscope**

The scattering pattern pattern from the BFP is relayed to a position sensitive detector by a telescope consisting of an f=300 mm and an f=200 mm lens, resizing the beam so its diameter matches the size of the detector chip, improving the signal to noise ratio. The PSD is placed at a specific position after the telescope where it images the BFP (Fig. 2.6 ).

To achieve this placement, the condenser was moved by $\Delta$ in X and Y direction (perpendicular to beam) for a fixed amount ($\sim 100\mu m$) and the change in X and Y detector voltages were measured. When the PSD is placed relative to the f=200 mm lens such that it approximately images the back focal plane both voltage changes should both be minimal. Figure 2.7 shows the result of this measurement. We note a mismatch of minima for $|\Delta \mathrm{V_x}|/|\Delta \mathrm{x}|$ and $|\Delta \mathrm{V_y}|/|\Delta \mathrm{y}|$, likely due to a tilt of the f=300 mm lens which is permanently fixed to the condenser mount. A position intermediate between the two minima was chosen, at x=65 mm on the mounting rail. At this point this error does not influence the measurement as the laser focus position is approximately on optical axis (within 10 $\mu\mathrm{m}$) and remains stationary during measurement.

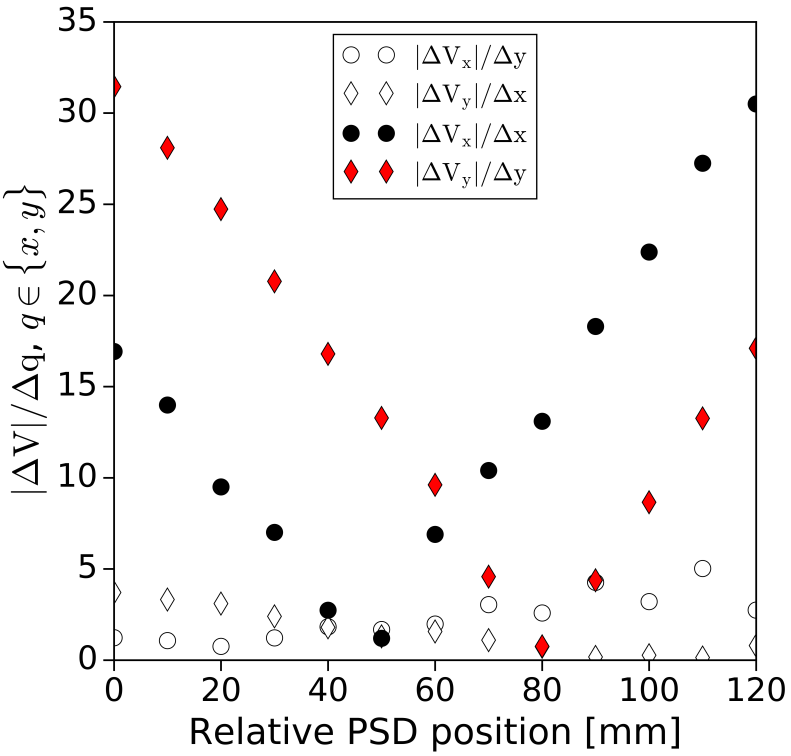


FIGURE 2.7: The PSD was moved in the 'z' direction on a rail while the condenser was moved in x and y. The ordinate axis shows the change in PSD Signal X and Y voltage when the condenser was displaced in X or Y. Circles represent $|\Delta V_x|$, the change in X signal voltage when the condenser was displaced in the X direction ($|\Delta V_x|/|\Delta x|$, full black) and when the displacement is in the Y direction ($|\Delta V_x|/|\Delta y|$, empty circles). Diamonds represent analogous quantities for the Y signal, full red diamonds representing $|\Delta V_y|/|\Delta y|$ and empty diamonds representing $|\Delta V_y|/|\Delta x|$.

### 2.2.3 Data Acquisition

The output of the PSD is a pair of voltages $(V_x, V_y)$ corresponding to an X and Y position of the bead within the optical trap. In this work, the rotational frequencies are below 300 Hz but the data is acquired at a rate of 10 kHz. To remove high frequency noise, we apply a low pass filter to the signal before sampling. The filtering is done with a analog low pass filter (Krohn-Hite Corporation) using a Bessel window and a nominal cut off frequency of 2.5 kHz. The frequency response of the filter is given in Figure 2.8 where the inset zooms into the [0,300Hz] band of interest.

After filtering, sampling was performed at 10 kHz by a DAQ board (DAQmx, National Instruments, USA). Data was displayed and stored on the measurement computer using a custom program I developed in LabView (National Instruments, USA). The schematic of the program is given in Appendix A.

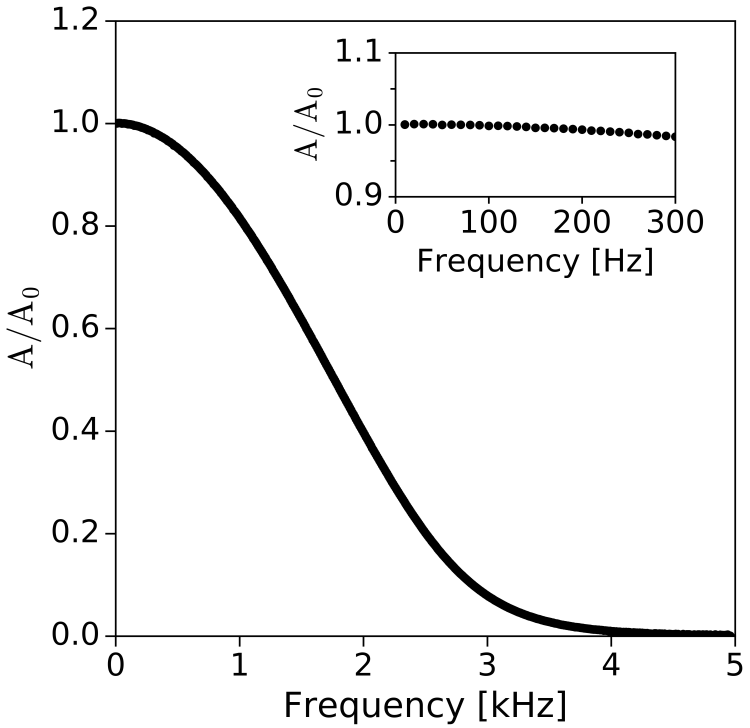


FIGURE 2.8: Frequency response of the short pass filter of bessel type when the cut-off frequency on the front panel of the box is set to 2.5 kHz. Inset zooms in the 0-300 Hz range of the pass band, a range within which all of the signal frequencies measured in this work fall.

## 2.3 Differential Dynamic Microscopy

Differential dynamic microscopy (DDM) is a high throughput method for measuring the speed distribution of a large number of free swimming cells. By averaging over $\sim 10^4$ cells in one measurement, it is much faster than tracking (Wilson et al., 2011; Martinez et al., 2012). It works by recording low magnification videos of bacteria swimming and analysing the statistics of temporal fluctuations of pixel intensities, which are caused by the variation in the number density of bacteria. It measures the differential image correlation function (DICF), which is effectively a power spectrum of the difference between two images taken at separate time points (Wilson et al., 2011; Martinez et al., 2012). If a theoretical motility model exists, such as in the case of *E. coli*, the expected DICF can be calculated and fitted to experimental data (Wilson et al., 2011), allowing accurate estimates of the distribution of free-swimming speeds of a large number of bacteria (Martinez et al., 2012).

To briefly outline the theory of DDM, consider a time sequence of microscopy images. An image is described by a distribution $\mathrm{I}(\vec{\mathrm{r}}, \mathrm{t})$ of intensities where $\vec{\mathrm{r}}$ is the position of a given pixel and $\mathrm{t}$ is the time the picture was taken. Every frame of the video can be described as a fluctuation $\Delta\mathrm{I}(\vec{\mathrm{r}}, \mathrm{t}) = \mathrm{I}(\vec{\mathrm{r}}, \mathrm{t}) - \langle \mathrm{I} \rangle$ around an average intensity $\langle \mathrm{I} \rangle$ (Berne et al., 2000).

A difference between two images, time $\tau$ apart, gives the intensity

$$\mathrm{D}(\vec{\mathrm{r}}, \tau) = \Delta\mathrm{I}(\vec{\mathrm{r}}, \mathrm{t} + \tau) - \Delta\mathrm{I}(\vec{\mathrm{r}}, \mathrm{t}). \tag{2.1}$$

The Fourier transform of $\mathrm{D}(\vec{\mathrm{r}}, \tau)$ is

$$\mathrm{F_D}(\vec{\mathrm{q}}, \tau) = \int \mathrm{D}(\vec{\mathrm{r}}, \tau) \mathrm{e}^{\mathrm{i}\vec{\mathrm{q}}\vec{\mathrm{r}}} \mathrm{d}\vec{\mathrm{r}}, \tag{2.2}$$

which is used to define the DICF $\langle |\mathrm{F_D}(\vec{\mathrm{q}}, \tau)|^2 \rangle$ (Wilson et al., 2011; Martinez et al., 2012). Next, an assumption is made that the fluctuations in pixel intensity are proportional to the fluctuations in the number density of bacteria, $\Delta\mathrm{I}(\vec{\mathrm{r}}, \mathrm{t}) = \kappa \Delta\rho(\vec{\mathrm{t}}, \mathrm{t})$. The constant of proportionality $\kappa$ depends on the image contrast mechanism (Wilson et al., 2011; Martinez et al., 2012). The number density is $\rho(\vec{\mathrm{r}}, \mathrm{t}) = \sum_{\mathrm{i}} \delta(\vec{\mathrm{r}}(\mathrm{t}) - \vec{\mathrm{r}}_{\mathrm{i}}(\mathrm{t}))$, summing up over all of the particles, represented with delta functions. The fluctuation of number density around the average density $\langle \rho \rangle$ is $\Delta\rho(\vec{\mathrm{r}}, \mathrm{t}) = \rho(\vec{\mathrm{r}}, \mathrm{t}) - \langle \rho \rangle$ and the Fourier transform of the fluctuation is $\Delta\rho(\vec{\mathrm{q}}, \mathrm{t}) = \int \Delta\rho(\vec{\mathrm{r}}, \mathrm{t}) \mathrm{e}^{\mathrm{i}\vec{\mathrm{q}}\vec{\mathrm{r}}} \mathrm{d}\vec{\mathrm{r}}$ (Berne et al., 2000; Wilson et al., 2011;

Martinez et al., 2012). Combining equations 2.1 and 2.2, and expressing intensity fluctuations in terms of density fluctuations, gives

$$F_D(\vec{q},\tau) = \kappa[\Delta\rho(\vec{q},t+\tau) - \Delta\rho(\vec{q},t)]. \tag{2.3}$$

This is then used to calculate the DICF, $\langle|\mathrm{F_D}(\vec{\mathrm{q}},\tau)|^2\rangle$, which after averaging over all initial starting times,t, and dropping the vector over $q$ under assumption of isotropy becomes

$$\langle|\mathrm{F_D}(\mathrm{q},\tau)|^2\rangle = \mathrm{A}(\mathrm{q})[1-\mathrm{f}(\mathrm{q},\tau)]\mathrm{B}(\mathrm{q}), \tag{2.4}$$

where

$$\mathrm{f}(\mathrm{q},\tau) = \langle \mathrm{e}^{\mathrm{i}\vec{\mathrm{q}}\vec{\mathrm{r}_\mathrm{i}}(\mathrm{t}+\Delta\mathrm{t})}\mathrm{e}^{-\mathrm{i}\vec{\mathrm{q}}\vec{\mathrm{r}_\mathrm{i}}(\mathrm{t})}\rangle = \langle \mathrm{e}^{\mathrm{i}\vec{\mathrm{q}}\Delta\vec{\mathrm{r}_\mathrm{i}}}\rangle,$$

which is evaluated by averaging over all particles and directions of $\Delta\vec{r}$ with respect to a given direction of $\vec{q}$. $\mathrm{A}(\mathrm{q}) = 2\kappa^2\langle[\Delta\rho(\mathrm{q})]^2\rangle$ is a factor that includes dependence on the imaging system through $\kappa$ and on the sample structure through $\langle[\Delta\rho(\mathrm{q})]^2\rangle$. An additional term, $\mathrm{B}(\mathrm{q})$, *a posteriori* added to equation 2.4, accounts for camera noise (Wilson et al., 2011; Martinez et al., 2012). Equation 2.4 is known as the intermediate scattering function in dynamic light scattering (Berne et al., 2000). Averaging over all particles ($\vec{\mathrm{r}}_\mathrm{i}$) and evaluating $\mathrm{f}(\mathrm{q},\tau)$ for a population of isotropic, independent swimmers, all with the same velocity $\mathrm{v}$ yields (Wilson et al., 2011; Martinez et al., 2012)

$$\mathrm{f}(\mathrm{q},\tau) = \frac{\sin(\mathrm{qv}\tau)}{\mathrm{qv}\tau}. \tag{2.5}$$

Equation 2.5 will pick up a prefactor of $\mathrm{e}^{-\mathrm{Dq}^2\tau}$ since the ballistic swimming particles are also performing Brownian motion with a diffusion coefficient $\mathrm{D}$. However, if only a fraction $\alpha$ of the total population is motile and the swimming speed is given a distribution of values $\mathrm{P}(\mathrm{v})$, $\mathrm{f}(\mathrm{q},\tau)$ becomes (Wilson et al., 2011; Martinez et al., 2012)

$$\mathrm{f}(\mathrm{q},\tau) = \mathrm{e}^{-\mathrm{Dq}^2\tau}\left[(1-\alpha) + \alpha\int_0^\infty \mathrm{P}(\mathrm{v})\frac{\sin(\mathrm{qv}\tau)}{\mathrm{qv}\tau}\mathrm{dv}\right] \tag{2.6}$$

By selecting the Schulz velocity distribution, for reasons of having the correct peaked shape and yielding an analytically solvable integral, Wilson et al. have

produced a parametrized model for $\mathrm{f}(\mathrm{q},\tau)$ (Wilson et al., 2011)

$$\mathrm{f}(\mathrm{q},\tau) = \mathrm{e}^{-\mathrm{D}\mathrm{q}^2\tau}\left[(1-\alpha)+\alpha\left(\frac{\mathrm{Z}+1}{\mathrm{Z}\mathrm{q}\langle\mathrm{v}\rangle\tau}\right)\frac{\sin(\mathrm{Z}\tan^{-1}\theta)}{(1+\theta^2)^{\mathrm{Z}/2}}\right], \tag{2.7}$$

where $\theta = (\mathrm{q}\langle\mathrm{v}\rangle\tau)/(\mathrm{Z}+1)$, Z is a parameter of the distribution and is related to the variance $\sigma$ and the mean speed $\langle v\rangle$ by $\sigma = \langle\mathrm{v}\rangle(\mathrm{Z}+1)^{-1/2}$. The complete Schulz distribution is given by (Wilson et al., 2011; Martinez et al., 2012)

$$\mathrm{P}(\mathrm{v}) = \frac{\mathrm{v}^{\mathrm{Z}}}{\mathrm{Z}!}\left(\frac{\mathrm{Z}+1}{\langle\mathrm{v}\rangle}\right)^{\mathrm{Z}+1}\mathrm{e}^{-\mathrm{v}(\mathrm{Z}+1)/\langle\mathrm{v}\rangle}. \tag{2.8}$$

Using this model, one can obtain an average swimming speed from a series of high frame rate, low magnification videos of swimming bacteria. Taking all the possible differences $\mathrm{D}(\vec{\mathrm{r}},\tau)$ of images separated by a time $\tau$ and averaging their Fourier transforms, one arrives at $\langle|\mathrm{F}_\mathrm{D}(\vec{\mathrm{q}},\tau)|^2\rangle$. A further average over the directions of $\vec{q}$ yields $\langle|\mathrm{F}_\mathrm{D}(\mathrm{q},\tau)|^2\rangle$, which can then be fitted to the model outlined in the above equations to produce, among other quantities, the average ballistic swimming speed of bacteria (Wilson et al., 2011). In practice, the procedure is repeated for a range of values of $\tau$ and the calculation of $\langle|\mathrm{F}_\mathrm{D}(\mathrm{q},\tau)|^2\rangle$ is carried out for several values of $\mathrm{q}$. An example of thus calculated swimming speed $\langle\mathrm{v}(\mathrm{q})\rangle$, from (Wilson et al., 2011) is given in Figure 2.9. The relevant q region is determined by the limitations of the model. For example, only ballistic swimming can be studied with the current form of $\mathrm{f}(\mathrm{q},\tau)$. A lower bound on $\mathrm{q}$ is thus set by the length scale L on which tumbling and reorientation of cells starts happening and is approximately $2\pi/\mathrm{L} = 0.5\mu\mathrm{m}^{-1}$. The upper bound of about 3 $\mu\mathrm{m}^{-1}$ is set by the noise from cell body wobbling when probing length scales of $\sim 2\mu\mathrm{m}$, a typical cell size (Wilson et al., 2011; Martinez et al., 2012). As is visible from Figure 2.9, when an appropriate range of $\mathrm{q}$ is selected, the speed will be relatively constant through out a range of length scales. In this particular case the best range is between 1 and 1.5 $\mu\mathrm{m}^{-1}$. The residual slow variation within the interval can be used to define an uncertainty of the average value.

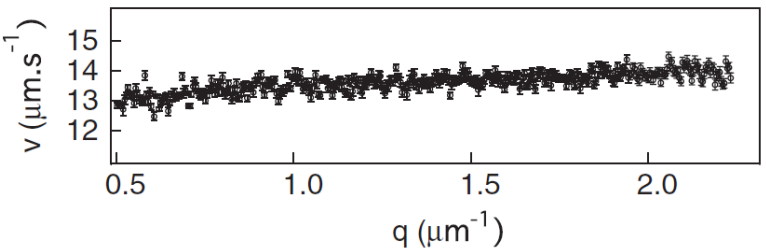


FIGURE 2.9: An example of the average swimming speed obtained by fitting equation 2.4 in a DDM analysis, given as a function of q. Adapted from (Wilson et al., 2011)

## 2.4 Strains, Growth and Media

### 2.4.1 *E. coli* strains and plasmids

*E. coli* strains KAF84 and KAF95 (Berg et al., 1993b) were used for BFM speed and bias, and MG1655 (Blattner et al., 1997) for cell swimming experiments. Both KAF84 and KAF 95 carry the *fliC726* allele, (produce nonflagellate phenotypes), and contain a plasmid carrying an ampicillin resistance and a $fliC^{sticky}$ gene (produces flagellar fillaments that stick readily to surfaces). Additionally, KAF84 is a chemotactic wild type and KAF95 is a ΔCheY strain and therefore can not perform chemotaxis, producing a smooth swimmer phenotype. MG1655 is a K-12 strain and a chemotactic wild type.

### 2.4.2 *E. coli* Growth and culturing

KAF95, KAF84 and MG1655 cells were grown in Tryptone Broth (1% Bacto tryptone, 0.5% NaCl) at 30°C while shaken at 200 RPM (Bai et al., 2010; Martinez et al., 2012). KAF95 and KAF84 were supplemented with 100 $\mu$g/ml of ampicillin and grown to OD=0.7-1.0 (Spectronic 200E Spectrophotometer, Thermo Scientific, USA), and MG1655 to OD=0.6. These optical densities correspond to the mid exponential phase of the growth curve, Fig. 2.10.

### 2.4.3 Buffers Used For Experiments

Experiments were performed in buffers which do not support growth to prevent re-growth of truncated filaments (See 2.5) as this would increase the radius of rotation of the bead and influence the drag coefficient. All buffers are

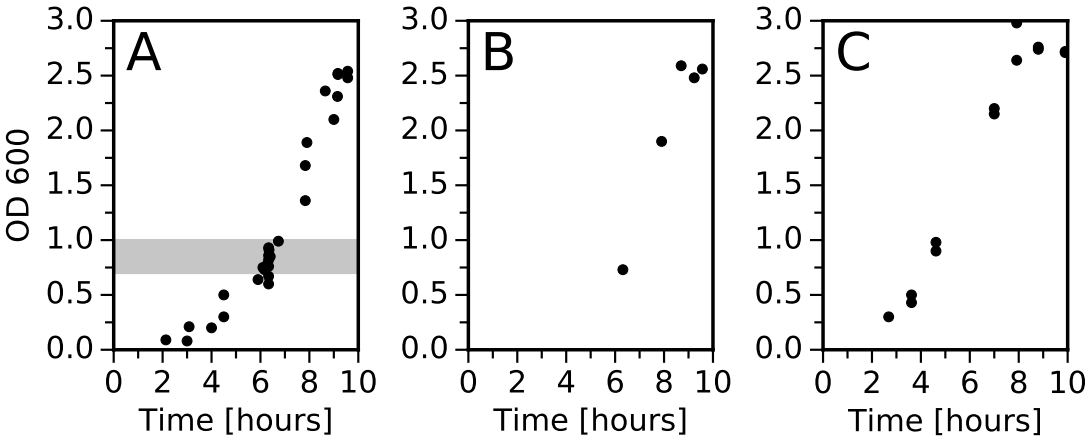


FIGURE 2.10: Growth data for strains used in the experiment. All were grown by innoculating 100 $\mu$L of frozen stock into 5mL of Tryptone Broth supplemented by appropriate antibiotics and shaken at 200 RPM at 30 degrees.(A) Curve compiled from points made with multiple samples of a single frozen stock of KAF 84. (B) Data for the frozen stock of KAF 95 used in the experiments. (C) Growth curve for a frozen stock MG1655

based on the Sodium Motilty Buffer (abbreviated NMB) which is a 10 mM sodium phosphate buffer, pH=7.1 (an aqueous solution with 6.1mM of $Na_2HPO_4$, 3.9 mM of $NaH_2PO_4$) and 0.01 mM of Ethylenediaminetetraacetic acid (EDTA). Often swimming is assayed in a similar buffer, based on potassium rather than sodium phosphates but I opted for sodium as this makes the buffer not only unsupportive of growth but also preventing cell volume recovery after osmotic shock. Further buffers were made by adding osmolytes to NMB. All buffers and their contents are presented in Table 2.1 with osmolarity and pH data.

## 2.5 Sample Preparation

### 2.5.1 Bead Assay for Flagellar Motor Rotation

To detect the rotation of the flagellar motor, polystyrene $1\ \mu\mathrm{m}$ (Bangs Labs, USA) and latex $0.5\ \mu\mathrm{m}$ (Polysciences, USA) beads were attached to shortened flagellar filaments of cells that have previously been attached to the surface of the cover glass, setting up the experiment illustrated in Figure 2.4 B.
First, *Escherichia Coli* cells were grown until mid exponential phase (OD 0.7 to 1.0 at 600 nm) and an aliquot of 0.7mL was taken. It was subsequently passed

TABLE 2.1: Table of the main buffers and media used in the experiments together with their composition, osmolarity and pH

| Media/Buffer | Components | Osmolarity | pH |
|---|---|---|---|
| Sodium Motility Buffer (NMB) | 6.1 mM $Na_2HPO_4$<br>3.9 mM $NaH_2PO_4$ | 24 mOsm/kg | 7.12 |
| Tryptone Broth | Undefined growth media | 215 mOsm/kg | 7.08 |
| Volume Recovery Buffer (VRB) | NMB + 20 mM KCl<br>10 mM Choline Chloride<br>10 mM Glycine Betaine | 92 mOsm/kg | 7.04 |
| Modified Buffer 0 (MB0) | NMB + 40 mM KCl<br>40 mM Glycine Betaine<br>40 mM NaCl | 286 mOsm/kg | 6.90 |
| Modified Buffer 1 (MB1) | NMB + 80 mM KCl<br>80 mM Glycine Betaine<br>80 mM NaCl | 501 mOsm/kg | 6.87 |

through a shearing device to truncate the flagellar filaments. The device consists of two blunt tip 26G needles (McMaster-Carr, USA) connected with PEEK tubing (Outer and Inner Diameter: 1/16 in. ; 0.020 in., Sigma Aldrich, USA) (Chen et al., 2000a). To achieve good results, one syringe was driven with moderate speed while applying some resistance to the piston of the second and this was repeated until 35 back and forth cycles were complete. A good indicator of a successful filament truncation is a noticeable increase in the viscosity of the suspension.
Next, the sheared cells were taken out and centrifuged three times at 8000 RPM for 2 minutes, each time resuspending them into fresh buffer. Last resuspension was done in 0.3 mL of buffer, concentrating the bacteria.

**Preparing the “tunnel slide"**

A slide was prepared as shown in Figure 2.11 B by layering a glass slide and a coverslip between two strips of double sided sticky tape (Scotch), forming a channel of $2.2 \pm 0.2\text{mm}$ in width and 5-7$\mu$L in volume. Poly-L-Lysine (1% w/v, Sigma) was incubated for 10 seconds in the channel before being washed out twice with $100\mu\text{L}$ of buffer by adding the liquid to one side of the tunnel and withdrawing with a piece of tissue paper on the other. Cells were then added and incubated for 10 minutes in a humid environment to prevent evaporation. Subsequently, $100\mu\text{L}$ of buffer was flushed through the channel again

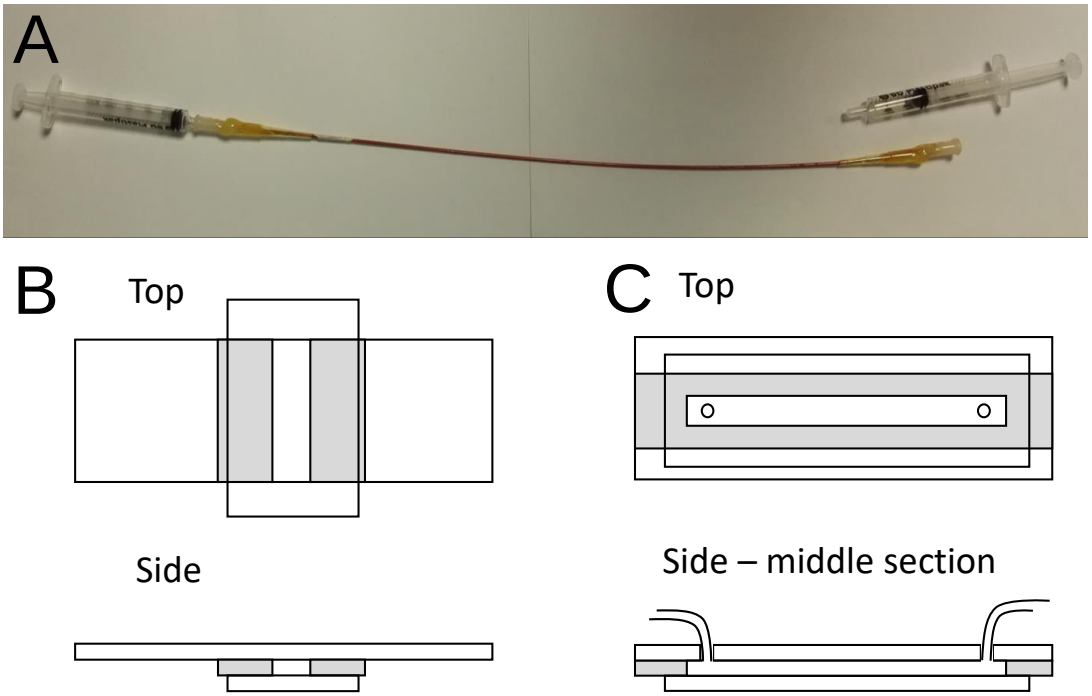


FIGURE 2.11: (A) Filament "shearing device" made of two blunt tip syringe needles (McMaster-Carr, USA) connected with PEEK tubing (Outer and Inner Diameter: 1/16 in. ; 0.020 in., Sigma Aldrich, USA). On each side, a 200 $\mu$L filled with a generous amount of epoxy resin glue is used to permanently attach the syringe needle to the tubing. (B) Top and side view of a tunnel slide. Two strips of double sided sticky tape (Scotch, USA - grey rectangles) are sandwiched between a slide and a cover slip. (C) Top and a side view of a flow cell made using a slide with two holes drilled into it, and plastic tubing attached to them using epoxy resin glue. Then, double sided tape (Scotch, USA) is placed over the holes and a channel is cut out. After gently wiping any residual glue with ethanol, a larger cover slip is placed over the tape to form a channel.

to remove cells that did not adhere to the poly-L-lysine coated surface and a suspension of beads in buffer was flushed in. After another 10 minute incubation and one more wash with $100\mu$L of buffer the situation of Figure 2.4 B had been set up within the slide and was ready for measurements.

### Flow Cell Preparation

When precise control of flow rate through the tunnel was necessary, a flow cell similar to the tunnel slide was prepared as shown in Figure 2.11 C. Two holes were drilled in a glass slide, $\sim$ 5 cm apart, and plastic tubing was attached to

them with epoxy resin glue. A piece of double sided tape was placed over the holes and a rectangular channel 3mm in width was cut out. A large (64mm) cover slip was then placed onto the tape. Sample preparation proceeded as with the tunnel slide with the only difference of using syringes to inject liquid into the tunnel instead of wicking through with a piece of paper tissue.

### 2.5.2 Cell swimming assay

MG1655 cells were grown as decribed in Section 2.4 and washed into VRB by pouring 10 mL of cell culture over a filter paper with $0.22\mu\mathrm{m}$ pores and letting the media seep through the paper. When very little ($1\mathrm{mL}$) was left, ($35\mathrm{mL}$) of VRB was poured over the paper. This process was repeated 3 more times. Afterwards, the suspension of cells in VRB was diluted until OD 0.9 and 250 $\mu l$ aliquots were made into microfuge tubes. For measurements of swimming speeds following osmotic shocks, 500 $\mu l$ of an appropriate solution of sucrose in VRB was added to the tube containing the cells, gently mixed and loaded into glass capillary tubes. The capillaries were then sealed and loaded into the microscope for imaging. The time between elevation of osmolality and the start of imaging was 2 minutes.

## 2.6 Laser Damage to E. Coli cells

Laser damage in optical traps has been found to be not due to heating of the cell (Neuman et al., 1999) but due to a single photon process which requires the presence of oxygen to damage the cell. In one study, the rotation of single *E Coli* cells, tethered to a surface by a flagellar filament, was used to assay the effect of laser damage on the proton motive force, a proxy for cell metabolism (Neuman et al., 1999). They found that damage exhibits two maxima (for 870 and 930 nm) and two minima (830 and 970 nm) with a five fold variation in $\mathrm{LD}_{50}$ between the minima and maxima. $\mathrm{LD}_{50}$ is the time it takes for the rotational rate to drop by 50%. Another study (Mirsaidov et al., 2008) looked at the effect of a 7-8 minute long exposure to a trapping laser on gene expression in E Coli. For continous wave optical traps, like the one used in my work, they find that deleterious effects of four studied wavelengths (840, 870, 900, 930 nm) are all within each others uncertainty. Combining data for continous wave and time shared (on-off) optical traps, they show that there exists a threshold energy of

2J after which cells start becoming non viable and at 5J only 50% of the cells are viable, as determined by whether or not they express a green fluorescent protein which was introduced as a marker of gene expression. Both of these studies find that the power dependance of damage is consistent with a single photon photochemical process but this process yet needs to be identified.

To estimate the power delivered to the cell we establish an upper bound by conservatively estimating the transmission losses of the laser beam passing through the optical elements on the way to the sample plane. Initial laser power, 24.5 mW, is attenuated to 18.6 mW after the ND filters. The f25 and f125 telescope lenses (Figure 2.1) will attenuate 8.2 and 2.5 % of the laser power according to their product specifications. The mirrors M6 and M7 have almost complete reflectivity, while D2 will contribute 3% to the power loss. Moreover, a Nikon objective from the same CFI Lambda family, but of lower magnification of 60x, reduces the power by another 30%. For a 100x objective this number is assumed to be higher due to additional lenses it contains within. Therefore, the power is further reduced to $0.61 \cdot 18.6\mu\mathrm{W}$, ignoring further loss due to the beam overfilling the objective back apperture. Lower bound was established by putting a photo diode power sensor in the sample plane, as close to the objective as possible, and this was found to be $0.4 \cdot 18.6\mu\mathrm{W}$. Thus, the post-ND beam is attenuated by a factor of $0.5 \pm 0.1$, which translates into an estimate of $9 \pm 2\mu\mathrm{W}$ of power delivered to the cell in the focus of the laser. Over a course of a typical 20 minute experiment this results in $10.8 \pm 2.4mJ$ of energy, greatly under the 2J limit at which the cell starts showing effects of damage through lower gene expression. Furthermore, for the wavelength used in this work, 855 nm, $\mathrm{LD}_{50}$ at a power of 100 mW is $\sim$ 500s (Neuman et al., 1999). To estimate the $\mathrm{LD}_{50}$ at $9\mu\mathrm{W}$, I use a simple laser damage model used in the aforementioned studies (Neuman et al., 1999; Mirsaidov et al., 2008)

$$S(P) = A + BP^n \tag{2.9}$$

where S is the sensitivity (inverse of $\mathrm{LD}_{50}$), A is the control sensitivity, which can be established by monitoring the damage from an ordinary bright field lamp, B is the wavelength dependent sensitivity and $\mathrm{P^n}$ is the power of the incident laser power onto the cell. The exponent, $n$ was determined in to be $\approx$ 1 (Neuman et al., 1999; Mirsaidov et al., 2008). Therefore the $\mathrm{LD}_{50}(15\mu\mathrm{W}) = \mathrm{LD}_{50}(100\mathrm{mW})(100\mathrm{mW}/9\mu\mathrm{W}) = 64.3$ days, well in excess of 500s. Additionally,

I have performed control measurements where I monitored the rotation of a BFM in an optical trap. The laser power was $9 \pm 2\mu\mathrm{W}$ and the results are shown in Figure 2.12, exhibiting no steady linear decrease of speed like the one reported in (Neuman et al., 1999). Furthermore, Chen and Berg (Chen et al., 2000a) have used a laser power of 2mW and their figures show a constant speed over 10 minutes.

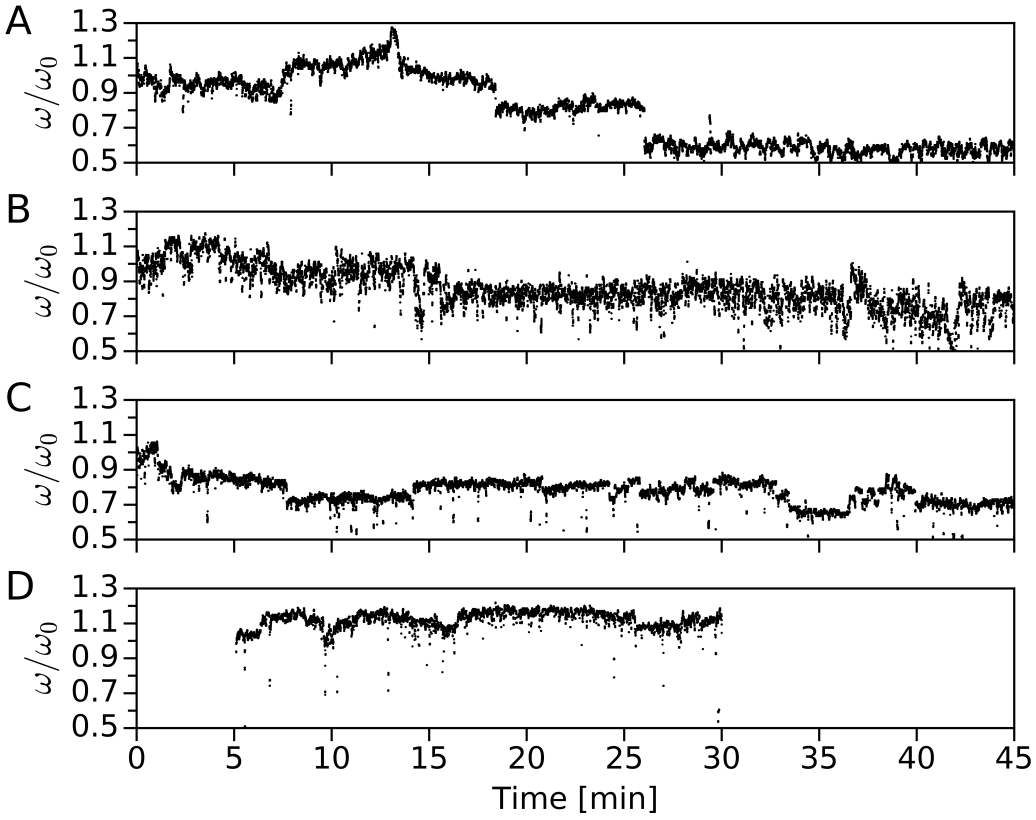


FIGURE 2.12: A,B,C: Laser power controls taken on separate cells in separate slides on different days. The traces show no behaviour consistent with laser damage (Neuman et al., 1999). The biggest changes in speed are observed in (A) but they are of stable step-like nature. D: A portion of rotation plotted after flushing in fresh buffer during recording, at t=5 minutes and acquired for 25 minutes without signs of laser damage. All speeds have been normalized to the initial value of speed for the respective recording.

## 2.7 Data Analysis

### Extracting Motor Speed

An example of the data collected from the PSD is shown in Figure 2.13 A and B. The points in panel A are voltages $(\mathrm{V_X}, \mathrm{V_Y})$, corresponding to the X and Y position of the bead and were sampled at a rate of 10 kHz. In panel B, these are plotted in an angle versus time representation. The coordinates were converted into speed data using a moving window Fast Fourier Transform with a “flat top" window of 1.6384s in duration. This window was chosen because it exhibited a good balance of signal to noise ratio and resolution, making it fit for analysis of long time traces with various features such as speed drops and varying levels of noise. An example speed trace obtained from the FFT is shown in Figure 2.13 C. Positive frequencies correspond to counter-clockwise (CCW) rotation of the motor and negative to clockwise (CW).

### Clockwise Bias of the Flagellar Motor

Clockwise bias of the flagellar motor is the fraction of time it spends rotation in the CW direction (Bai et al., 2010; Bai et al., 2013). Explicitly it is

$$CW\,Bias = \frac{N_{cw}}{N_{tot}} \tag{2.10}$$

where $N_{cw}$ is the number of data points corresponding to CW rotation and $N_{tot}$ is the total number of data points in a given time interval.

**Clockwise and Counter Clockwise Intervals** Clockwise and Counter Clockwise rotation interval lengths are extracted from motor speed data like that presented in Figure 2.13 C. In order for a CCW Interval to be counted, it needs to be bounded by two CW intervals. Thus, the initial and final stretch of CCW (+Hz) rotation in Fig. 2.13 C are disregarded as it is unknown when they begin or end, respectively. An analogous selection procedure applies for CW intervals.

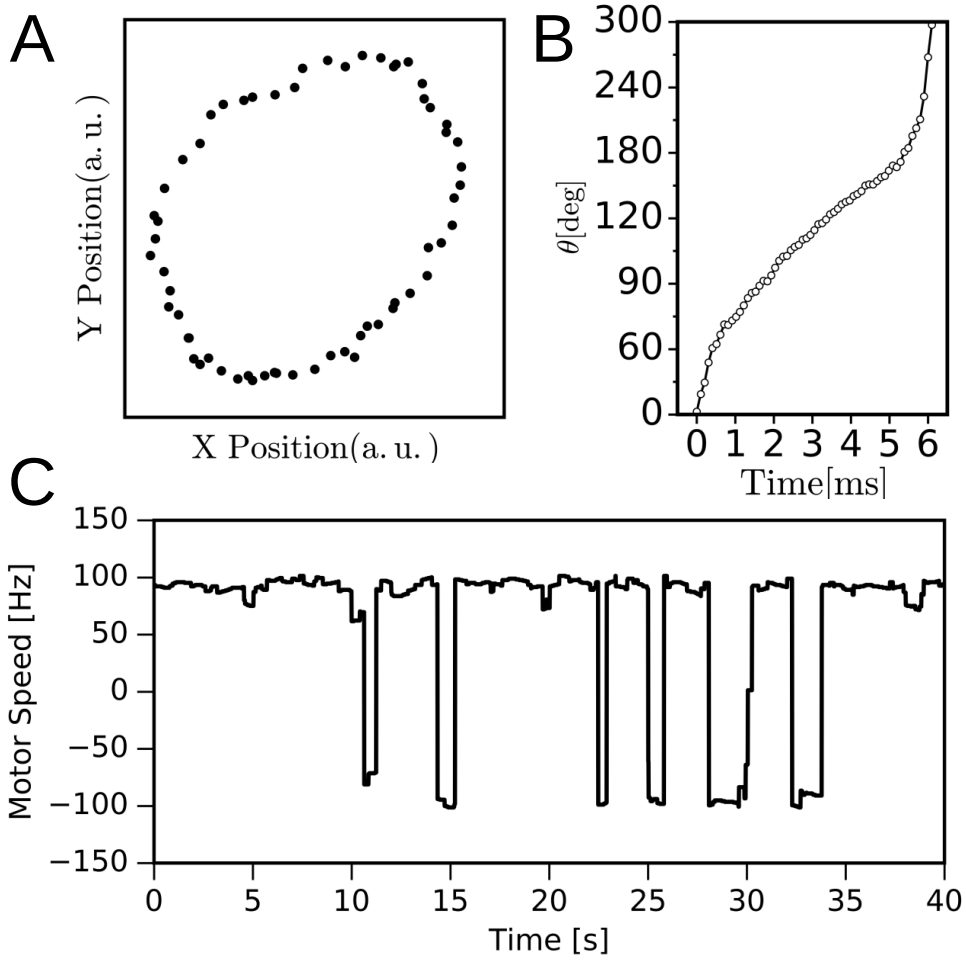


FIGURE 2.13: A: A single revolution of a flagellar motor driving a 0.5 $\mu$m bead at a speed of 166 Hz presented as $(V_X, V_Y)$ voltages from the PSD. B: The points from (A) plotted as angle versus time. C: An example of the output from a FFT analysis of PSD data for another cell.

# Chapter 3

# Results

## 3.1 Osmotic upshifts bring complex CW Bias dynamics

The chemotactic network, a sensory and signalling network, influences the way the flagellar motor rotates and thus facilitates cell runs or reorientations (Section 1.2). Because several network components, such as the chemosensors and parts of the signalling cascade, have shown activity during osmotic shocks (Vaknin et al., 2006), I begin this study by first looking at the bias of the BFM. Here the aim is to study the response to high osmolalities on a single cell, single motor level and compare the CW bias dynamics to those elicited through “conventional" chemical signals. Ultimately, I seek to understand how these CW bias dynamics could lead to cells accumulating in space away from sources of high osmolality, as has been observed before on agar plates (Li et al., 1988; Adler et al., 1988).

First I present a survey of steady state CW Biases in buffers of various compositions and using two bead sizes in the motor assay (Section 2.5). This was done as an initial step before settling on a buffer to use in further experiments. Then I give the CW Bias response to changes in osmolality, administered using sucrose. A complex response is revealed consisting of two phases, combining features characteristic for both chemorepellents and chemoattractants. Next, three different osmotic upshift magnitudes are presented. Then I ask the question whether there is any difference between osmotic upshifts of the same relative magnitude but with the cells starting at different initial concentrations. The subsections after that deal with extending the work to another solute, NaCl and verifying that CW bias indeed is a good proxy for motor switching (and consequently tumbling).

KAF 84 and KAF95 cells were grown as described in Section 2.4 and measurements were performed using the bead assay in tunnel slides (Section 2.5). CW Bias is extracted from BFM rotational speed traces as described in Section 2.7. When referring to CW Biases of a population of cells, unless otherwise stated, median quantities are given.

### 3.1.1 CW Bias in various media and buffers

In order to be able to detect both increases and decreases in CW motor bias, there needs to exist a sufficient bias baseline. Initial work was done in the sodium phosphate motility buffer (NMB) but the pre-stimulus bias there was 0.006 (Figure 3.1 A), too small to detect a potential drop caused by a reaction to a stimulus. In contrast, when the cells where suspended in tryptone broth (TB), the bias was comparatively much higher ($\mathrm{CW} = 0.132$, Figure 3.1 C). Since TB has an osmolality of 200 mOsm/kg, approximately 9 times higher than that of NMB (25 mOsm/kg), I decided to test the CW Bias in other buffers of higher osmolality. One of them, termed Modified buffer 1 (MB1), approximately of twice greater osmolality than TB (410 mOsm/kg) led to a CW Bias of 0.127. All of these tests were performed using polystyrene beads of $1\mu\mathrm{m}$ in diameter. However, in interest of larger resolution, I have later transitioned to $0.5\mu\mathrm{m}$ beads. These have a 2 times greater rotational speed and were chosen to allow me to discern finer speed changes (Section 3.2). In lieu of this, a re-evaluation of biases was performed with MB1 using $0.5\mu\mathrm{m}$ beads, producing a bias of 0.05, in contrast with the previous 0.127. This drop in CW Bias is consistent with data of (Fahrner et al., 2003) that shows a dependence of motor bias on the load it is driving. There, increasing the load leads to higher CW Biases. Another buffer, MB0, made by diluting MB1 with NMB in equal proportions showed a bias of 0.110 (Fig. 3.1 B). While these results do not establish a causal link between osmolality and bias, they indicated that a buffer with slightly more concentrated contents than NMB could provide a sufficiently high bias baseline. To allow the cells to recover their volume and ensure their survival of high osmolalities, NMB was supplemented with 20 mM potassium chloride, 10 mM choline chloride and 10 mM glycine betaine. Potassium, choline and glycine betaine act as osmoprotectants, compounds which are accumulated by the cell to help counter-balance an increased environmental osmotic pressure (Csonka et al., 1991; Wood, 1999). The new buffer, termed volume recovery

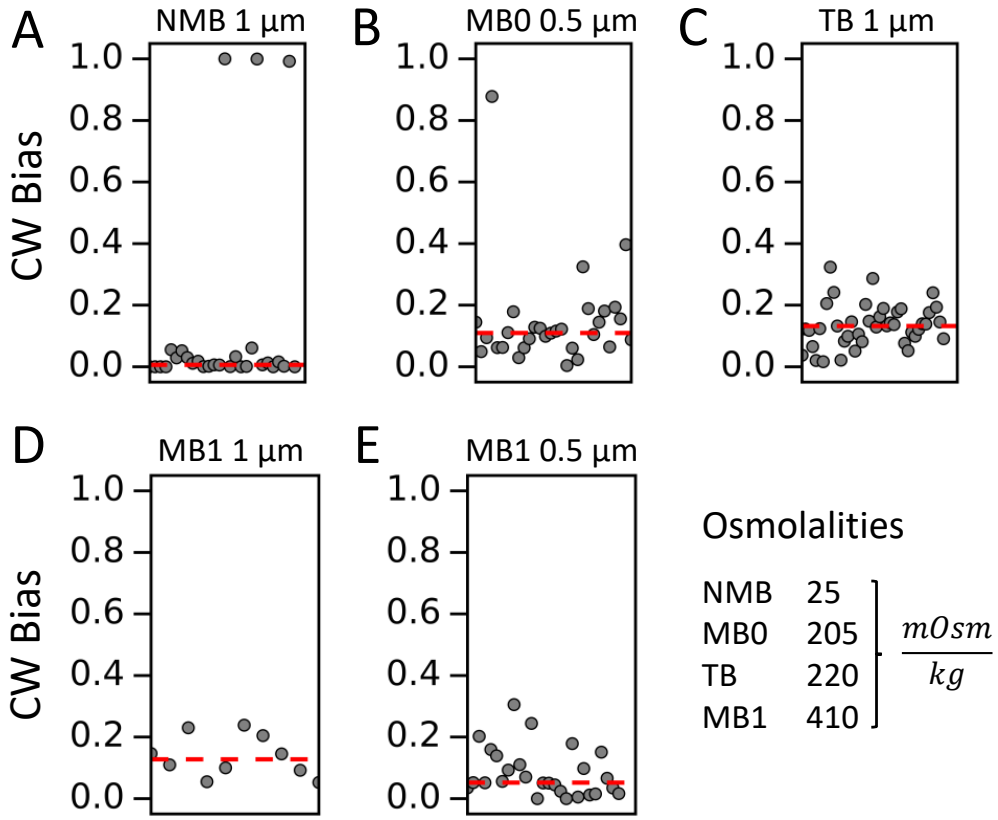


FIGURE 3.1: CW Biases in buffers and media of various osmolalities. Measurements were performed using two different bead sizes, of 1 and 0.5 micrometer diameters. (A) 28 motors on individual cells, driving $1\mu m$ beads, in Sodium Phosphate Motility Buffer (NMB) with a median CW Bias value of 0.006 (B) 30 motors in Modified Buffer 0, driving $0.5\mu m$ beads, with a median CW Bias value of 0.110 (C) 41 motors ( $1\mu m$ beads) in Tryptone Broth (TB) with a median bias of 0.132 (D) and (E) is a comparison between Modified Buffer 1 with motors driving $1\mu m$ (D) and $0.5\mu m$ (E) beads. The number of motors is 10 and 27, and the median biases are 0.127 and 0.05, respectively. Next to panel (E) are osmolalities of the buffers used in (A-E).

buffer (VRB) has an osmolality of 92 mOsm/Kg and a median bias of 0.08, $\sim$ 13 times bigger than the $1\mu m$ NMB bias. A full distribution of single cell, single motor VRB biases compiled from 120 recordings is shown in Figure 3.3 A.

### 3.1.2 The response of the BFM to an osmotic shock is complex

A representative measurement of the response of a single bacterial flagellar motor to an osmotic upshift is shown in Figure 3.2. Panel A shows a motor

speed trace obtained using the bead assay, described in Section 2.4. Positive speeds represent counter-clockwise (CCW) rotation and negative correspond to clockwise (CW). The former is associated with stable bundle formation and cell runs, while the latter with flagellar bundle destabilization and thus, cell reorientations. Initially the cell is in VRB and at $\mathrm{t} = 5\mathrm{min}$ the environment osmolality is elevated by exchanging VRB for VRB containing 400 mM sucrose. This is done over 10-15 seconds, flushing through 24 $\mu$l of the new buffer. The magnitude of the osmotic shock in terms of osmolality is 488 mOsm/kg.

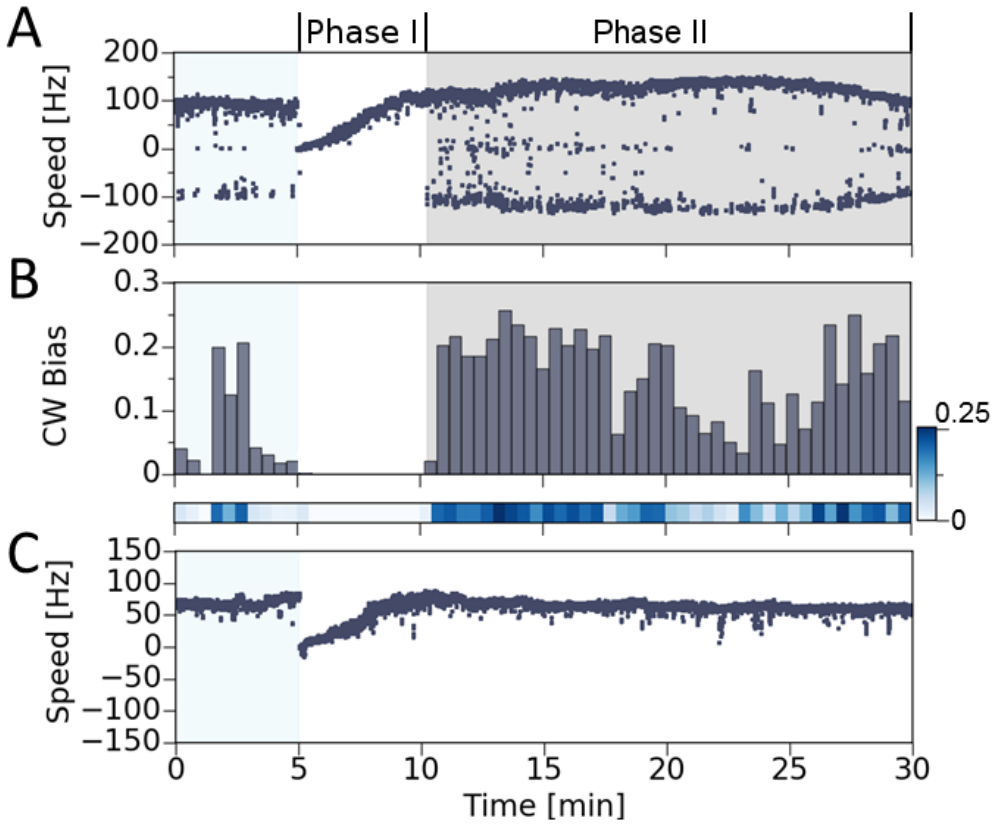


FIGURE 3.2: (A) An example 30 min speed trace obtained from a single BFM. The cell was initially in VR Buffer (Section 2.5), indicated in shaded light blue, and exposed to an osmotic upshock of 488 mOsmol/kg at t=5 min. The shock was delivered as a step increase by flowing in VRB containing additional 400 mM Sucrose, resulting in shock magnitude of 488 mOsmol/kg. (B) A histogram of clockwise bias computed by binning the trace in Fig. 1A into 30 second bins and dividing the time spent rotating clockwise by the bin length (see also equation 2.10 and Section 2.7). Below is the same histogram condensed into a color map, with an intensity scale to the right. (C) Single-motor speed trace of a $\Delta CheY$ mutant exposed to the same osmotic upshock as in Fig. 1A.

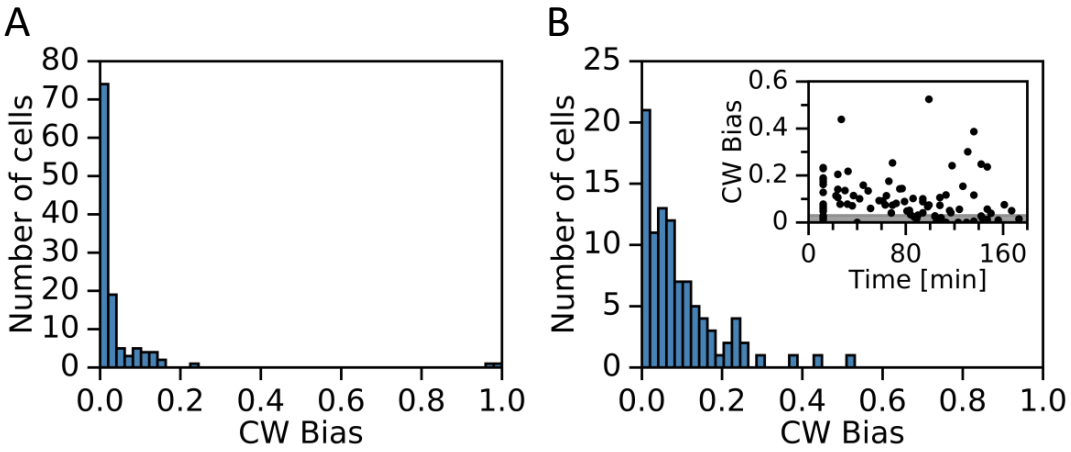


FIGURE 3.3: (A) Histogram of *CW Bias* for cells in Volume Recovery Buffer (VRB), prior to osmotic upshift. The histogram consists of 120 single motor recordings, each on a different cell and 3 minutes in duration. The biases were computed as described in Section 2.7 and sorted into bins of 0.02 in width. (B) Histogram of single cell, single motor biases after osmotic upshock, administered by exchanging VRB with VRB + 200 mM sucrose. 3 minute recordings were made 12 or more minutes after elevation of osmolality and bias was computed.Bin width is again set to 0.02 and the figure contains data from 96 cells. The inset plots these 96 single motor biases against the time after their respective osmotic upshift. Gray shading represents the range between $25^{\text{th}}$ and $75^{\text{th}}$ percentile of the CW bias distribution in VR Buffer given in A.

Prior to the stimulus, the motor is rotating with a CW bias of 0.07, similar to the median populational VRB bias of 0.08 (Fig. 3.3). Immediately following the buffer exchange, a distinct phase begins, termed Phase 1, where switching is entirely supressed. Another immediate consequence of an osmotic upshift with 400 mM sucrose is a sharp drop in motor speed, which then begins its slow recovery, eventually surpassing its initial value. The onset of switching, which happens in parallel with speed recovery, marks the beginning of Phase 2, which is characterized by a larger amount of motor switching events compared to the pre stimulus state. In this particular case, the CW Bias in Phase 2 is 0.16, opposed to the initial 0.07, and the heightened bias is maintained over a time scale of at least 20 minutes. The response to an osmotic upshift combines a supressed and an elevated bias, which are characteristic of two separate chemotactic responses, that to an attractant and to a repellent. It also shows no sign of complete adaptation, a defining characteristic of chemotaxis, where the

bias changes in response to a chemical stimulus only last several seconds before the bias resets. Here, the is no sign of complete adaptation of CW bias to initial levels over time scales as large as 20 minutes. Further, I investigated whether CheY protein, which relays chemotatic signals to the BFM, is needed for the CW Bias response to high osmolarity. If it were neccessary, this would be another piece of evidence for the implication of the chemotactic network in the osmotic response. Alternatively, if the response would proceed without CheY, this could indicate existence of another pathway processing osmotic inputs. Figure 3.2 C shows a ΔCheY cell responding to an osmotic upshift of 488 mOsm/kg in magnitude, administered at t=5 minutes.

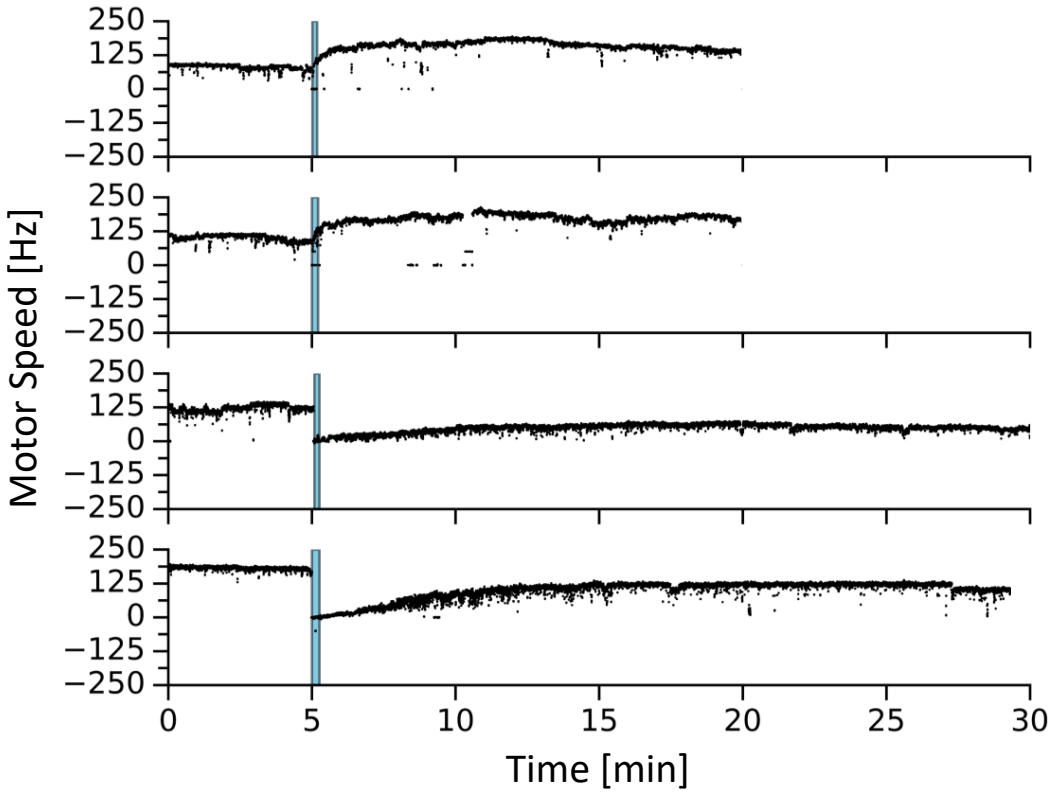


FIGURE 3.4: Top two: 20 minute long traces of motor rotation for KAF 95, a strain identical to KAF84 apart from being ΔCheY and thus unable to relay signals from the chemoreceptors to the flagellar motor. The blue shaded interval marks the delivery of osmotic shock using 100 mM Sucrose in VRB, a magnitude of 111 mOsm/kg. Bottom two: Longer sampling (30 minutes) and a greater shock, 488 mOsm/kg (400 mM sucrose).

Due to the lack of CheY the motors do not initially switch direction and this behaviour persists even after elevation of osmolality. Figure 3.4 shows

four more measurements using this strain, two with an osmotic upshift of 111 mOsm/kg and two more with a magnitude of 488 mOsm/kg. These implicate $\mathrm{CheY}$ in the CW Bias response to osmotic up-shifts.

### 3.1.3 Lack of adaptation over large time scales

To confirm the absence of adaptation at large timescales and to further investigate the dynamics of the CW bias single motor, single cell, measurements like that presented in Figure 3.2 were performed over several osmotic conditions. These conditions comprise upshifts in osmolality using sucrose in magnitudes of 111, 230 and 488 mOsm/kg, respectively. All measurements were performed using the volume recovery buffer and 22, 24 and 23 cells were collected for the aforementioned sucrose upshifts. A color map representation of the entire data set is shown in Figure 3.5 where each line represents a bias histogram for a single motor on a separate *E. Coli* cell. The process of collapsing single motor speed traces into colormap histograms is illustrated in Figure 3.2. Darker color represents higher CW Bias and white stands for lack of switching. The white, hatched column at $\mathrm{t} = 5\mathrm{min}$ contains the administration of the osmotic shock by flowing in the high osmolarity buffer for 10-15 seconds. In many cases, the flow pushed the bead to the edge of the laser focus and this causes artefacts in the Fourier transform analysis. Thus, this histogram bin has been excluded from the figure. Examining the color map in Figure 3.5 we see that Phase 1, the zero bias phase, scales with the shock magnitude. Its duration, several minutes, is of similar magnitude as the time it takes the cell to recover its volume following a hyperosmotic shock (Pilizota et al., 2012; Pilizota et al., 2014). The elevated bias of Phase 2 and lack of complete adaptation are present across the entire dataset of 69 cells. To present the data in a more quantitative fashion, Figure 3.6 B-D plots each of the three conditions from the color map in the form of a CW Bias median, mean and the interquartile range. The biases therein are computed using a moving window of 60 seconds in width. Additionally, Figure 3.6 A shows the same kind of plot, but for a buffer to buffer control, to assay the potential effect that merely flowing in fresh buffer would have on the CW Bias. There is at best an effect comparatively small to osmotic upshift conditions of panels B-D. To compare the median bias traces of the three osmotic conditions to each other, I present them together in Figure 3.7 A,

where once again we notice the scaling of Phase 1 with shock magnitude. Figure 3.7 B explicitly shows Phase 1 duration versus osmotic shock magnitude.

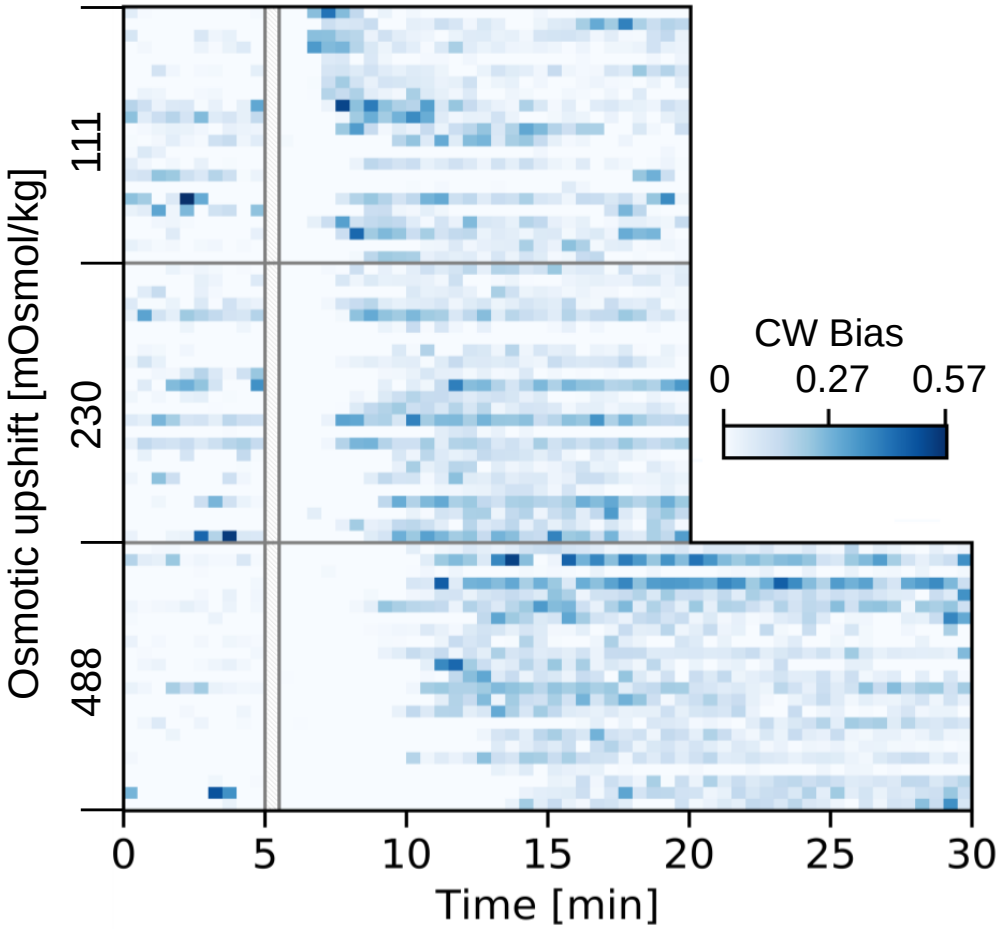


FIGURE 3.5: Stacked single cell color maps (histograms) of *CW Bias* for three different shock magnitudes (indicated on the left). Bin widths are 30 s and the process of obtaining a single cell color map is illustrated in Figure 3.2. VR Buffer was exchanged for the same buffer with the addition of sucrose at t=5 min. The white hatched column represents the period of the media exchange which lasted for ∼10-15 s. 22, 24 and 23 cells are given for the 111, 230 and 488 mOsmol/kg condition, respectively. These upshift correspond to sucrose concentrations of 100, 200 and 400 mM. The color map scale is given at the side of the figure.

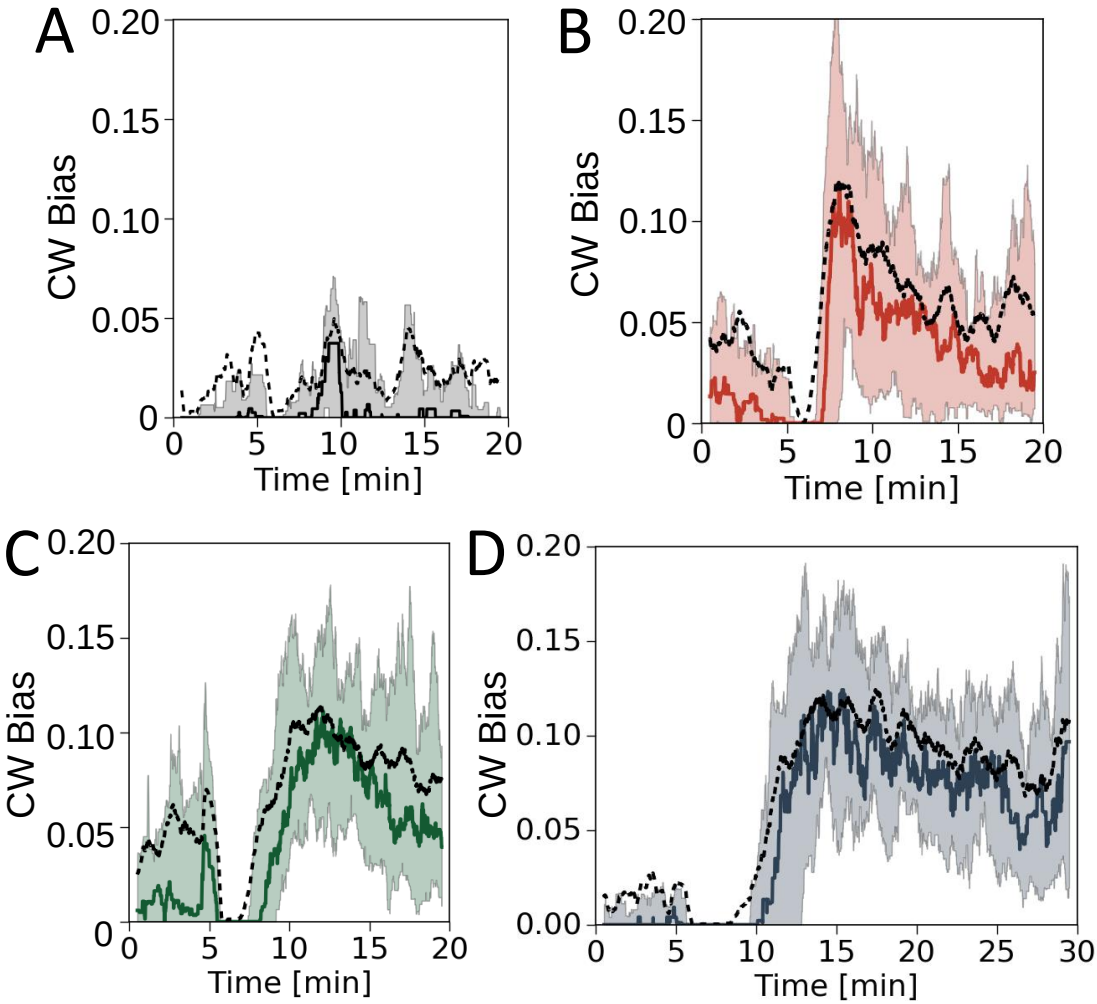


FIGURE 3.6: (A) Buffer to buffer control experiment. CW Bias was computed from 12 single cell, single motor recordings. The black solid line is the median bias of those 12 cells, the dashed line represents the mean and the grey shading is the area between the 25th and the 75th percentile. At t=5min fresh buffer was flown around the cell and rotation was recorded for 15 more minutes. CW Bias was calculated from motor speed recordings using a 60s wide moving window. (B) Same as A but for the 111 mOsmol/kg osmotic upshift and the plot represents the median of the 22 single cell bias traces (thick red line), the mean (dashed black line) and the red shading is the area between the 25th and the 75th percentile. (D) and (E) are the same as C, only for the 230 mOsmol/kg (24 cells) and the 488 mOsmol/kg (23 cells) osmotic upshifts, respectively.

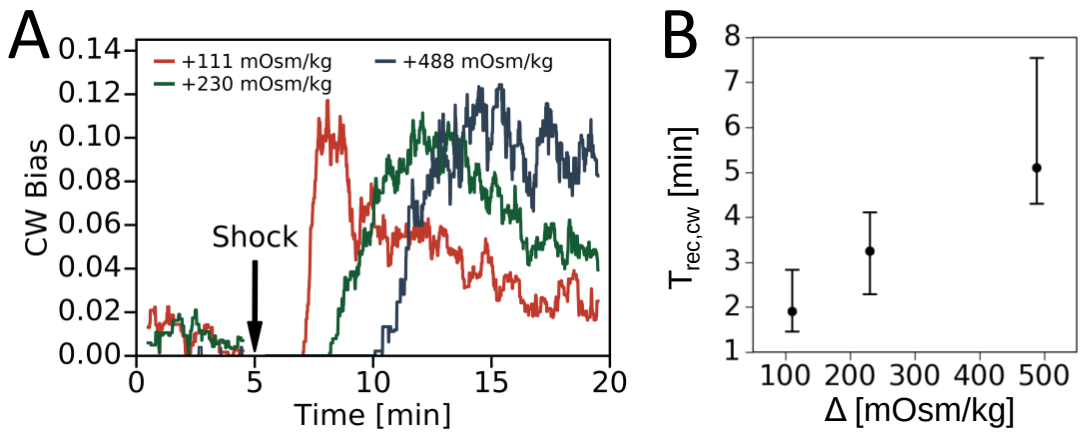


FIGURE 3.7: (A) Median population *CW Bias* in time, computed from cells given in Figure 3.5, for different shock magnitudes: 111 mOsmol/kg (red), 230 mOsmol/kg (green) and 488 mOsmol/kg (dark blue). Black arrow indicates the time at which hyperosmotic shock was administered. (B) Recovery Phase duration ($T_{rec,CW}$), calculated as the time needed for the post-shock median population bias (panel A) to recover to the median VR Buffer bias (CW Bias=0.01, Figure 3.3). $T_{rec,CW}$ was calculated for each of the three shock conditions, whose biases are presented in panel A and also in Figure 3.6. The points represent times at which the post shock median reaches 0.01, relative to the time of shock delivery. The error bars give the populational variability in terms of recovery times for the 25th and the 75th percentile of population bias.

### 3.1.4 CW Bias might respond to relative changes in osmolality

To investigate whether the motor responds to relative changes in osmolality I have performed an experiment where I have initially washed cells into VRB with addition of 100 mM sucrose. Then, in a bead assay experiment I performed another osmotic upshift, using 200 mM sucrose in VRB. This amounts to a relative osmotic upshift of 119 mOsm/kg. In Figure 3.8 I plot the result of this experiment together with the 111 mOsm/kg osmotic upshift of Figure 3.7. The two traces show striking similarity with only a slight difference in the initial CW Bias and the 119 mOsm/kg shock having a shorter Phase 1. It is not clear whether this Phase 1 shortening is related to already having been through an osmotic shock of that magnitude during sample preparation and potential accumulation of osmoprotectants from the buffer, which could in turn help the cell recover volume more readily.

Comparing Figure 3.8 with Figure 3.7 A, one might be tempted to conclude that the flagellar motor measures relative, rather than absolute changes in osmotic pressure, but such a conclusion would need a lot more data. At present,

this result best serves as guide towards further experiments.

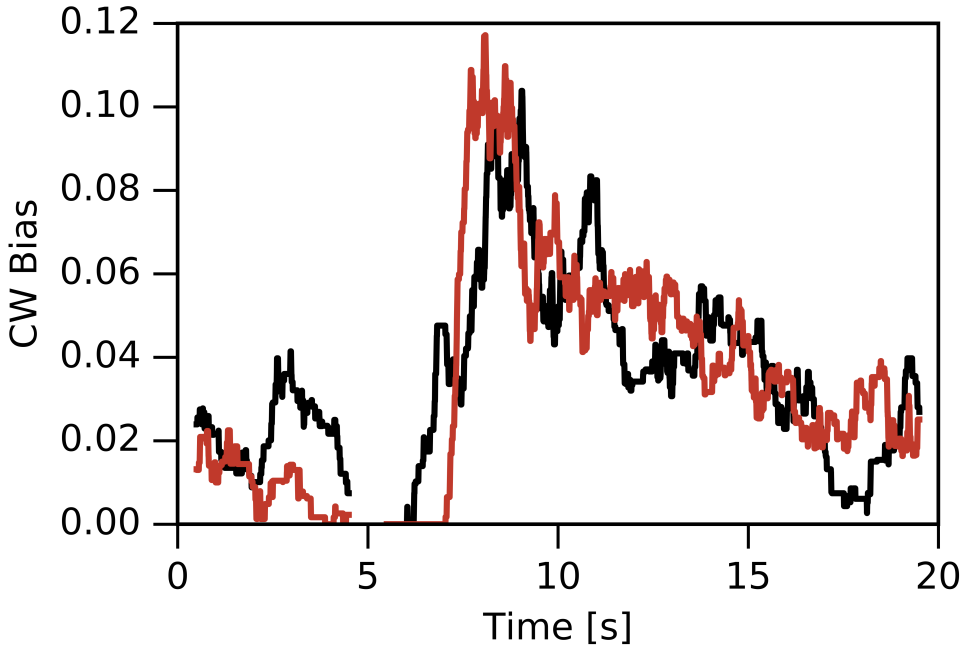


FIGURE 3.8: A comparison between an osmotic upshift experiments going from VRB to VRB + 100 mM sucrose, given in red (also in Figure 3.7 A), and an experiment where this shock was already performed during sample preparation and another upshift of the same magnitude was performed in the microscope. During this upshift, VRB+100 mM sucrose was exchanged for VRB+200 mM sucrose. This data is represented by the black line

### 3.1.5 Extending the measurements to NaCl

Historically, apart from sucrose, sodium chloride has also been extensively used to elevate osmolarity in experiments. Thus, looking to extend my measurements to investigate the effect of different solutes, I have turned next to NaCl. Here there appears to be greater variability in the response as several cells in the 93 mOsm/kg condition appear not to respond at all. Despite that, on average there is an increase in CW Bias following osmotic shock, in agreement with the data for sucrose. More experiments are necessary to build up statistics for analysis of bias dynamics.

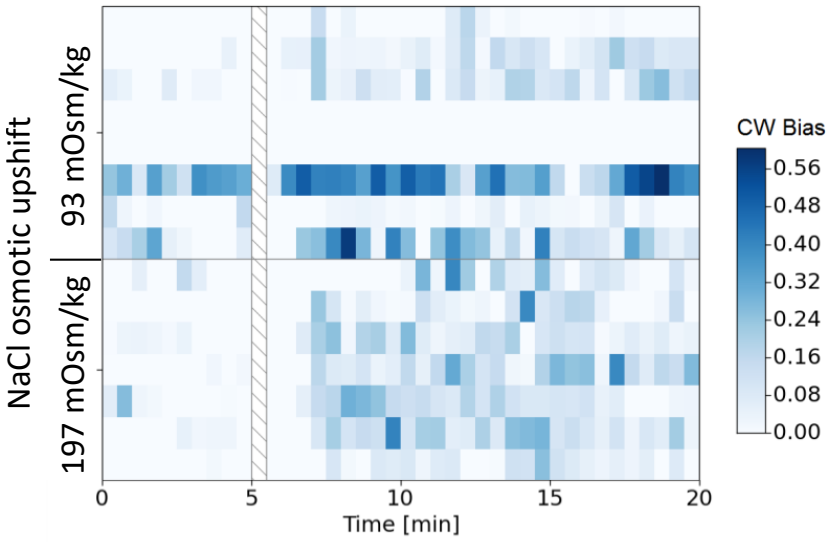


FIGURE 3.9: A color map for osmotic shocks performed with sodium chloride. Each line represents a single motor on an individual cell. VRB was exchanged for VRB with addition of NaCl at t=5 and the white hatched column represents this media exchange. Color map bin width is set to 30s, like in Figure 3.5. A scale is given on the right hand side. A total of 8 and 7 cells were analysed for the 93 and 187 mOsm/kg conditions.

### 3.1.6 CW Bias is proportional to the number of switches

When studying chemotaxis using the single motor CW Bias, one assumes that there is a correlation between CW Bias and the switching frequency (SWF). That is, if the bias increases this is because there are more CCW-CW switches and consequently more free swimming cell reorientations. To verify that this indeed is the case and the elevated CW Bias is not merely a consequence of longer CW intervals, I counted the number of CW intervals in the rotation samples used to calculate CW Bias. Figure 3.10 A shows the switching frequency, the number of switches per minute, against the corresponding motor bias for volume recovery buffer. The quantities were calculated from 3 minute long samples of single motor rotation. Since this buffer produces a low steady state bias we do not have a large range of values to work with. However, although with a wide spread, the points seem to group around a line indicating a proportionality between SWF and CW Bias. Figure 3.10 B shows the same VRB points in black but overlayed with a post osmotic shock sampling of the dataset from Figure 3.5. The sampling was done by taking a section between t=17 minutes and t=20 minutes. The larger range of biases available in this

condition supports the idea of a linear correlation of SWF and CW Bias. Ideally, in both conditions the slopes would be the same but VRB seems to have a slightly smaller number of switcher per unit bias. At this point we can not say much about the origin of the slope difference without measuring $CheY - P$ concentrations and scanning the full range of biases with more points to reduce experimental uncertainties. However, what we can say is that in our

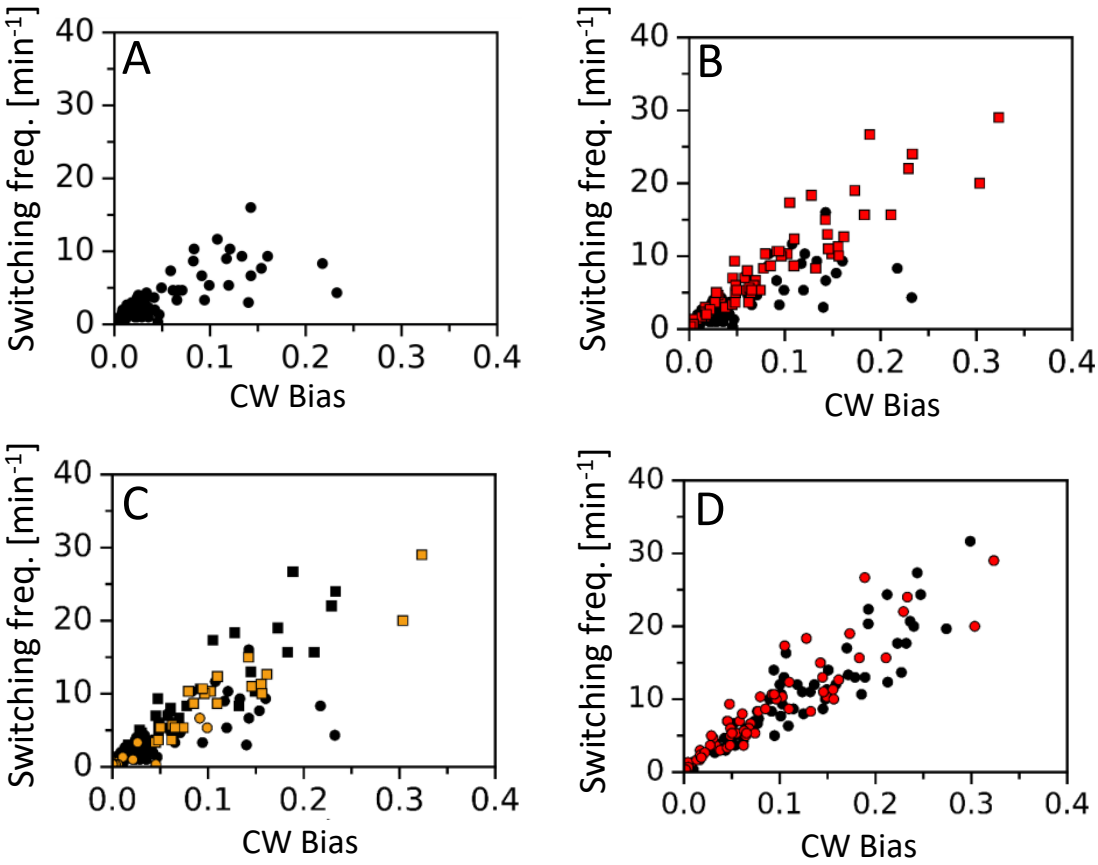


FIGURE 3.10: Switching Frequency vs CW Bias. Switching frequency is computed by counting the number of CW intervals in a 3 minute long sample of motor rotation and divided by 3. (A) SFW vs CW Bias for 102 single motor (single cell) 3 minute samples of VRB rotation, shown with black circles. (B) As in (A), the black circles are VRB points and red squares are a sample taken between t=17 and t=20 of the VRB Sucrose shock dataset shown in Figure 3.5. (C) Same data as in (B) but this time the circles (VRB) and squares ($t \in [17, 20]$) for samples from the 488 mOsm/kg condition of Figure 3.5 are orange and other samples are black. (C) Red is the ($t \in [17, 20]$) sampling of Figure 3.5, already presented in (B) plotted alongside an alternative sampling where each cell was sampled for 3 minutes starting from the point where it started switching again, following an osmotic shock (black circles).

range of interest, the relationship is linear and that, after osmotic shock, there could be more switches per unit bias. If the latter is real, this would mean that the post shock CW bias increase signal is even stronger because it corresponds to even more motor switches. A different angle is presented in Figure 3.10 C where both VRB (circles) and shock dataset points (squares) are orange if coming from the initial 3 minutes or the t=17 to t=20 interval of only the 488 mOsm/Kg dataset from Figure 3.5. Everything else is shown in black. This way we can follow the same set of cells as they transition from VRB to high osmolality. In this instance, there is no apparent sign of two slopes. In panel D, the osmotic shock dataset is sampled in the $\mathrm{t} \in [17, 20]$ interval (red) but also in an alternate way where each cell is sampled from 3 minutes from the moment it recovered switching. Both ways of sampling, despite being removed in time from each other, fall on the same line.

Another result that supports the claim that the increase in CW bias is due to more switches and not longer switches, is given in Figure 3.11 in the form of mean CW interval distributions for populations of cells in VRB (102 cells) and in VRB + 230 mOsm/kg sucrose (88 cells). The average cell in VRB has a mean CW interval of $\overline{\tau}_{\mathrm{CW}} = 0.61 \pm 0.05$ seconds, while that in the VRB + 230 mOsm/kg condition is characterised by one lasting $\overline{\tau}_{\mathrm{CW}} = 0.64 \pm 0.05$ seconds. Interestingly, while the distribution means are practically equal, the spread appears to be smaller in the condition of higher osmolality. The inset of Figure 3.11 B gives the VRB + 230 mOsm/kg $\overline{\tau}_{\mathrm{CW}}$ values against the time the motor rotation was sampled, relative to the delivery of osmotic shock. We notice that the values are steady for at least 100 minutes, revealing that there are no temporal dynamics at work. Thus, the CW Bias is a good proxy for the number of switching events in the conditions examined in this chapter.

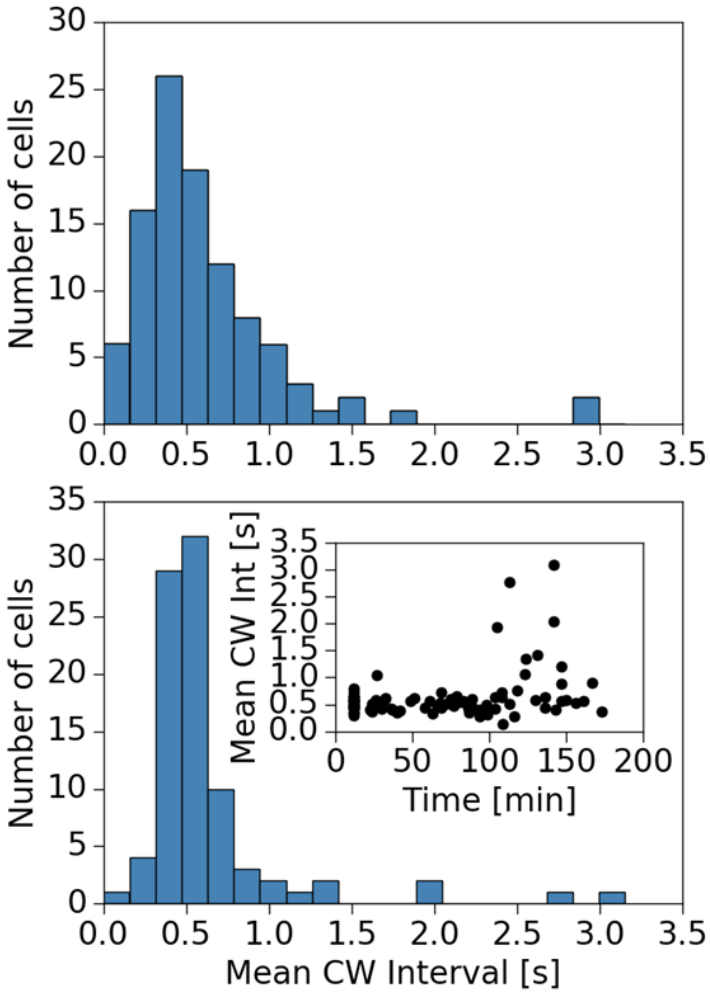


FIGURE 3.11: A: Mean CW interval distribution ($\overline{\tau}_{CW}$) for cells in Volume Recovery Buffer. Motor rotation of 102 cells was sampled for 5 min and single motor intervals calculated as outlined in Section 2.7. B: Distribution of average CW intervals for motors where the sampling interval (3 min) begins 12 or more minutes after an osmotic shock with 200 mM sucrose in VRB (+230 mOsmol/kg). The inset contains data from the histogram plotted against the start time of the sampling interval and t=0 corresponds to the osmotic shock. Intervals for VRB were sampled for longer as there are less events per unit time and longer sampling allows the estimation of a single cell mean interval with less uncertainty.

## 3.2 Osmotic upshifts give long term increases in speed

Part of this work, on the effects of osmotic upshifts on populations of swimming cells using differential dynamic microscopy (Section 2.3), was conducted in collaboration with Vincent Martinez. I have grown cells, prepared samples and interpreted the data. Vincent Martinez performed the imaging and the calculations of swimming speeds.

Changes in motor speed, like changes in CW Bias, can drive accumulation (Schnitzer et al., 1990; Demir et al., 2012). Thus, I continue the investigation of steps in osmolality, administered by sucrose, with an analysis of changes in motor speed but also in population swimming speed. I begin with a survey of speeds in various buffers, important for having a point of reference for possible increases or decreases observed later with osmotic changes. Then, I characterize the changes in motor and population swimming speeds in response to steps changes in osmolality. In the subsequent subsection motor speed reversibility upon a step down in osmolality is revealed and following that, it is explored whether there is any difference, in terms of final speed, between elevating osmolality in one or several steps. The next subsection takes a closer look at the nature of the speed recovery following a drop to $\sim 0\mathrm{Hz}$ in response to the strongest, 488 mOsm/kg, osmotic shock. After performing a preliminary analysis of the possible number of stator units associated with the motor before and after an osmotic shock, I present the work done on extending the measurements to another solute, NaCl. Ultimately, a result from the literature on CCW-CW speed asymmetry is confirmed (Yuan et al., 2010).
KAF 84 and KAF95 cells were grown as described in Section 2.4 and measurements were performed using the bead assay in tunnel slides (Section 2.5). MG1655 cells for populational swimming studies using differential dynamic microscopy were grown and prepared as described in Section 2.3.

### 3.2.1 Flagellar motor speed in various buffers

I begin the investigation of motor speed by assaying the speed magnitude with two different bead sizes, $0.5\mu\mathrm{m}$ and $1\mu\mathrm{m}$, and in various buffers and media. Figure 3.12 shows histograms of motor speeds in sodium motility buffer (NMB), presented on panel A, and in tryptone broth (TB), presented on panel B. Single motor rotation was sampled for 10 seconds for both conditions and 95

motors on individual cells were assayed for NMB and 41 for TB. Experiments were carried out using $1\mu m$ beads and it was found that the mean speed in NMB is $48.6 \pm 1.5$Hz, while that in TB is $43.0 \pm 2.0$Hz. The inset of Figure 3.12 A shows a CW Bias distribution computed from the 10 second samples of motor speed with a median value of 0.06.

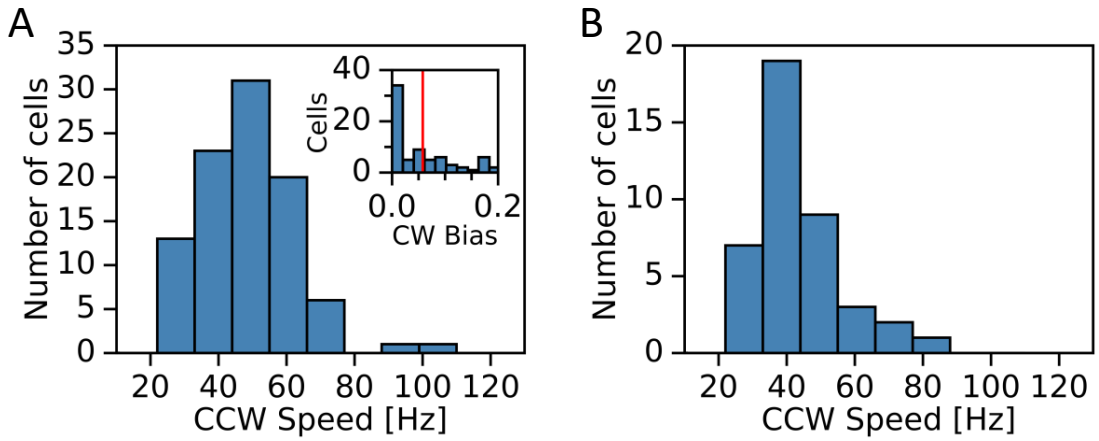


FIGURE 3.12: Motor speed histograms computed from 10 second samples of single motor rotation, each from an individual cell. Bin widths are set to 10 Hz and 1 micrometer in diameter polystyrene beads were used in the bead assay. A: Measurements were performed in NMB. The inset is a histogram of motor biases computed from these samples. 95 cells were recorded in this condition. B: Measurements performed in TB on 41 individual motors on separate cells, using 1 micron beads. Mean speed in NMB is $48.6 \pm 1.5$Hz, while that in TB is $43.0 \pm 2.0$Hz.

The third buffer examined with use of $1\mu m$ beads was that Modified Buffer 1 (MB1), where 10 motors spun with an average speed of $55.0 \pm 1.2$Hz, shown in Figure 3.13 B. Wanting to increase the sensitivity of the experiments to changes in motor speed, I transitioned from use of $1\mu m$ beads to $0.5\mu m$ beads. In contrast with the larger, $1\mu m$ beads, these rotated at an average speed of $94 \pm 7$Hz in MB1. The speed was measured on a sample of 27 motors and is presented in Figure 3.13 C. In MB0, a half concentrated version of MB1, 30 motors driving half micron beads were recorded spinning at $82 \pm 3$Hz (Figure 3.13 A).

Buffers MB0 and MB1 were created because, unlike NMB, they contain potassium and other osmoprotectants, enabling the cell to recover volume post osmotic shock (Csonka et al., 1991; Wood, 1999). The composition, osmolalities and pH values of the buffers used are summarised in Table 2.1 of section 2.4. The final choice of experimental buffer is similar in composition to MB0 and

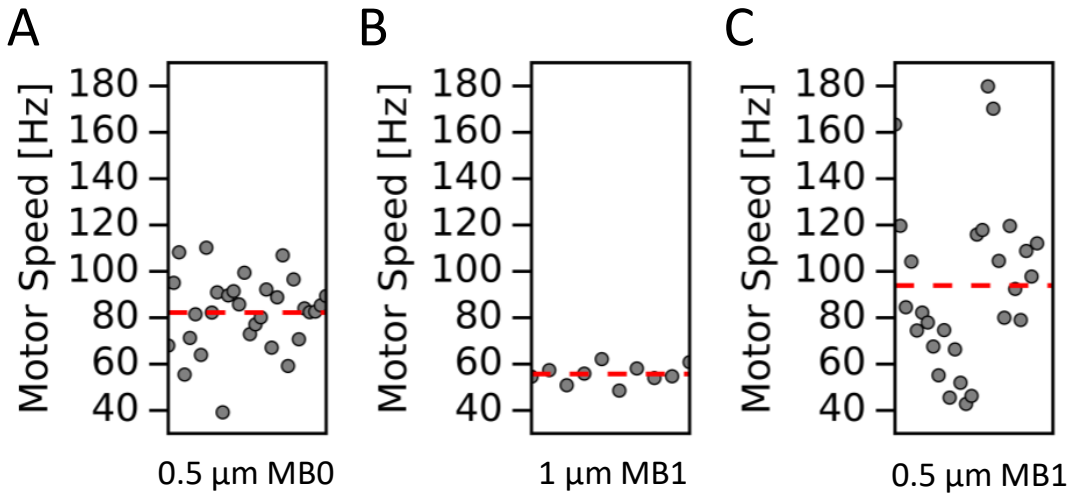


FIGURE 3.13: Motor speeds in various buffers. A: Each point represents a single cell, single motor speed value in MB0 buffer, where $0.5\mu$m beads were used in the bead assay. B: Measurement in MB1 buffer using $1\mu$m beads. (C) Speeds obtained using $0.5\mu$m beads in MB1. Dashed red lines represent mean values which are $82 \pm 3$Hz, $55.0 \pm 1.2$Hz and $94 \pm 7$Hz, for A, B and C respectively.

MB1. This buffer is termed VRB for volume recovery buffer and includes an NMB base with 20 mM of potassium chloride, and 10 mM each of choline chloride and glycine betaine. A speed histogram composed of 10 second samples of motors driving half micron beads is presented in Figure 3.14. This distribution has a mean value of $107 \pm 2$Hz and a median of $102$Hz.

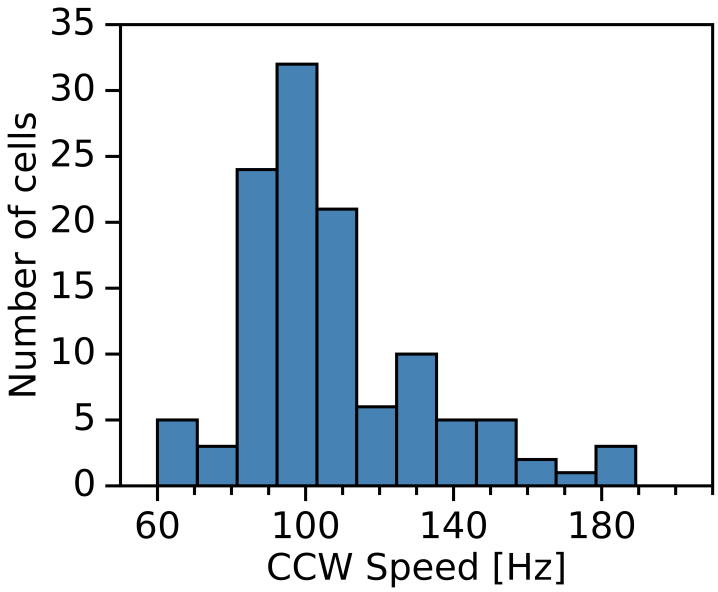


FIGURE 3.14: A histogram of 118 single cell, single motor speeds obtained from 10 second samples of motor rotation in VRB. Half micron in diameter beads were used in the bead assay. The bin widths are set to 10 Hz and the mean and median values are $107 \pm 2$Hz and 102Hz.

### 3.2.2 Motor and swimming speed increase when osmolality is elevated

Figure 3.15 shows examples of single motor rotation traces in VRB before and after an osmotic upshift. Only CCW speeds are shown for clarity, as CW speeds follow the same trend. Interestingly, just exchanging VRB for VRB by means of flow results in an instantaneous jump in motor speed as can be seen from Figure 3.15 A. When VRB is exchanged for VRB + sucrose in an amount that constitutes an osmotic shock, motor speed shows two types of behaviour depending on the shock strength. The first kind of behaviour is in response to changes in sucrose concentration of 100 and 200 mM. These change the extracellular medium osmolality to 111 and 230 mOsm/kg, respectively. Examples of speeds of motors exposed to these two magnitudes are given in Figure 3.15 B and C. Like with just flow, here the speed also rises but the change lasts longer. The second kind of response is to a very high osmotic shock, such as that brought by adding 400 mM sucrose, giving a change in osmolality of 488 mOsm/kg. One example is given in Figure 3.15 D. Here the speed immediately drops to zero, subsequently enters a period of recovery which then leads to an elevated level of motor speed.

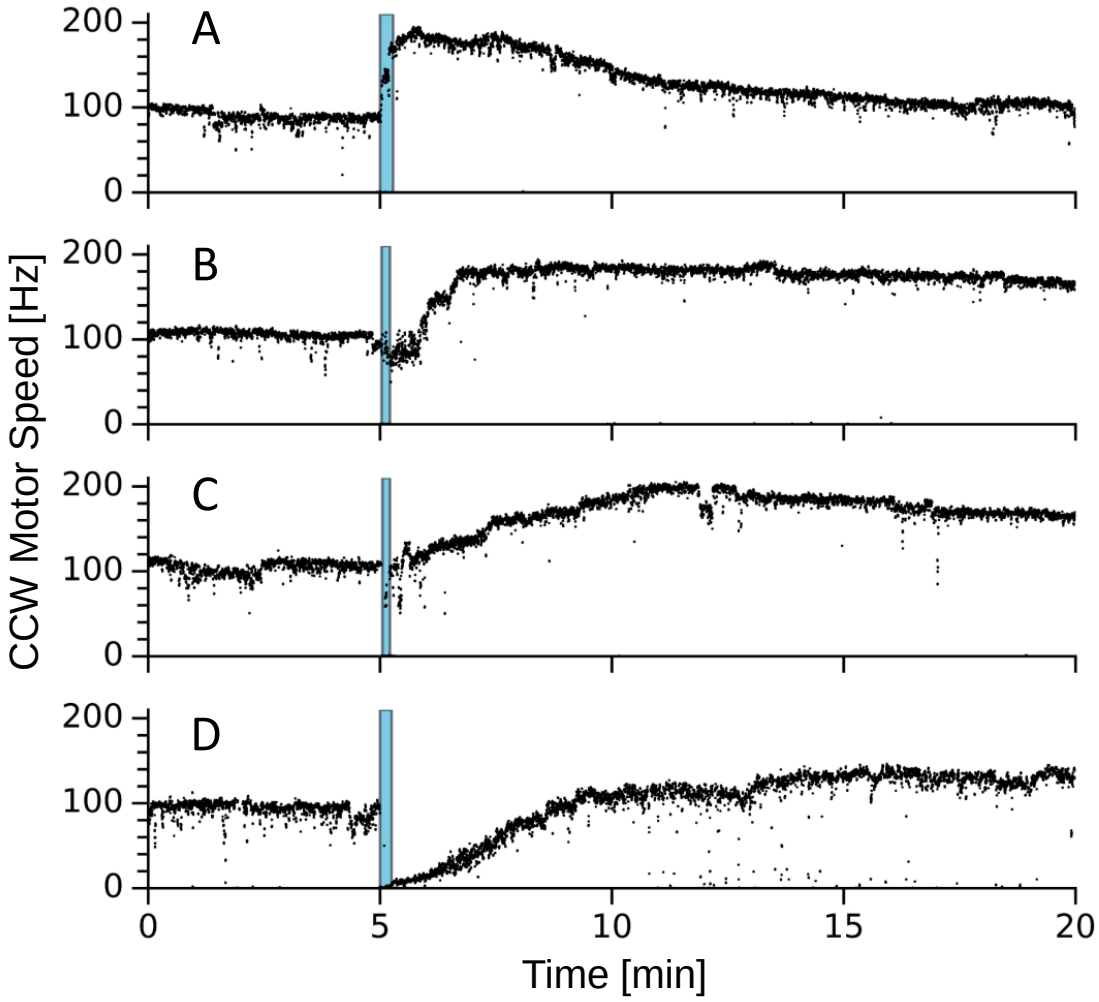


FIGURE 3.15: Examples of experimental results for osmotic up-shifts with sucrose. VRB is exchanged for VRB + Sucrose at t=5 minutes by flow, indicated with the blue shading on the traces. A: Control experiment where VRB is exchanged for VRB. B: VRB + 100 mM Sucrose is flown in, constituting an osmotic upshift of 111 mOsm/kg. C: 200 mM sucrose in VRB is added, shifting the osmolality up by 230 mOsm/kg. C: Highest upshift studied, 488 mOsm/kg, delivered by flowing in VRB + 400 mM sucrose

**Overview of the entire dataset confirms long term speed increases**

The full dataset for sucrose upshifts in VRB contains 12 cells in the flow control group, 22 cells in the 111 mOsm/kg group, 24 for 230 mOsm/kg and 23 for 488 mOsm/kg. To present them in a compact representation I first select only the CCW speeds and a color map is then constructed following the same procedure illustrated in Section 3.1.3 for Figure 3.5. Briefly, the single motor traces are divided into 15 second segments, and an average speed is computed for every segment. The trace then becomes an array of 15 second wide squares, coloured according to the speed magnitude. Ultimately, these are stacked one onto another, giving rise to Figure 3.16, where each row represents a single motor on an individual cell. The colour scale is given on the side of the figure. Additionally, speeds are presented normalised to the value of the first bin.
Now we are able to see that, indeed, for smaller shock magnitudes such as 111 and 230 mOsm/kg, the speed shows a long term increase relative to the pre stimulus levels. Furthermore, larger shocks, like the 488 mOsm/kg condition first show a drop and then, in most cases, an increase in the speed of motor rotation.
In order to uncouple the effect of the flow and the effect of osmolality, we consider a sample of the Figure 3.16 colour map dataset taken between t=17 and t=20 minutes, assuming that by this time, any transient behaviour that was due to flow will have dissipated and only the reaction to osmolality will have remained. Then I compute the average speeds for each trace, grouping them by the condition they belong to and calculate the mean population motor speed. To make meaningful comparisons, the average motor speed in VRB is also calculated for each experimental condition. While the osmotic shock conditions experience relative increases in $T_{17-20}$ relative to VRB of $28 \pm 8$, $33 \pm 7$ and $23 \pm 6$ Hz, the relative increase for the flow control group is $7 \pm 8$ Hz. Individual values of speeds with means and medians are presented in Figure 3.17 A for the $T_{17-20}$ interval and Figure 3.17 B has the corresponding values for VRB. Thus, osmotic changes produce a clear long term change in motor rotation, markedly above the baseline effect of the flow itself.
The colour map of Figure 3.16 and also the data presented in Figure 3.17 indicate that the relative speed increases compared to VRB are lower in the strongest, 488 mOsmol/kg condition, compared to the two lower osmolalities.

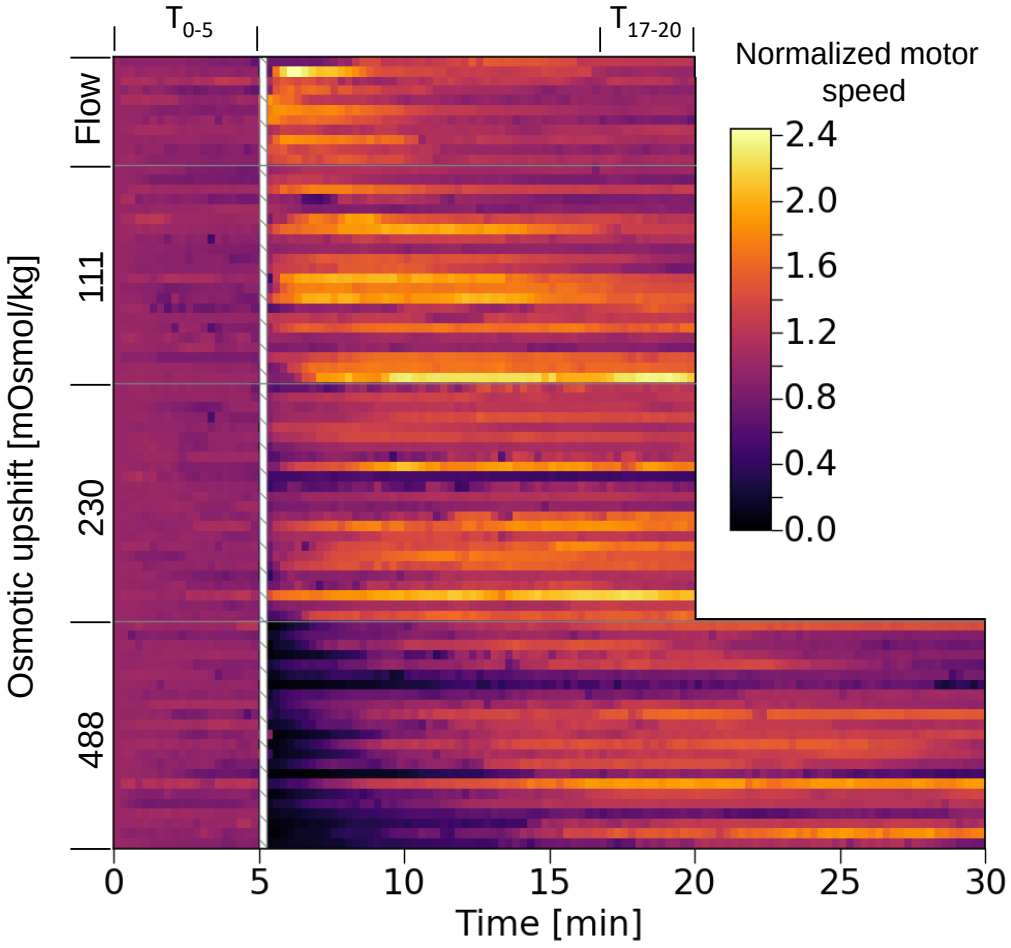


FIGURE 3.16: Stacked single-motor (also single-cell) speed histograms, where the speed for each BFM is normalized to the average value of the first 15 s. Bin widths are 15 s and the color represents the bin height. Results are grouped by upshock magnitude, as indicated on the left hand edge. The white hatched column represents the point where an osmotic shock was performed by exchanging VR Buffer for VR Buffer + sucrose and the flow lasted for 10-15 s. 12, 22, 24 and 23 cells are given for the VRB to VRB flow control, 111, 230 and 488 mOsmol/kg conditions, respectively. The color map scale is given at the side of the figure. On top of the figure the intervals $T_{17-20}$ and $T_{0-5}$ are labelled. These are used throught this chapter to sample populational speeds before and late after an osmotic shock. See for example Fig. 3.17.

It is unlikely that this is an effect of osmolality but is probably caused by an increased viscous drag on the polystyrene bead that is being driven by the motor. The weakest of the shock conditions, 111 mOsm/kg, includes a negligible relative viscosity increase of 1.056, but the 230 and 488 mOsm/kg conditions bring rises of 1.195 and 1.444, respectively. What is more likely due to high osmolality and the increased burden on the cell that it brings, is the time needed to recover the average value of motor speed after an osmotic shock. For the two smaller magnitudes, 111 and 130 mOsm/kg this takes $0.2 \pm 0.1$ and $0.7 \pm 0.3$ minutes on average. For the 488 mOsm/kg subset the mean recovery time is $5.2 \pm 0.5$ minutes, almost an order of magnitude slower than for the preceding, 230 mOsm/kg, condition for just twice the difference in relative viscosity. Recovery time data is plotted on Figure 3.18 A.

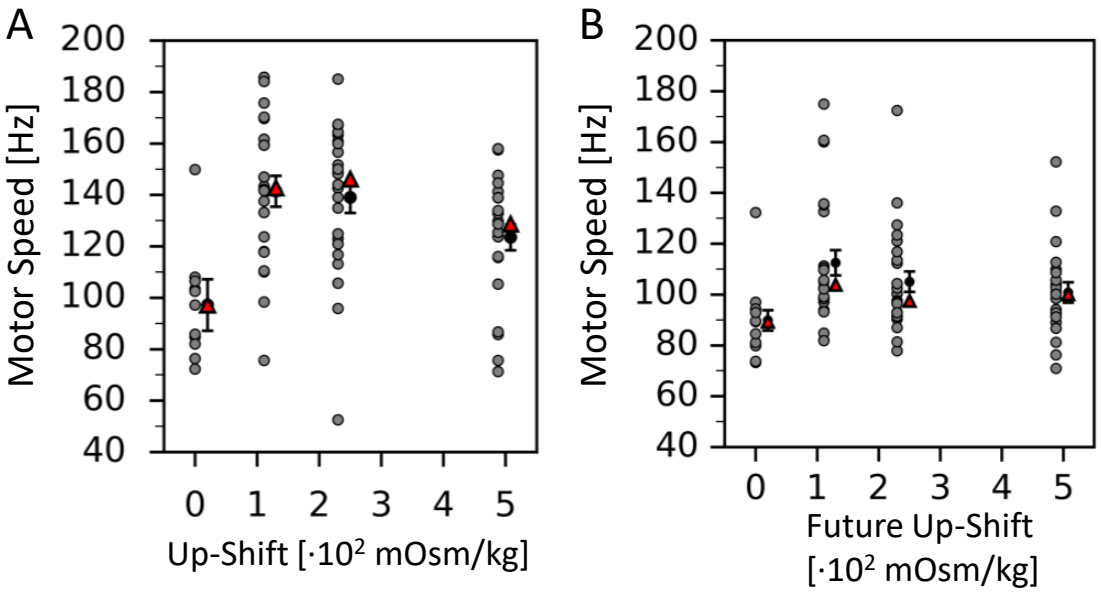


FIGURE 3.17: Average motor speeds for cells presented in Figure 3.16, sampled late after an osmotic shock, at $T_{17-20}$, and before the osmotic shock, at $T_{0-5}$. The former sampling is presented on panel A and the latter on Panel B. The circles are single motor values, triangles are medians and the black circle is the mean, together with its standard error. In panel A, the means are: $97 \pm 6$, $141 \pm 6$, $138 \pm 6$ and $124 \pm 6$, in order of acsending osmotic upshift. In panel B, the respective means are: $90 \pm 4$, $113 \pm 5$, $105 \pm 4$ and $100 \pm 4$.

**A population of swimming cells confirms single motor data**

To complement the measurements done on single motors, together with Vincent Martinez, I performed measurements of free swimming cells using Differential Dynamic Microscopy (DDM), a high throughput technique for measuring the swimming speed distribution in populations of self propelled particles, in our case *Escherichia Coli*. Measurements were performed using the MG 1655 strain, grown and washed into VRB as described in 2.5. Immediately before imaging, an osmotic shock was performed by mixing cells suspended in VRB with an aliquot of VRB containing the appropriate amount of sucrose, in a microfuge tube. Subsequently, cells were quickly placed into a capillary for DDM measurements and the capillary was sealed, resulting in a fixed amount of oxygen present during the experiment. Swimming speed recordings commenced within 2 min after the upshock and are shown in Figure 3.18 B. The gradual decrease of swimming speed with time observed in Figure 3.18 B for all magnitudes of osmotic upshocks is expected and was previously observed in a potassium phosphate buffer (Schwarz-Linek et al., 2016) where *Escherichia Coli* maintains PMF using only its endogenous energy sources (Dawes et al., 1965; Schwarz-Linek et al., 2016). The crash in swimming speed for the highest value of osmotic upshift, 785 mOsm/kg, looks like the crashes previously observed when cells run out of oxygen (Schwarz-Linek et al., 2016). This is indicative of a higher oxygen consumption rate at higher osmolalities as all samples start with the same concentration of cells and oxygen, and VRB does not support growth.

Consistent with what has been observed with BFM speed measurements, cells swimming at higher osmolalities reach higher motor speeds than cells swimming in VRB. Additionally, the within the first $\sim 50$ minutes, in the regime of osmotic upshifts between 0 and 215 mOsm/Kg, the peak post osmotic shock swimming speed is higher with increasing osmolality, while the 473 mOsm/kg condition struggles and does not reach a higher peak speed. This is in agreement with the relative changes presented in Figure 3.17 and Figure 3.16. At a later point in the measurement, the 473 mOsm/kg trace catches up and overtakes it's lower osmolality counterparts. If the aforementioned crash in speed of the highest shock condition is indeed due to increased oxygen consumption, it could be that it is this heightened oxygen consumption permits the 473 mOsmol/kg condition to maintain its speed for long enough to rise above the

lower shock traces.

Another point concerns the effect of flow. Pipetting a pre-shocked, free swimming cell suspension into a capillary for DDM is different to the exchange of media that happens in the bead assay. In the latter, the cells are attached to a surface and the flow running past exerts a force on the bead that is being driven by the BFM. There, the motor experiences more dramatic forces than in the case of a free swimmer suspension being pulled into a capillary. And, indeed, the data shows little difference between the speed traces for VRB and VRB + 21 mOsm/kg sucrose compared to an upshift of +116 mOsm/kg (Figure 3.20 A). This, taken together with the scaling of the effect with osmolality, presented in Figure 3.18 B, is strong evidence for a distinct effect stemming from a change in extracellular solute concentration.

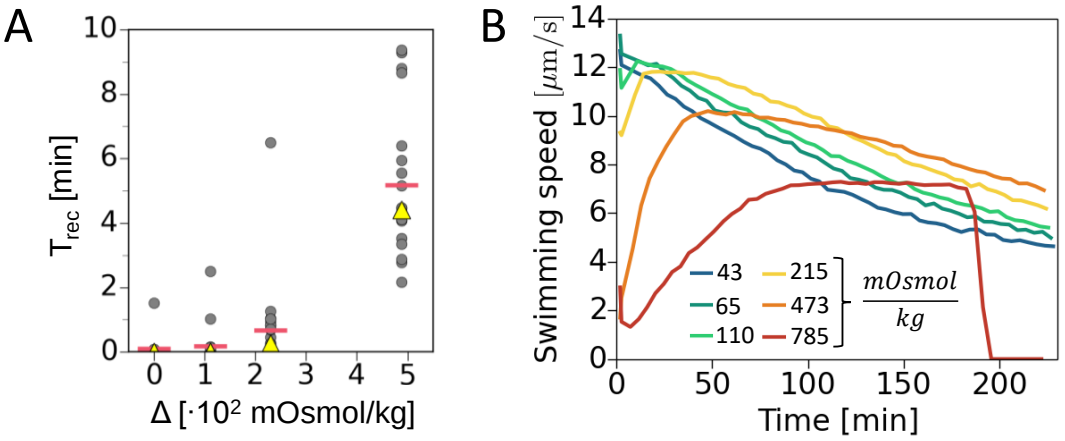


FIGURE 3.18: (A) Time necessary to recover the average value of pre-shock speed. Red horizontal bars are mean, and yellow triangles are median values, and the graph contains 18, 22, 23 and 20 single motor data points for the 0, 111, 230 and 488 mOsmol/kg upshocks. One value for the 230 mOsmol/kg condition and three for the 488 mOsmol/kg have been excluded from the graph as these motors do not recover average initial speed in the course of recording. The 0 mOsmol/kg condition is a buffer to buffer control flush.(B)DDM measurement of swimming speeds following an osmotic shock. Cells were shocked in microfuge tubes and brought into a microscope within 2 minutes. The legend shows shock magnitudes and the mean speed is the average of swimming speeds obtained for each time point in a range of different length scales (*Methods*). The systematic error of our measurements is then calculated as the standard deviation of the mean, and falls within $\sim$ 5% of the mean value. Here it was not plotted for clarity.

### 3.2.3 Motor speed changes are reversible

The result that cells swim faster at elevated osmolalities lead me to the question of whether speed changes could drive taxis. In a simple thought experiment, one could imagine two regions of space, one with low and one with high osmolality. If speeds were higher in the latter region, cells performing a random walk would spread out of it quicker, while the lower speed region would act as a sink of sorts, entrapping the cells. The first test of validity of such an idea was verifying that the change in speed brought by going from low to high osmolality is reversible once the swimmer is back at low osmolality. Otherwise, the speed would not be uniquely defined by the external solute concentration. Figure 3.19 features the motor speed distribution in VRB (from Figure 3.14), the speeds of 45 cells exposed to an osmotic upshift of 111 mOsm/kg and, ultimately, the speeds 27 of cells which have been shifted up to 111 mOsm/kg during early sample preparation and brought back to VRB in the final step, before measurement. The mean speed, expectedly, increases from $116 \pm 2$Hz to $156 \pm 5$ between VRB and +111 mOsm/kg and then decreases to $97 \pm 2$Hz for the cells that have been washed back into VRB. The origin of the relative undershoot of the “Back to VRB" with regards to steady state VRB speed is unknown. One possible reason could be depletion of endogenous energy sources during the 30 minute (sample preparation) period they spent at, presumably, higher metabolic rates in the +111 mOsm/kg condition. However, this shows that cells are able to reduce their motor speed upon being returned back to a lower osmolality.

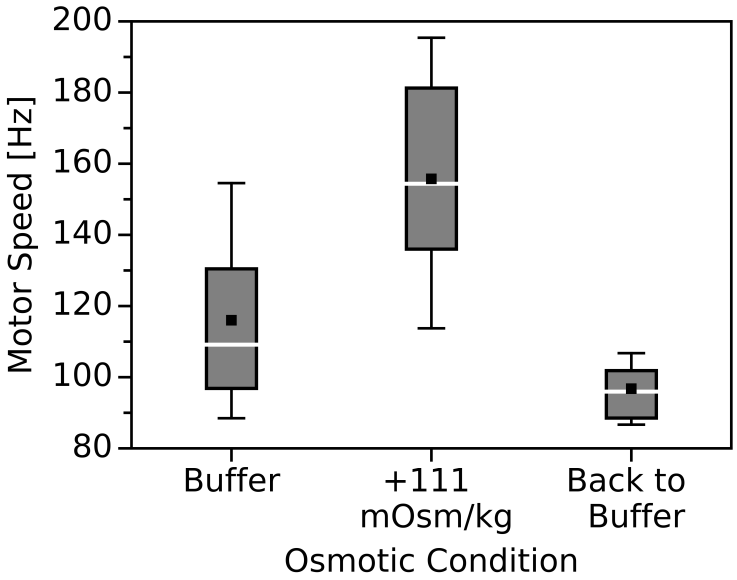


FIGURE 3.19: Cells that have been washed back into VRB from VRB+111mOsm/kg have similar speed levels to the pre-shock VRB condition. Speeds are given as box plots with the box denoting he interquartile range and the whiskers the 10th and the 90th percentile. The Buffer (VRB) box contains the entire VRB speed distribution already shown in Figure 3.14. The 111 mOsm/kg box contains speeds from osmotic upshift measurements 12 or more minutes after shock from Figure 3.16 and the $t \in [0, 5]$ interval of two-step dataset of Figure 3.8. The "Back to Buffer" box contains measurements performed in tunnel slides where cells were first brought to 111 mOsm/kg in a tube and then washed into VRB during the final wash step of tunnel slide preparation. The boxes contain 118, 45 and 27 cells, with population average speeds of $116 \pm 2$Hz, $156 \pm 5$ and $97 \pm 2$Hz.

### 3.2.4 Changing osmolality in one or ten steps has the same effect

Another check of whether the speed is defined by the osmolality, and independant of the path taken to reach it, is elevating the osmolality in multiple steps. This was done in the DDM experiment, with an osmotic upshift of 235 mOsm/kg in magnitude. In one sample, the cell suspension in VRB was mixed with an appropriate amount of VRB + Sucrose to achieve an instant change of 235 mOsm/kg. In the second sample, the elevation of osmolality was done in 10 steps, over two minutes, producing increments ranging from 50 mOsm/kg in the first step to 11 mOsm/kg in the last (inset of Fig. 3.20 B).
According to the data in Figure 3.20 A, an increase of +21 mOsm/kg in VRB produces very little change in swimming speed, while that of +100 mOsm/kg brings approximately a 15 % increase. From Figure 3.18 B we can infer that a change in osmolality of 65 mOsm/kg will definitely bring visible speed changes. Combining the two separate DDM measurements, it is clear that cells started reacting to osmotic changes somewhere in the range between $\sim$ 20 and $\sim$ 60 mOsm/kg. Hence, this incremental approach occurred in a sequence of temporally spread steps close to the minimum response threshold, in stark contrast with the one single step.
Remarkably, the speed traces for both ways of increasing osmolality show minimal differences and are presented in Figure 3.20 B.

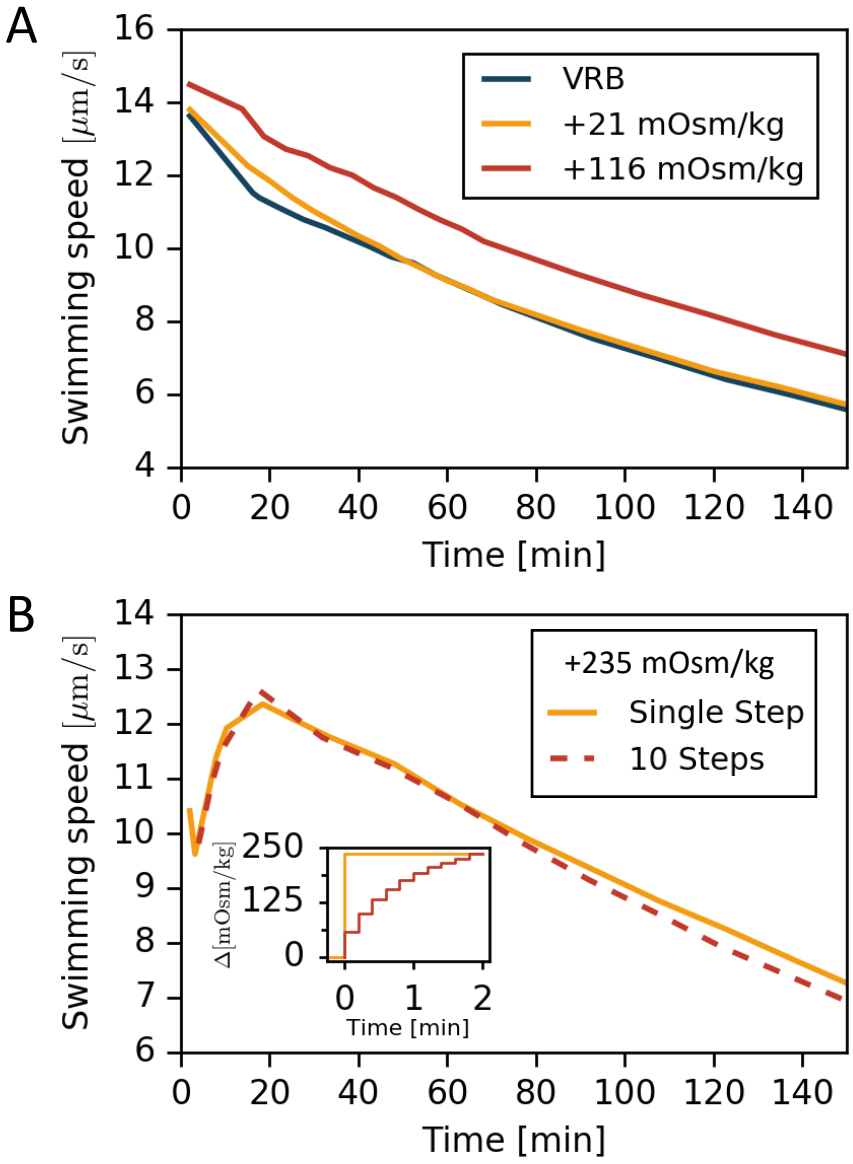


FIGURE 3.20: A: DDM measurement of swimming speed in VRB (blue), VRB + 21 mOsm/kg (orange) and VRB + 116 mOsm/kg (red). B: Elevating the osmolality in two different ways. A single step bringing the cells up to VRB + 235 mOsm/kg (orange), and the same shock magnitude but performed in 10 steps (red, dashed). The inset shows the calculated changes in osmolality over time with the two methods.

### 3.2.5 Speed recovery after the 488 mOsm/kg shock does not show clear steps

Following an osmotic shock of 488 mOsm/kg in magnitude, motor speed drops to zero and immediately begins a recovery. Whether this recovery shows a smooth or steppy variation of speed provides insight into the mechanism through which the motor recovers. For example, the presence of clear steps would indicate re-integration of stator units, like in ressurection experiments (Yuan et al., 2008; Reid et al., 2006; Ryu et al., 2000; Lele et al., 2013). I have not observed a consistent presence of steps, but rather a significant portion of traces with a smooth speed recovery. The results are presented in Figure 3.21.

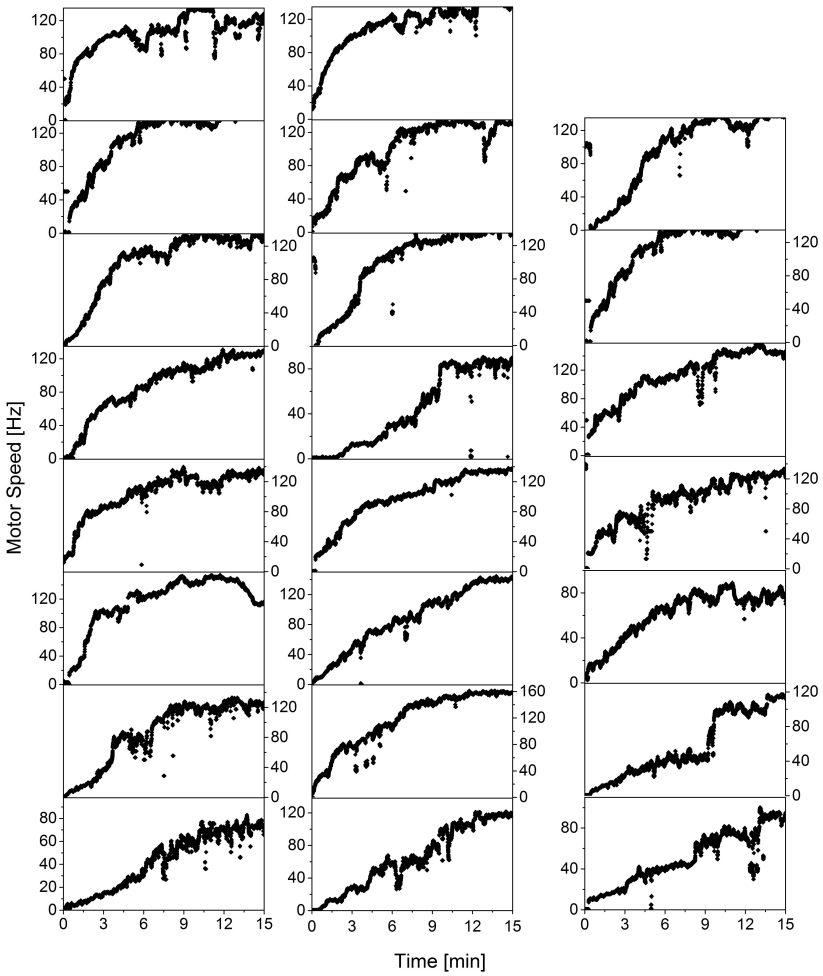


FIGURE 3.21: Plots of 15 minute post shock segments of all of the single motor traces from the 488 mOsm/kg sucrose shock condition, showing no clear presence of steps in the post-shock recovery of motor speed.

### 3.2.6 Single motors seem to have near maximum stator number before and after shock

Here I present a preliminary analysis of stator steps in the rotation of the BFM in two osmotic conditions, VRB and VRB + 488 mOsm/kg. In the first, 44 clear steps were identified and characterized in samples of rotation coming from 34 individual single motor, single cell traces. In the second, high osmolality, condition 19 steps were counted from 5 different cells. Examples of steps used in the analysis are given in Figure 3.22 A. All of the step sizes are plotted in Figure 3.22 B, with the VRB points given in black and the +488 mOsm/kg ones in red. Those marked by an asterisk have been subsequently determined to be two-stator steps by finding a small intermediate steps or comparing with several other steps in the same speed trace. Thus, I introduced a threshold line below the smallest determined double step, at 19Hz. The single step mean value for VRB is $12.2 \pm 0.4$Hz and for VRB + 488 mOsm/kg $11.5 \pm 0.9$Hz. Applying the viscosity correction to the latter yields $16.4 \pm 1.3$Hz, indicative of a higher relative motor torque. The average, uncorrected, initial motor speeds in these conditions are $113 \pm 4$Hz and $124 \pm 4$Hz.

In Figure 3.22 C, I divide the step size with the value of the motor speed before the step. For the points corresponding to those from panel B that are below the 19 Hz threshold, the average relative single step for VRB is $11.2 \pm 0.6\%$ and for the VRB + 488 mOsm/kg condition it is $10 \pm 1\%$. Assuming that the stator step size is the same regardless the step number, as suggested by (Ryu et al., 2000), these percentages indicate that there are between 9 and 11 stators associated with the motors in both conditions.

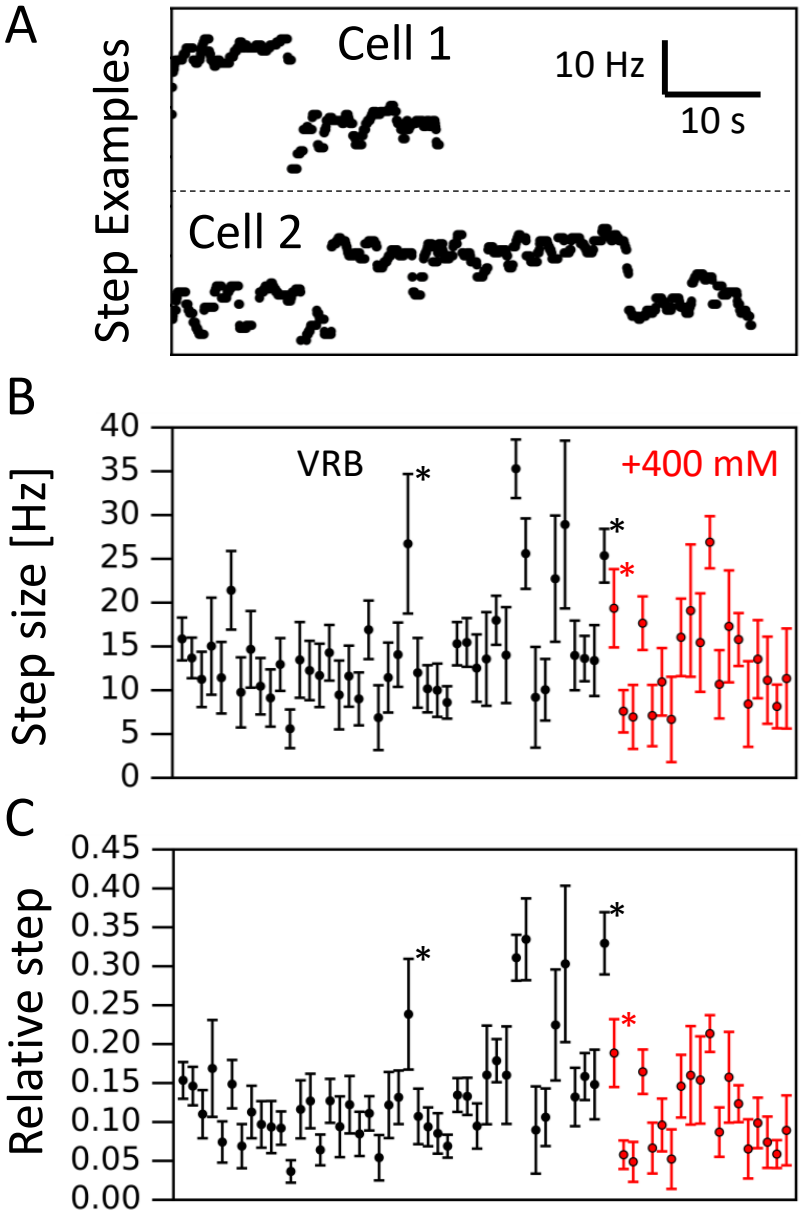


FIGURE 3.22: A: Examples of steps in motor rotation that are attributable to changes in stator number. Samples of motor rotation from two cells in VRB are given. B: Step sizes for a sample of 44 steps taken from 34 single motor traces (from individual cells) in VRB are given in black. In red - 19 steps extracted from post osmotic shock motor rotation samples of 5 cells. C: Values from (B) divided by the initial speed. Error bars represent the sum of the standard deviations of motor speeds before and after step. Standard errors are at least 20-30 times smaller due to the number of points used to calculate the means. Points marked with an asterisk have been determined to be double steps based on a short intermediate step or other steps present in the trace.

### 3.2.7 Correlations between CCW and CW speed, and CCW Speed and CW Bias

The wide range of speeds, obtained through use of different beads, buffers and osmolalities was used in Figure 3.23 to reproduce the result of Berg (ref ref) concerning asymmetry in the rotation of the flagellar motor. In good agreement, my data has reproduced the departure from symmetric CCW-CW speeds around $\sim 75\text{Hz}$. Additionally, the figure inset addresses the question of whether the CW Bias and motor speed are correlated in my experimental conditions and no evidence of correlation is found.

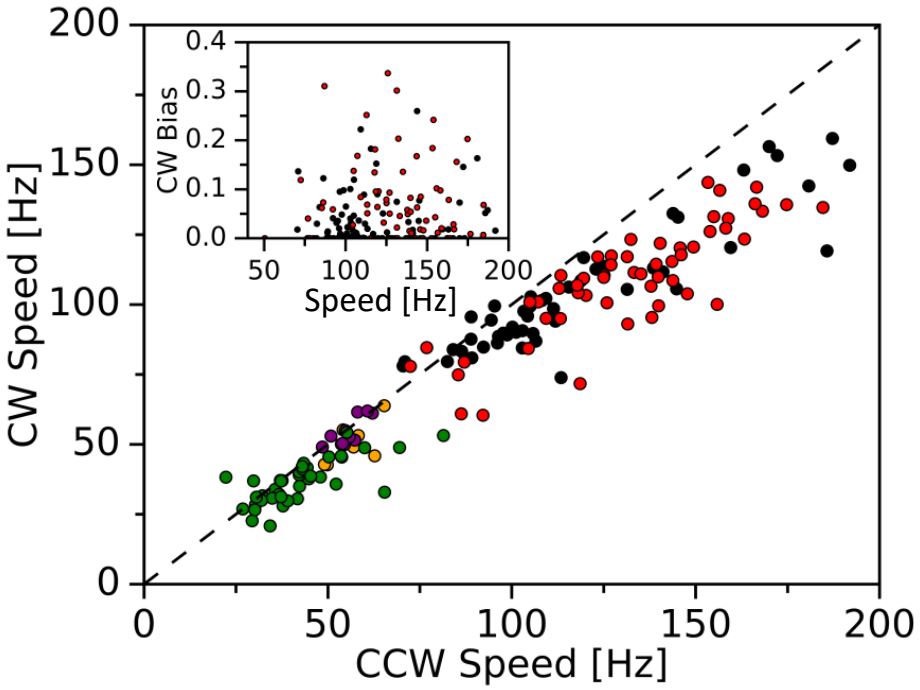


FIGURE 3.23: Clockwise speed plotted versus counter-clockwise speed. Green, putple and orange points are single motor data for TB, MB1 and NMB, respectively, using $1\mu\text{m}$ beads. Black circles represent VRB data acquired with $0.5\mu\text{m}$ beads before an osmotic shock, and red points represent the same set of motors 14.5 minutes after an osmotic upshift. Here, upshift magnitudes of 111, 230 and 488 mOsm/kg are all gruped together. All speeds were sampled for one minute. The inset shows CW Bias versus CCW Speed, with VRB points in black and shock dataset points in red, using the same 1 minute samples from the main figure.

### 3.2.8 Extending the measurements to NaCl

Lastly in this section, I present the extension of the measurements to another solute, NaCl. Figure 3.24 is a speed color map, constructed in the same manner as Figure 3.16. In the first condition, eight motors on individual cells were measured before and after an osmotic shock of 93 mOsm/kg in magnitude, administered by exchanging VRB for VRB + 50 mM NaCl. The second condition contains seven motors, with the osmotic shock magnitude of 187 mOsm/kg, corresponding to a concentration upshift of 100 mM NaCl. Similarly to the osmotic shocks with sucrose (Fig. 3.16), there is an increase in speed, albeit seemingly of a shorter duration. Some cells in the second condition appear not to respond, or respond with a slowdown. Curiously, those cells (4 out of total of 7) have pre-shock motor speeds over 139 Hz, well above the VRB average of $107 Hz$ (Fig. 3.14). Initial motor speeds for each cell are indicated on the side of the figure.

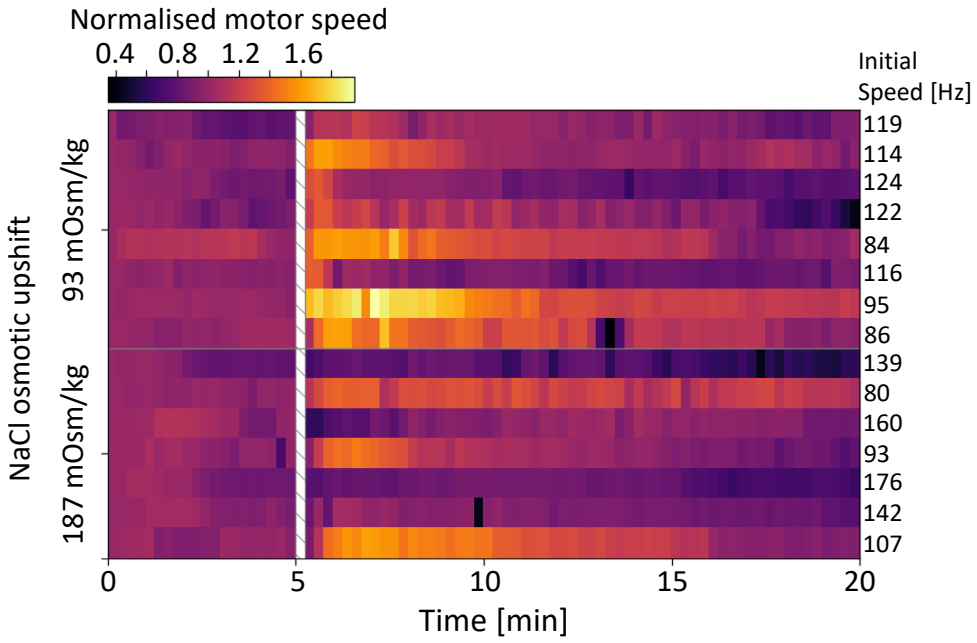


FIGURE 3.24: Stacked single motor, single cell speed histograms, constructed in the same way as for Fig. 3.16. Bins are of 15s in width and speeds have been normalised to the value of the first bin. Two osmotic upshift conditions are assayed, 93 and 187 mOsm/kg, as indicated on the left hand edge. The first condition contains 8 recordings, while the second comprises of 7. On the right hand side, the initial (first bin) motor speeds are listed.The white hatched column at t=5 minutes represents the point of osmotic shock, administered by flowing in new buffer with added NaCl.

## 3.3 Short term effects of flow on motor speed and bias

Here I further explore the relationship between flow and motor speed that was hinted in Figures 3.15 A and 3.16. Flowing in the same buffer gives a response, similar but smaller in magnitude, to that of elevating the osmolality. Figure 3.6 A hints at a possible subtle effect on CW bias with the drop near t=5 minutes when the buffer exchange happens. Investigating the effect of flow, I have performed measurements using the bead assay in a flow cell, described in Section 2.5 which allows precise control of the average flow rate through the channel using a syringe pump. Flow pulses were of 10 seconds in duration, similar to the length of media exchange in the osmotic shock experiments. The flow rates examined, ranging from 50 to 750 $\mu$l/min were chosen to that they are similar or greater than the average rate in osmotic shock experiments ( $\sim 120\mu l/min$).

### 3.3.1 Flow has little effect on CW Bias

I examined the effect of flow on CW Bias by flowing in several buffers. Representative traces from data sets produced using one- or half micron diameter beads are presented in Figures 3.25 and 3.26. The widest range of scanned conditions, employs MB1 as the buffer of choice and Fig. 3.26 shows examples of measurements with one micron beads, under flows of 50 and 750 $\mu$l/min and Fig. 3.25 exemplifies those for 100 and 300 $\mu$l/min. These show no striking and immediately evident effect on CW Bias. Other condition studied, and presented in these figures include NMB (100 $\mu$l/min, 1 $\mu$m beads), TB (300 $\mu$l/min, 1 $\mu$m beads), MB1 (750 $\mu$l/min, 0.5 $\mu$m beads) and manual flush controls from the osmotic shock experiments done with 0.5 $\mu$m beads.
Further, I have calculated CW Bias traces for all of these conditions and plotted them in Figure 3.27 and Figure 3.28 A, showing individual traces and a black median line. Manual VRB flush controls are already shown in Figure 3.6 A, with the mean, median and the interquartile range. Two smallest flow rates delivered with MB1, $50\mu$l/min and $100\mu$l/min (Fig. 3.27 B,E) do feature a drop in median CW Bias following the administration of flow. Going higher in flow rate with MB1, as shown in Figure 3.27 D and F, the drop is no longer visible.

Thus, no general conclusion can be made about a potential effect of media exchange on CW Bias. Here I disregarded the panels A and C of Figure 3.27 and Fig. 3.28 A due to these having only 7, 4 and 4 individual measurements.

### 3.3.2 The effect on motor speed depends on bead size

While there appears to be no conclusive effect of flow on motor bias, Figure 3.26 E-H indicates that when the bead diameter is reduced from 1 micron to 0.5 micron, an effect on speed begins to show. To look for signs of this effect I compare the average speed of a 3 minute interval just before flow to the average speed of such an interval immediately post flow. This way I look for speed changes on time scales spanning several minutes, like those observed previously in Figure 3.16 in the flush control portion of the dataset. Figure 3.29 details the pre- and post-flow speeds for all of the 1 micron bead conditions exemplified in Figures 3.25 and 3.26, clearly showing that there is no tangible speed rise.
However, as seen in Figure 3.26 E-F, 0.5 micrometer beads, when subject to flow of 750 $\mu\mathrm{l/min}$ get a short lived rise in speed, although too short to manifest itself well in a 3 minute average in Figure 3.28 B. To better characterise the initial minutes post flow, I extended the data set where the effect is most pronounced, the $0.5\mu\mathrm{m}$ bead flush controls. Eleven of these are have been already presented in Figure 3.16, in duration of 20 minutes, and I collected 6 more single motor recordings of 10 minute duration. They have been put together in 3.30, plotting the interquartile range in grey and the mean line in red. The inset plots the 3 minute average speeds before and just after shock, revealing a strong effect in this condition.

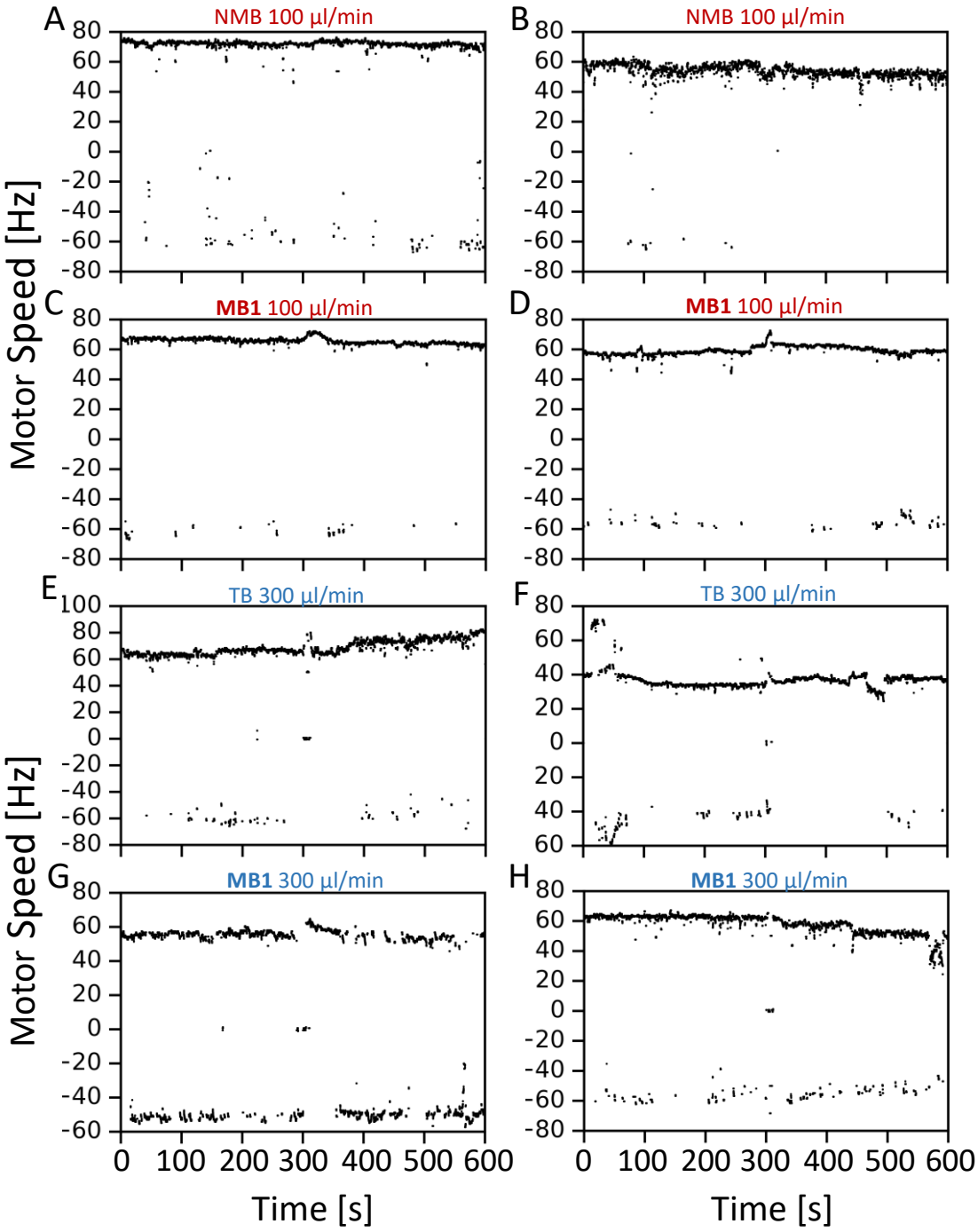


FIGURE 3.25: Example traces of motor rotation from flow experiments using 1 $\mu$m beads. A 10 second pulse of flow is administered at t=300s. A,B: Experiments carried out in NMB with a flow rate of 100 $\mu$l/min, with respect to the entire cross section of flow cell channel. C,D: Same as A and B, but the buffer is MB1. E,F: Tryptone Broth with a flow rae of 300 $\mu$l/min. G,H: MB1 with a flow rate of 300 $\mu$l/min.

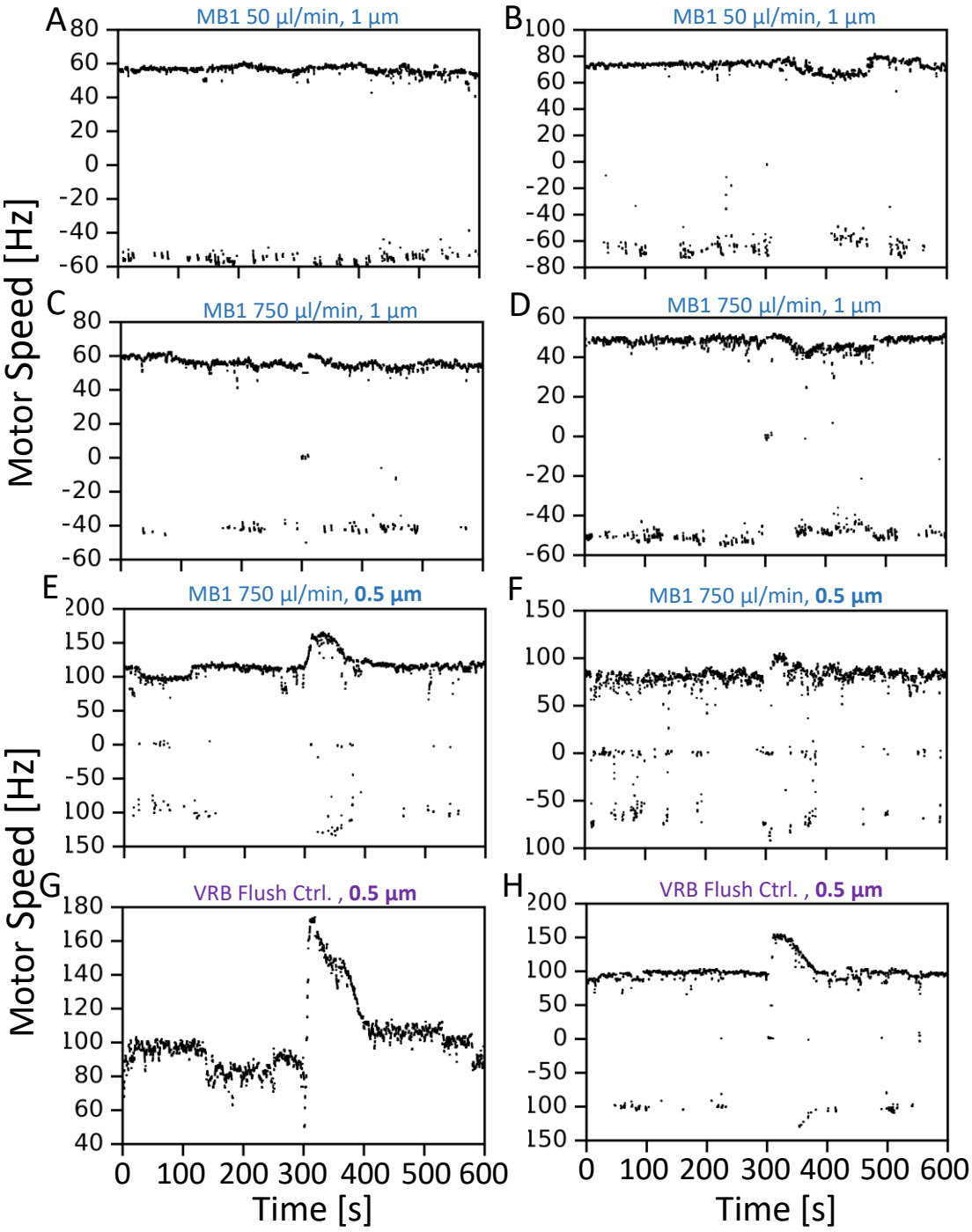


FIGURE 3.26: Example traces of motor rotation from flow experiments using 1 $\mu$m (A,B,C,D) and $0.5\mu$m (E,F,G,H) beads. A 10 second pulse of flow is administered at t=300s. A,B: Experiments carried out in MB1 with a flow rate of 50 $\mu$l/min, with respect to the entire cross section of flow cell channel. C,D: MB1 with a flow rate of 750 $\mu$l/min. E,F: Using $0.5\mu$m beads with a flow rate of 750 $\mu$l/min of MB1. G,H: Experiments performed in a tunnel slide, in VRB, flushing through 24 $\mu$l of VRB at t=300 over a time span of 10-15 seconds, with a $\sim 5-7\mu$l channel volume.

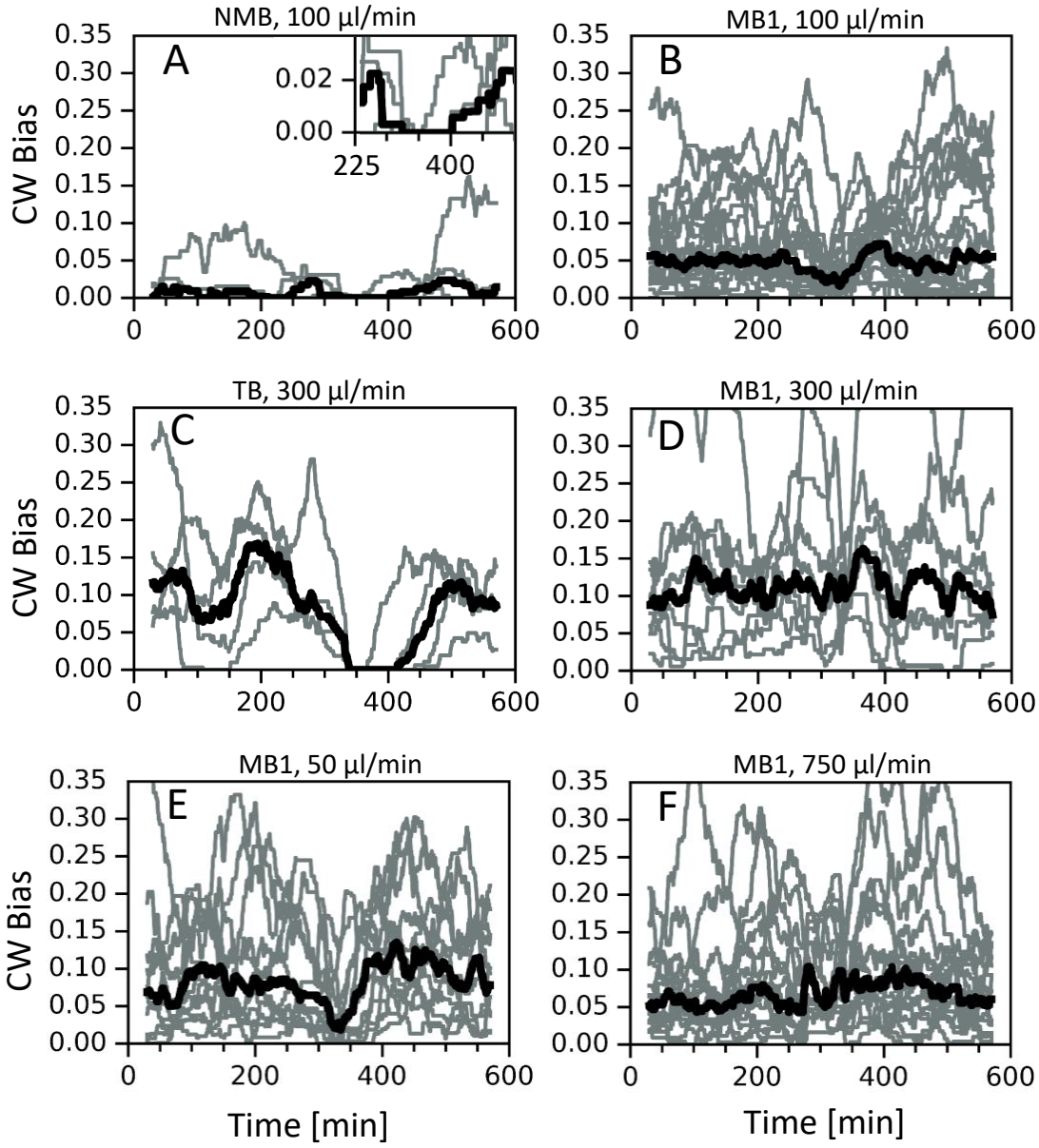


FIGURE 3.27: Traces of motor CW Bias calculated from speeds including those presented in Figures 3.25 and 3.26. A moving window of 60 seconds in width was used to calculate the CW Bias. Grey lines are single motor traces and the black line represents the median. A: 7 motors for the NMB $100\mu\mathrm{l/min}$ condition. B: 20 motors for the MB1 $100\mu\mathrm{l/min}$ condition. C: 4 motors for the $300\mu\mathrm{l/min}$, in TB. D: 8 motors for the $300\mu\mathrm{l/min}$, in MB1. E: 12 motors in MB1 with a flow rate of $50\mu\mathrm{l/min}$ and F: 17 motors in MB1 with a flow rate of $750\mu\mathrm{l/min}$

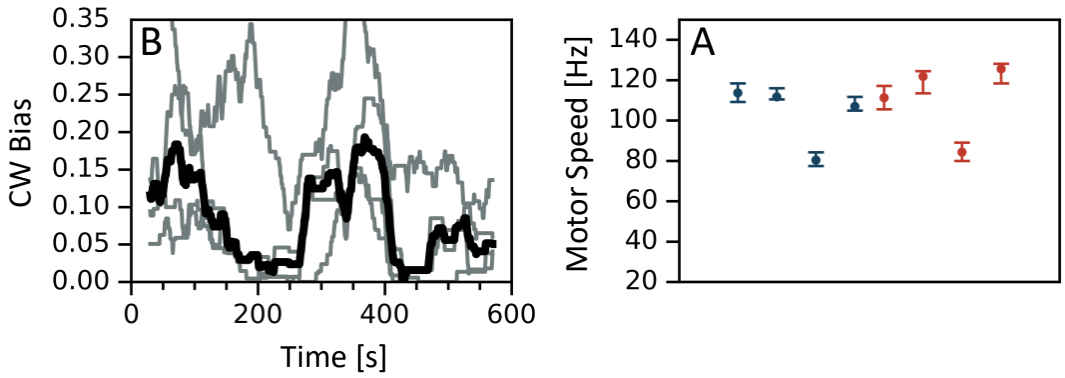


FIGURE 3.28: A: 4 single cell, single motor traces of CW Bias calculated on a 60s wide moving window for the $750\mu\mathrm{l/min}$ flow condition using $0.5\mu\mathrm{m}$ beads. The black line is the median and flow was administered at t=300s for 10s. B: Average motor speeds 3 minutes before flow (blue) and 3 minutes after flow (red). Error bars are the interquartile range.

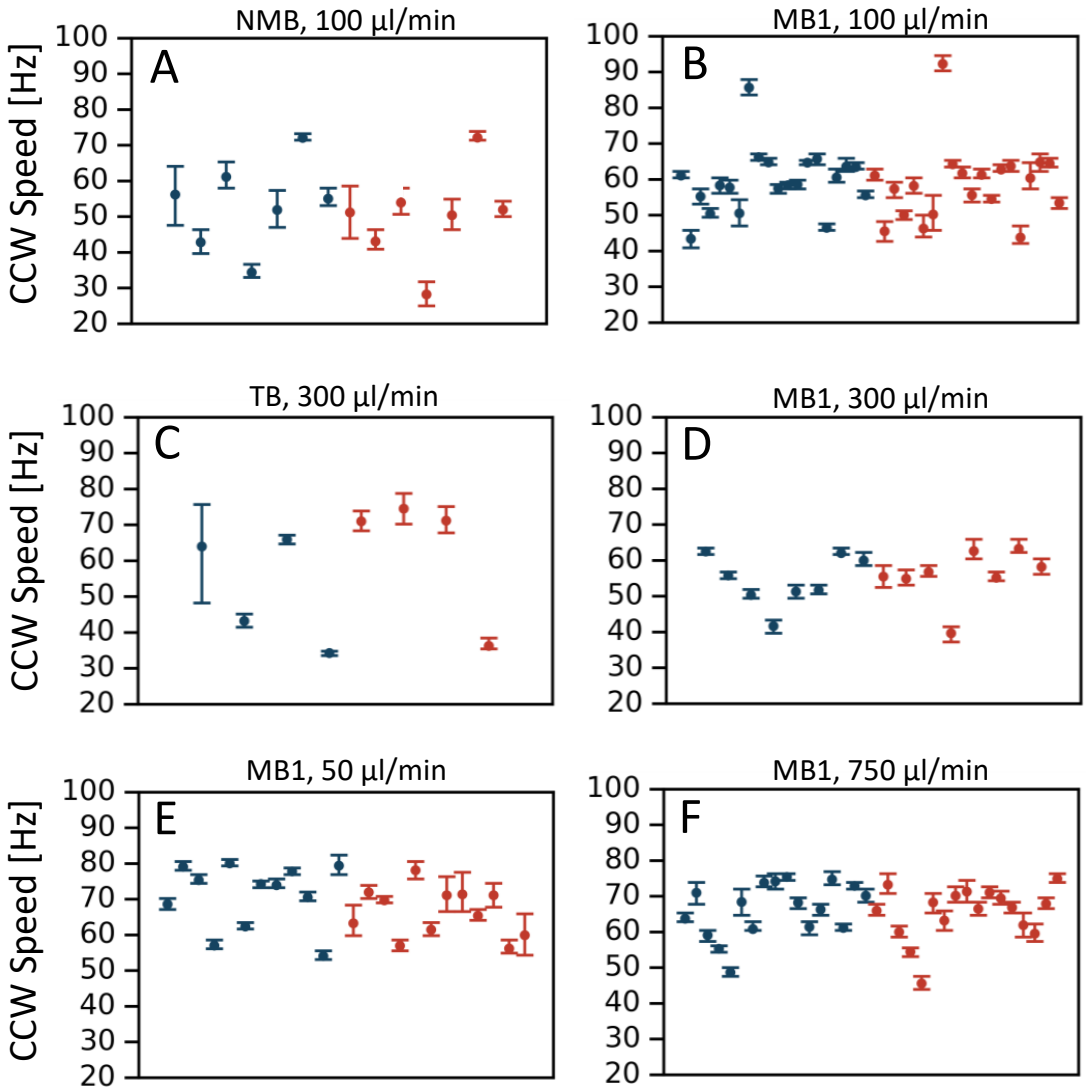


FIGURE 3.29: Average CCW Speed before and after flow. The sampling interval is 3 minutes long. The error bars represent the interquartile range of the sampling interval. $1\mu$m beads were used for all measurements. A: 7 motors for the NMB $100\mu$l/min condition. B: 20 motors for the MB1 $100\mu$l/min condition. C: 4 motors for the $300\mu$l/min, in TB. D: 8 motors for the $300\mu$l/min, in MB1. E: 12 motors in MB1 with a flow rate of $50\mu$l/min and F: 17 motors in MB1 with a flow rate of $750\mu$l/min

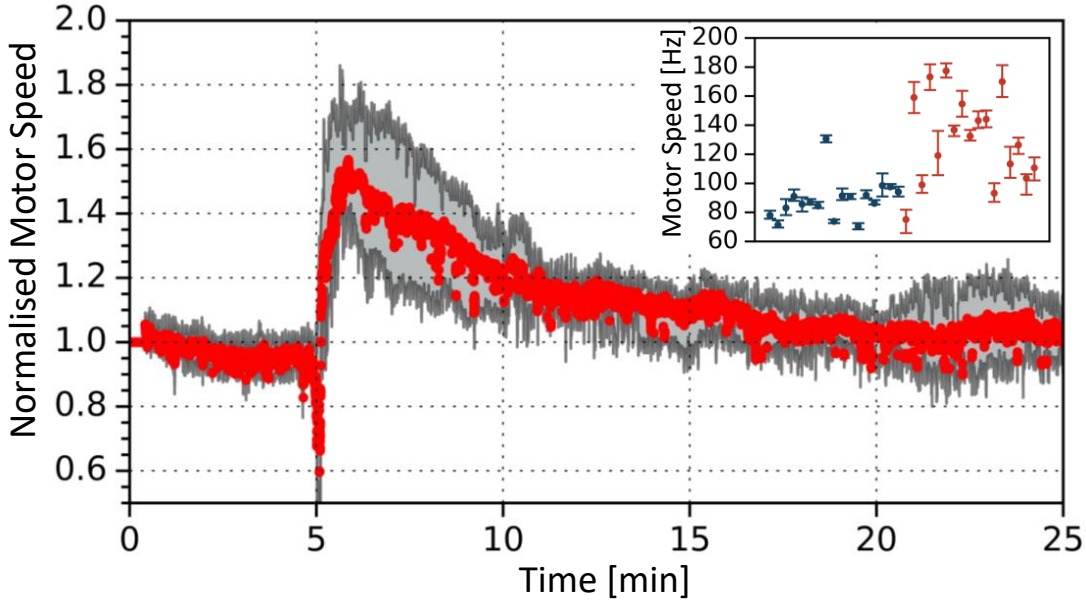


FIGURE 3.30: Eleven 22-25 minute long and six 10-15 minute long single motor rotation traces have been plotted as a mean speed value (red) and the interquartile range (grey). VRB was exchanged for VRB at t=5 minutes by flowing through 24 $\mu$l over 10-15 seconds by pipetting the liquid onto one end of a tunnel slide (Section 2.5) and withdrawing with a tissue paper on the other end

# Chapter 4

# Discussion

## 4.1 Results in context of previous work

Previous work has reported that cells show apparent tumble behaviour when exposed to sudden changes in osmolality, over 100 mOsmol/kg in magnitude (Li et al., 1988). This behaviour was divided into two regimes, for changes under 300 mOsmol/kg only tumbling was observed and for changes over 400 mOsmol/kg a several minutes long cessation of motion was followed by tumbling (Li et al., 1993). The combined effect of stopping and tumbling in the latter regime has been termed pseudotumbling and, surprisingly, it is characterized by CCW rotation of flagella, a behaviour that normally leads to stable bundle formation and smooth swimming (Adler et al., 1988). However, the authors report a range of KCl concentrations of 0.1-0.8M where they have seen tethered cells spin CCW. The lower bound of this range is within the first regime of "tumble" behaviour, indicating that probably in the small shock regime the observed tumbling too comes with CCW rotation of the flagella.
Thus, there is likely just one regime of response to sudden temporal changes in osmolality and the pause in rotation could just be some sort of a period through which a cell is "knocked out" by the large osmotic shock.
My data on the motor response to osmotic shocks supports this hypothesis. In the range of upshifts between 100 mOsmol/kg to 500 mOsmol/kg, covering both the low and high shock regimes postulated above, I have noticed a single regime of CW Bias response. It proceeds in two phases, Phase I and Phase II, durations of which scale with shock magnitude (Fig. 3.5). In the first phase, switching is supressed and the motor rotates exclusively CCW. Whether flagella can form bundles and run during this time is unknown, but likely it is during this phase that Adler (Adler et al., 1988) looked at tethered cells and

noticed them rotating CCW. Phase I length scales with osmolality (Fig. 3.7 B) and its duration for the highest shock magnitude is 5-6 minutes. There, a change of 488 mOsm/kg was delivered with an increase in sucrose concentration of 400 mM. On a similar time scale, *E. coli* cells that underwent an upshift in external osmolality of $\sim$ 400 mOsm/kg, also delivered using sucrose, recover the bulk of their volume (Pilizota et al., 2012). A possible correlation of the end of Phase I and the recovery of cell volume would support the idea that CCW rotation of flagella during pseudotumbling arises due to membrane deformations interfering with the flagellar motor, somehow preventing the filaments from bundling up despite spinning CCW, as discussed by Li (Li et al., 1993). In addition, the concentration dependence of Phase I (Fig. 3.7 B) tells us that it could be negligibly small when the changes in concentration are small or slow enough. That could explain why despite pseudotumbling, the non chemotactic mutants were still unable to perform taxis in spatial assays, pointing that Phase I/pseudotumbling is probably not a useful response but likely an intermediate behaviour that is a consequence of pathological changes in the membrane structure and that goes away as soon as the cell repressurises itself. I also noticed stopping and a slow speed recovery with my highest shock, 488 mOsm/kg. Together with CCW rotation of Phase I, these observations are fully consistent with what was seen before for osmotic upshifts of this magnitude. The origins of the speed drop are discussed more in Section 4.2. The lowest, 111 mOsmol/kg shock presents no speed drop, the 230 mOsmol/kg shows a small and, at best, very short reduction in speed, and the 488 mOsmol/kg a large drop and a longer lasting slowdown. This scaling is evident from Figure 3.18 A, which shows the time it takes for motors to regain their initial average speed after shock. The drop in speed is connected to the strength of the osmotic upshift, probably varying continuously with magnitudes and is not a binary two regime response of ''no effect" or ''complete stop" put forward previously (Li et al., 1993), which was limited by the metods the respective authors had at their disposal. Namely, the microscopic observations and observations of tethered cells were carried out by visual inspection without capacity for temporal resolution or ability to say whether the free swimming cells are tumbling due to CW or CCW rotation of flagella, as the authors themselves noted.

## 4.2 Origins of speed changes

### 4.2.1 Summary of findings

Motor speed measurements have shown a consistent trend of long term speed increases following osmotic shocks (Fig. 3.15, 3.16). With step upshifts in osmolality, different strengths lead to different time scales in the response. Figure 3.16, a heatmap presenting an overview of the entire sucrose dataset summarizes these temporal dynamics. In brief, the peak speeds occur sooner for weaker shocks. Strong shocks, like 488 mOsmol/kg, first cause a drop to zero speed and then gradually recover to elevated speed levels. Lastly, after the peak speed is attained, the speed levels slowly decrease, possibly because of oxygen limitations (Schwarz-Linek et al., 2016) in the sealed tunnel slide or due to depletion of endogenous energy sources (Dawes et al., 1965). The delay in achieving peak speed could also be related to energy burdens put on the cell by having to cope with volume changes (Pilizota et al., 2012) through pumping and synthesising osmolytes (Perroud et al., 1985; Wood, 1999).
I take the interval denoted $T_{17-20}$ (Fig. 3.16) as a point of comparison of long term effects in different osmotic conditions. $T_{17-20}$ is the section between the 12th and the 15th minute post shock. All of the conditions show increased speed levels in $T_{17-20}$ compared to the buffer to buffer control. The increase is the biggest in the 111 mOsm/kg condition, but this is likely due to increased viscosities slowing down the motor at higher osmolalities. While the 111 mOsm/kg increase comes with a small rise in viscosity compared to VRB, by a factor 1.06, the following two conditions come with more considerable changes, of 1.20 and 1.44 for the 230 and 488 mOsm/kg conditions, respectively. If the speeds are multiplied by the relative viscosity, we obtain a quantity proportional to motor torque, which shows a monotonous increase with final osmolality (Fig. 4.1 A). DDM Population swimming measurements are consistent with single motor data in the sense that the higher shocks eventually overtake their lower counterparts in terms of swimming speed (up to 473 mOsmol/kg) or torque output (up to 785 mOsmol/kg, Fig. 4.1 B). Additionally, at the highest shock, 785 mOsmol/kg, we observe a sudden crash in speed, consistent with previously observed crashes that happen upon depletion of oxygen in the measurement capillary (Schwarz-Linek et al., 2016).

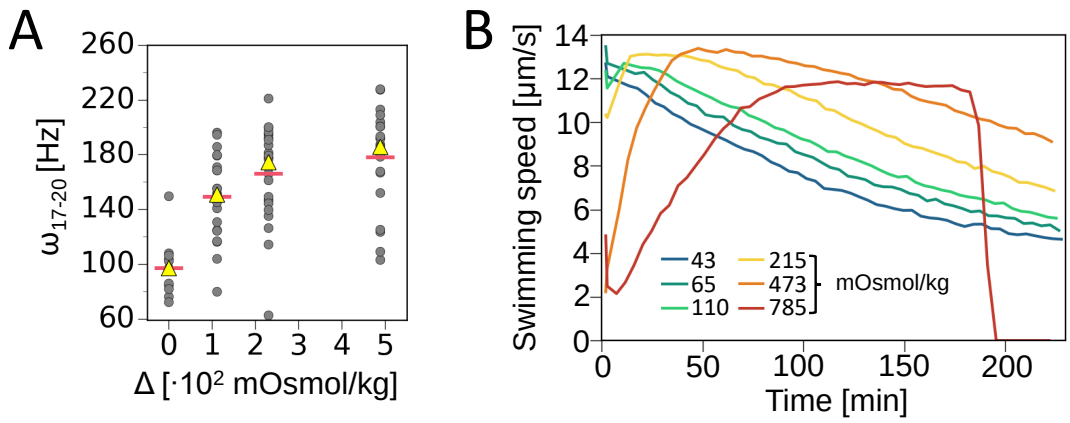


FIGURE 4.1: (A) Average motor speeds, multiplied by the relative viscosity (to VRB), for cells presented in Figure 3.16, sampled late after an osmotic shock, at $T_{17-20}$. The circles are single motor values, yellow triangles are medians and the red horizontal bar is the mean. The original, uncorrected figue is Fig. 3.17 A. (B) DDM measurement of swimming speeds following an osmotic shock, multiplied by the relative viscosity increase due to sucrose. Cells were shocked in microfuge tubes and brought into a microscope within 2 minutes. The legend shows shock magnitudes and the mean speed is the average of swimming speeds obtained for each time point in a range of different length scales (*Methods*). The systematic error of our measurements is then calculated as the standard deviation of the mean, and falls within $\sim$ 5% of the mean value. Here it was not plotted for clarity. The uncorrected version is presented in Figure 3.18 B.

### 4.2.2 High osmolality could increase PMF

The large long term increases in motor speed could be due to an increased PMF, possibly through changes in cell metabolism. An alternative explanation could be incorporation of additional stator units. The stator units have been shown to act as mechanosensors, with more units integrating into the BFM if the load increases, up to a maximum of 11-12 (Lele et al., 2013; Tipping et al., 2013a). Thus, an increased load due to the viscosity of sucrose could mechanically be stimulating the BFM and prompting it to integrate more force generators.

I have estimated the number of stator units per motor in VRB and in VRB + 488 mOsm/kg of sucrose. Upon the addition of that amount of sucrose, the viscosity changes by a factor of 1.44. This is the condition with the largest change and was picked for analysis expecting to give the largest difference in stator occupancy. However, in both cases there were 9-11 units present in the stator, thus operating close to the maximum capacity (Leake et al., 2006). Additionally, the

relative viscosities of the lowest (111 mOsm/kg) and largest (488 mOsm/kg) sucrose shock, 1.06 and 1.44, were used to find equivalent concentrations of Ficoll 400, a large mass, branched polysaccharide. Ficoll has previously been used in motor and swimming studies to elevate the viscous load without affecting the osmolality (Chen et al., 2000b; Martinez et al., 2014). According to the literature, the concentrations in question are 0.2% and 1.7% by weight, respectively (Chen et al., 2000b). Both single motor and swimming data show no increase of speed at these concentrations, with the higher one causing a slight reduction (Chen et al., 2000b; Martinez et al., 2014). This is another argument against the motor remodelling to increase the number of stator units in response to the elevated viscous load.
Support for the case of increased PMF comes from the larger torque per stator unit observed post osmotic shock, since torque is proportional to PMF (Fung et al., 1995). An increased metabolic rate, suggested by the early oxygen crash in the DDM experiment, could be responsible for the larger PMF. Another feature of the single motor traces that includes possible PMF dynamics is the speed recovery in the 488 mOsm/kg condition (Section 3.2.5). There, after the sudden drop to zero, the speed starts recovering without any consistent stepping. Stepping is what one would expect if disengaged stators were becoming reengaged with the motor (Ryu et al., 2000). Instead, the recovery is predominantly continuous and could result from a gradual recovery of PMF, as the two are proportional (Gabel et al., 2003; Lo et al., 2007).

## 4.3 Origins of osmotaxis

### 4.3.1 Speed driven bacterial accumulation

*E. coli* swims in an almost straight line and re-orients every so often in a nearly random fashion, performing a random walk that can be characterized with an effective diffusion constant $\mathrm{D} \sim \mathrm{v}^2/\alpha$ (Schnitzer et al., 1990; Schnitzer, 1993), where $\mathrm{v}$ is the swimming speed and $\alpha$ the tumbling rate given by

$$\alpha = \frac{3(1-\cos\phi_0)(\tau_{\mathrm{run}}+\tau_t)}{\tau_{\mathrm{run}}^2} \tag{4.1}$$

with $\tau_{run}$ being the mean run time, $\phi_0 \sim 71^\circ$ mean reorientation angle following a tumble, and $\tau_t$ the duration of the tumble event (Schnitzer, 1993; Lovely

et al., 1975). Chemotaxis is characterized by active sensing. The chemotactic network measures the concentration of a chemical in the environment and compares it to the value it had measured a second prior. Then it modulates $\alpha$ to retain or change the direction of swimming. Thus, $\alpha(\mathrm{x})$ will have different values depending on whether the cell is oriented towards or away from the source of a gradient.
In the case of CheRCheB mutants, defective in adaptation due to lack of methylation and demethylation enzymes, the external concentration of ligands defines the kinase activity and it does so reversibly (Segall et al., 1986). These cells are unable to perform temporal comparisons and are only able to output a tumble rate $\alpha(\mathrm{x})$ which depends only on the current concentration of, for example, a repellent. This has prompted theoretical studies of a spatially varying tumble rate $\alpha(\mathrm{x})$ and swimming speed $\mathrm{v}(\mathrm{x})$ on the density of such bacterial cells swimming in a chemical gradient (Schnitzer et al., 1990; Schnitzer, 1993). It was discovered that in the case of $\alpha(\mathrm{x})$ and $\mathrm{v}(\mathrm{x})$ lacking directional dependence, the steady state bacterial density $\rho(\mathrm{x})$ will be inversely proportional to the swimming speed $\mathrm{v}(\mathrm{x})$(Schnitzer et al., 1990; Schnitzer, 1993).

$$\rho(x) \sim \frac{1}{v(x)} \tag{4.2}$$

Tumbling rate dynamics only affect the approach to steady state bacterial density (Schnitzer et al., 1990; Schnitzer, 1993). Long term speed and CW Bias changes observed in the response to osmotic upshifts lead me to ask the question whether this case could apply to osmotaxis.

### 4.3.2 Long term changes in $\alpha$ at high osmolalities

Long term changes in CW Bias at high osmolalities could be due to longer switches or more switches. The results presented in Figure 3.11 and Figure 3.10 show that the mean CW interval does not change at elevated osmolality, but rather that there are more switches. As a result, I expect the mean CCW intervals to shorten at high osmolalities. Figure 4.2 plots the mean CCW interval as a function of osmolality, calculated for VRB and the $\mathrm{T}_{17-20}$ portion of the sucrose data set (Fig. 3.16). $\mathrm{T}_{17-20}$ is considered far enough from the point of osmotic shock that any volume recovery related transients can be disregarded (Pilizota et al., 2012). Using the mean CCW interval as a proxy for the mean

run time, it is evident that runs progressively shorten as osmolality increases. Taking the duration of CCW intervals as an approximation of tumble duration, I calculated the change in tumbling rate and plotted it against the relevant osmotic upshift in the inset of Figure 4.2, demonstrating a long term effect. There are indications that the CW Bias eventually adapts to pre-stimulus levels, but over time scales larger than 15 minutes. (Fig. 3.7 A). Presumably, the tumble rate follows this trend as well.

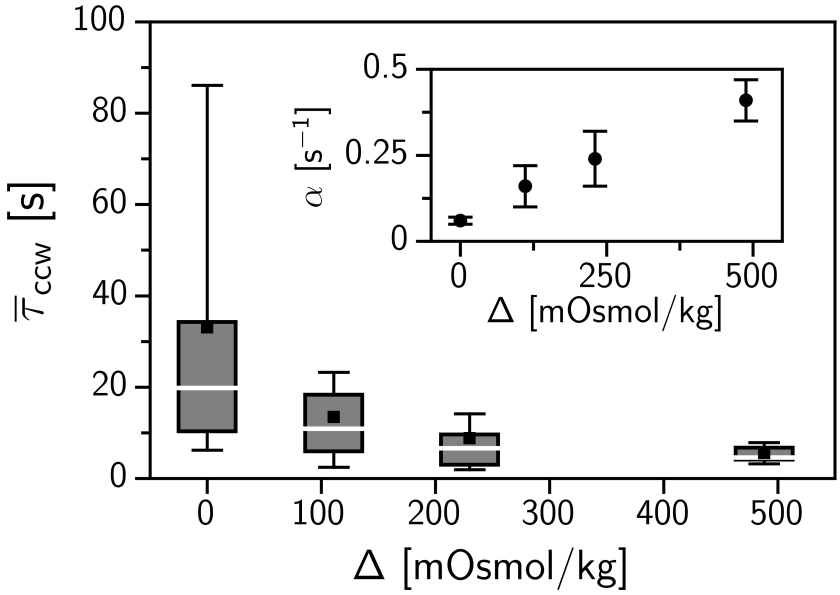


FIGURE 4.2: Mean counter clockwise motor interval, corresponding to cell runs, as a function of osmotic upshift. The "0" condition box contains 96 mean run intervals, calculated by averaging interval lengths over 5 min before osmotic upshift. Subsequent conditions, osmotic upshifts of 111, 230 and 488 mOsmol/kg, contain 21, 20 and 22 single motor values calculated by averaging interval lengths over the time span from t=12 min to t=15 min after an osmotic shock. In the inset, I calculate the tumbling rate $\alpha$ according to equation 4.1, approximating the run times with $\bar{\tau}_{ccw}$ and tumble times with $\bar{\tau}_{cw}$.

### 4.3.3 Motor speed changes could drive osmotaxis

Long term tumble rate changes on time scales presented in Figure 3.11 can not lead to taxis through active sensing due to the network memory extending too much into the past, almost 3 orders of magnitude more than the chemotactic memory (Vladimirov et al., 2009). How CW Bias would behave for smaller

changes in concentration and continuous gradients is, at present, not characterized. If we assume that osmotic pressure influences the CW Bias and motor speed without active sensing, $\alpha(x)$ and $v(x)$ would have no directional dependence and would only depend on the position within an osmotic gradient (Schnitzer et al., 1990; Schnitzer, 1993). In that case, accumulation would be driven by the speed changes discussed in Section 4.2. Furthermore, for the speed changes to be able to drive osmotaxis, the swimming speed should be uniquely defined by the external osmolality. This translates into two requirements, that they are reversible and that they do not depend on the steepness of the gradient. The latter is addressed by a DDM experiment that shows that it does not matter whether a 235 mOsm/kg shock is administered as a single dose or spread in ten steps over two minutes. The population average swimming speeds fall on the same line (Fig. 3.20 B). Reversibility of single motor speed changes is shown in Figure 3.19. Cells washed back from an osmolality of 111 mOsm/kg into VRB attain motor speeds similar to those in VRB that have not been exposed to a sucrose shock. The discrepancy between VRB and "Back to VRB" speeds could be explained by depletion of the endogenous resources due to the cells spending 25 minutes at high osmolality before being put back into VRB. Thus, osmotaxis could arise from changes in motor speed, possibly brought about by an increased proton motive force as a consequence of a heightened metabolic activity that scales with the external osmotic pressure. Such form of taxis has previously been observed in shallow thermal gradients and driven by changes in proton motive force. In that case, equation 4.2 correctly predicted where bacteria would accumulate (Demir et al., 2012).

### 4.3.4 Active or passive sensing?

Whether sensing of osmotic pressure is active or passive is an open question. Measurements of CheY-CheZ kinase activity using FRET revealed a signal in the chemotactic network when cells were stimulated with 100 mM sucrose (Vaknin et al., 2006). It is difficult to compare this result to CW Bias measurements in the 100 mM sucrose condition because the strongest part of the FRET signal falls into the zero bias period (Fig. 1.15 vs Fig. 3.7 A). Also, this is the only currently published measurement of kinase activity under osmotic shocks and it is not known how strong this response is in terms of amplitude

relative to chemotactic signals, and additionally, what is the relationship between the unit change in activity and the change in CW Bias. Another piece of information comes from quantification of receptor methylation after stimulating the cells with 100 mM sucrose for 30 minutes. Receptors were shown to have methylation levels lower than those of unstimulated cells, indicating adaptation to a repellent. The levels were 60% of those without stimulus, suggesting that the osmotic signal was nonsaturating (Qi et al., 1989).
A possible passive change of CW motor bias could come, for example, from an effect of elevated cytoplasmic osmolality on hydration (Parsegian et al., 2000) of motor proteins. The effect of high hydrostatic pressure on the bias of the BFM is thought to come from changes in the rotor ring structure brought about by changes in hydration (Nishiyama et al., 2013). Additionally, transient volume changes could change the amount of crowding in the cytoplasm, affecting protein interactions as well.(Van Den Berg et al., 2017).
In continuous gradients, where input stimuli are much smaller than 100 mM, the activation of the chemotactic network could be small compared to that brought about by chemical ligands. If that were not so, the detection of fine ($\mathrm{nM}$) changes in binding of specific ligands to the receptors could get obscured by the noise arising from similar changes in concentrations of nonspecific solutes. This could be avoided by the sensors having a lower sensitivity for osmotic changes, with the cell having to swim further to sense a measurable change in osmotic pressure. However, since the methylation/demethylation time scales have been pre-tuned for chemotactic memory, which is short term and on a scale of seconds, this could prevent the cell from making temporal comparisons of osmolalities this way (Vladimirov et al., 2009; Segall et al., 1986). In thermotaxis, when the gradient is too shallow for the sensitivity of active sensing, passive sensing was found to bring about changes in proton motive force and drive bacterial accumulation according to equation 4.2 (Demir et al., 2012). Thus osmokinesis, especially with the osmolality uniquely and reversibly defining the value of speed, provides a viable alternative for taxis in response to osmotic gradients without necessitating any changes in the time scales of chemotaxis. However, the reality could be even more complex, with passive or active sensing handling the tactic response based on the shape and steepness of the gradient, just like in thermotaxis (Demir et al., 2012).
Additionally, I have shown that osmokinesis occurs in the $\Delta\mathrm{CheY}$ mutant (Fig.

3.4) . Despite that, mutants lacking CheY have not been shown to be osmotactic on agar plates (Li et al., 1988). It was previously demonstrated that as long as the mutants tumble with a frequency close enough to wild type, osmotaxis will occur in plug assays (Li et al., 1988). Also, strains that are smooth swimmers or extreme tumblers are seriously hampered when it comes to spreading through soft agar (Wolfe et al., 1989). Thus the reason why CheY mutants, despite showing osmokinesis, are not osmotactic could be because of their impaired capacity to spread through a porous medium. Indeed, recent theoretical work suggests an optimal tumble rate for spreading through porous environments, such as agar gels (Licata et al., 2016).

## 4.4 Using NaCl to elevate osmolality

Extending this work to NaCl is underway. NaCl is commonly used for elevating osmolalities alongside sucrose. Unlike sucrose NaCl can enter the periplasm and could serve as a way to compare possible different effects of outer membrane impermeable and permeable solutes (Pilizota et al., 2013). However, NaCl has been shown to not only elevate osmotic pressure but has some specific interactions with the chemosensors (Qi et al., 1989), something that needs to be taken into account when analysing the data. Preliminary results show that steps in NaCl concentration have an effect on CW Bias similar to steps in sucrose, as shown in Figure 3.9. The effect on motor speed appears to be more subtle than with sucrose (Fig. 3.24) and the cells with the smallest effect on speed appear to be those that were already rotating their motors at speeds of >139 Hz, well above the VRB average of 107 Hz. Whether this is a coincidence or not is a question that awaits further data.

## 4.5 Effect of flow

Section 3.3 details the effect of flow pulses on motor rotation. While it is not clear whether and how much effect there is on motor bias, which could also be a chemotactic response to fresh media, there is an effect on speed. Using large beads (1 $\mu$m) attached to truncated flagellar filaments and a syringe pump to deliver flow pulses, I have noticed a subtle effect on speed at a flow rate of

$750\mu\mathrm{l/min}$ (Fig. 3.26 C,D). Upon transitioning to smaller beads, 0.5 $\mu\mathrm{m}$ in diameter, the speed jump became more pronounced, as shown in Figure 3.26 E and F. The most visible effect on motor speed was seen while doing manual buffer to buffer flushes in order to establish a baseline effect for osmotic shock experiments. In these, the rate is not precisely controlled. While 24 $\mu\mathrm{l}$ of VRB is flushed through the channel over 10-15 seconds, giving an average flow rate of 100-150 $\mu l/min$, the speed is not uniform in time. The first few seconds seem to have a much higher flow rate than the following 7-10. Judging by the magnitude of the speed jump, often proceeding as a single step of over $\sim$ 50 Hz in magnitude, the flow rate could, in the initial moments, even exceed $750\mu\mathrm{l/min}$. The jump in speed occurs over a time scale of seconds, as shown on Figure 3.26 G and Figure 3.30. To increase the speed by this amount, the BFM would need to integrate at least 3 or 4 new stator units, which seems unlikely in such a short time. For example, in ressurection experiments, the time between subsequent units integrating is on a scale of minutes. Similar delays between individual stators coming in and out are also present in Figure 3.22 A. Perhaps a more plausible hypothesis is that the sudden large mechanical stimulus speeds up the motor by directly affecting the interactions between constituent proteins of the BFM. To further explore the effect of flow pulses, I plan to characterize the response to various flow rates using various beads. Additionally, I will take steps to fully characterize the flow velocity field at the surface, enabling me to calculate the forces on the motor.

## 4.6 Concluding remarks and future work

In this thesis I have characterized the effect of step-wise osmotic upshifts on the speed and bias of flagellar motors and also on swimming populations of *Escherichia coli* cells. The changes in motor speed are reversible and seem to be uniquely defined by the final osmolality and could, in principle, lead to taxis provided that sensing of osmotic pressure does not happen actively through temporal comparisons by chemoreceptors but passively through physical action of osmotic pressure on the BFM itself or on the cell metabolism. Several open questions remain and I hope to address some of them in future work. The question of the sensitivity with which the cell can measure osmotic pressure is closely related to whether sensing is active or passive. I plan to use the motor

assay and microfluidic devices with swimming cells to explore small steps and shallow gradients, in order to quantify the minimum step in osmolality that the cell can detect. Additionally, by using a strain without native CheY but expressing a mutant protein, CheY**, which mimics CheY-P (Scharf et al., 1998), I could control the amount of tumbling in a strain completely lacking chemotactic machinery . This would permit me to explore whether the components of the chemotactic network are really needed for sensing the osmolality or just their presence leads to sufficient tumbliness, which allows cells to effectively migrate through soft agar gels and exhibit osmotaxis in plug asays (Li et al., 1988; Wolfe et al., 1989). These two experiments could significantly contribute to answering the open question of whether or not there is active sensing.
Another interesting problem are the origins of the speed changes observed in Section sec:speed. I hypothesise in Section 4.2.2 that the reason could be an elevated PMF as a consequence of an increased metabolism. To verify this hypothesis I plan to measure oxygen levels in a suspension of cells in a condition of elevated osmolality and combine it with single cell measurements of pH and membrane voltage, currently being developed by other members of the Pilizota lab. This would provide valuable insight into cell energetics and PMF dynamics an osmotic challenge. Combining this with fluorescence measurements of stator unit number, like those performed by Leake et al. (Leake et al., 2006), I could better address the question of the origin of post-osmotic shock speed up.
Other exciting directions include the mechanics of the effect of flow on motors driving small beads, comparing osmotactic effects of solutes with different membrane permeabilities and opposing gradients of chemicals and osmolality. And perhaps the most exciting of all is the difficult question of how all of this influences the life of *Escherichia coli*, not in the lab, but in its natural habitat, the intestinal system of humans and warm blooded animals.

# Chapter 5

# Appendices

**Appendix A** Figure 5.1 shows the Lab View program developed in this work to run the data acquisition from the PSD (Newport, USA) using a DAQ board (National Instruments, USA). More information is available in

**Appendix B** Section 2.2. Figure 5.2 shows the drawing for machining of an vertical extension post for Thorlabs VB01/M. Included here or future reference, and in case of need to machine more units.

**Appendix C** Figure 5.3 is a drawing for machining of the metal base that supports the IR laser.

**Publication** Rosko J, Martinez V A, Poon W C K and Pilizota T**. Osmotaxis in Escherichia coli through changes in motor speed. (In Revision, arXiv:1703.03926).

**GitHub repository** A selection of python functions used developed in this thesis work is located in the following github repository:
https://github.com/jrosko/ThesisCodeGit
These are useful for splitting and merging large files from the data acquisition, decimating data and analysing speeds and biases.

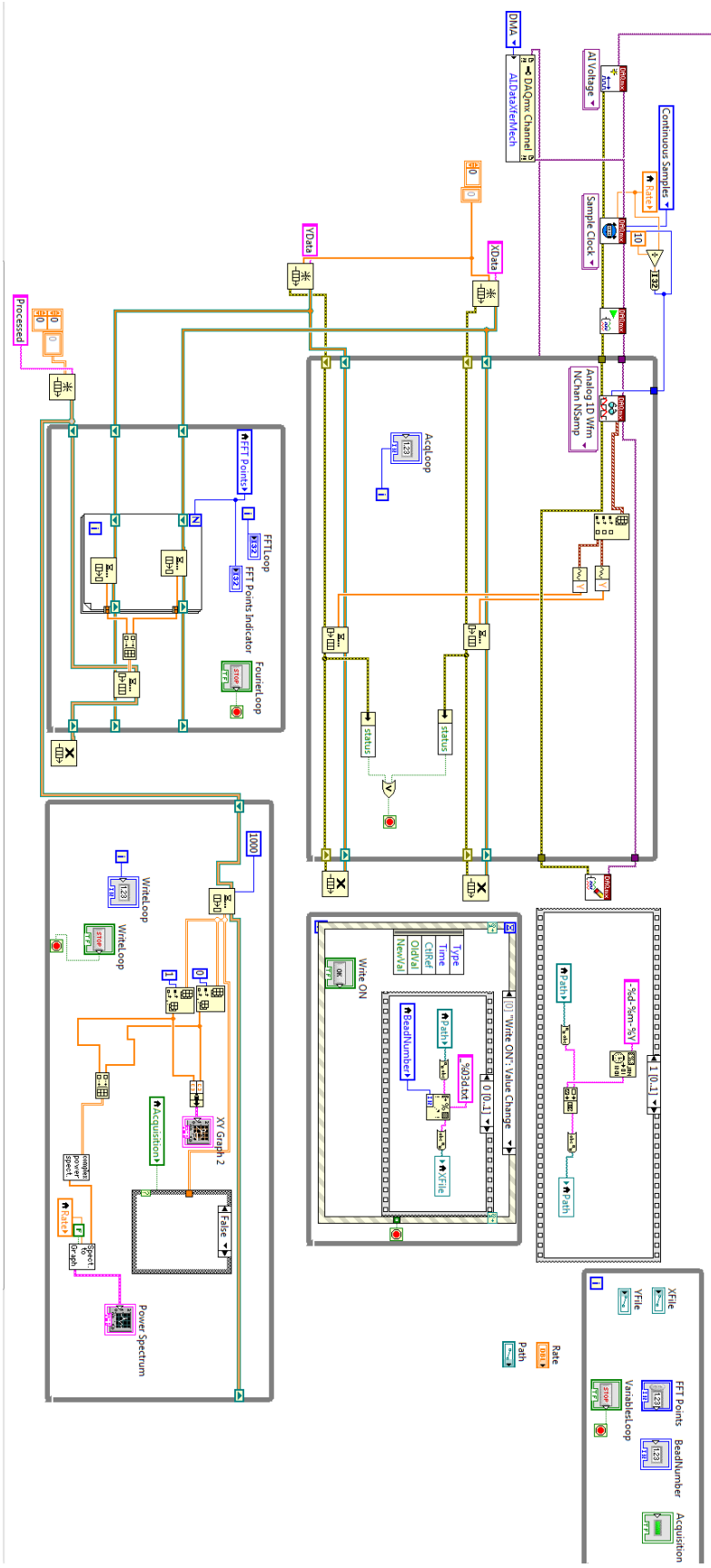


FIGURE 5.1: The Lab Veiw program I have written, that currently runs the data acquisition from the PSD. (Section 2.2 )

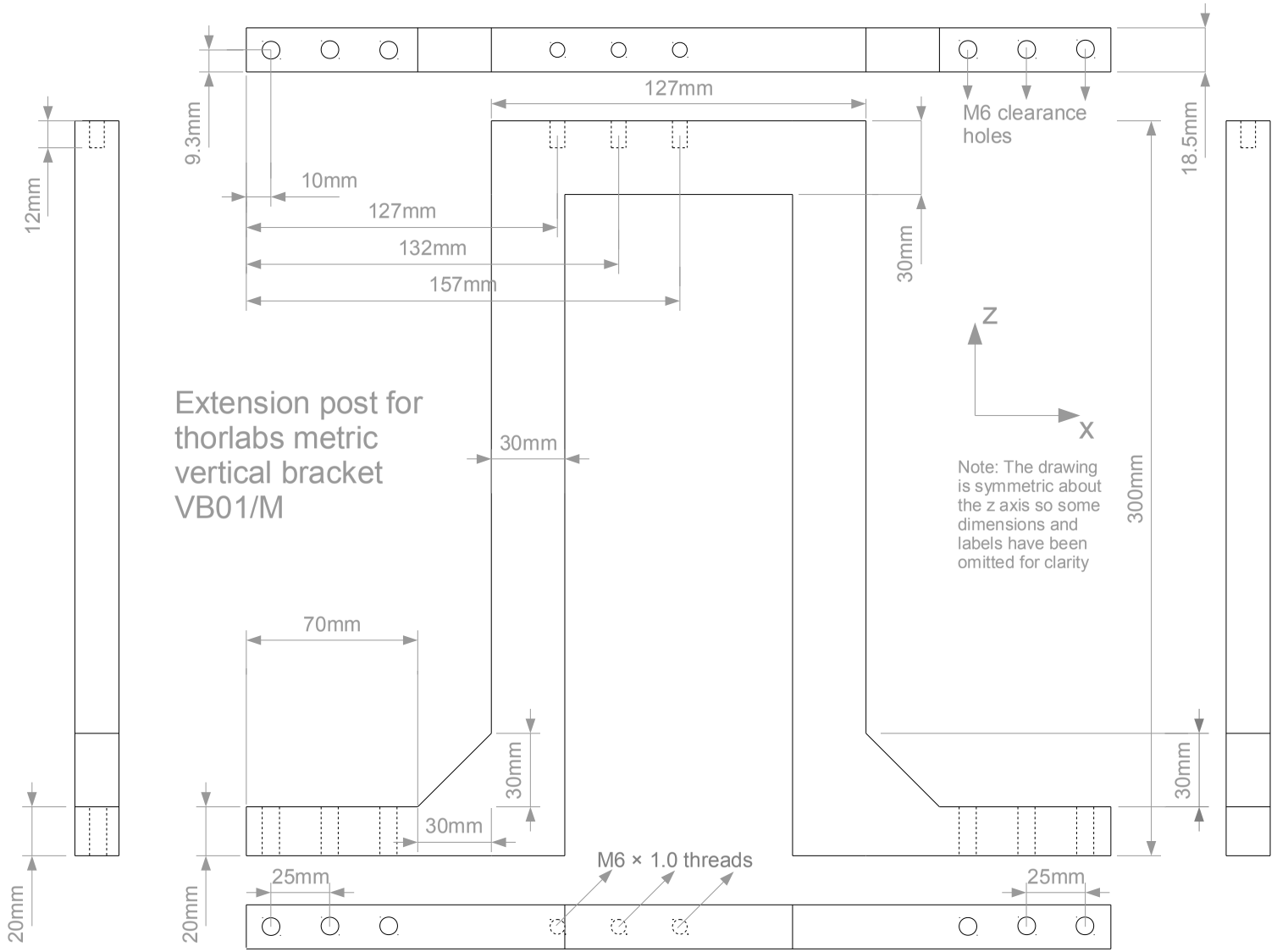


FIGURE 5.2: My design for the extension post for Thorlabs VB01/M brackets which hold vertical the parts of the microscope presented on Fig 2.2 A and 2.3 C

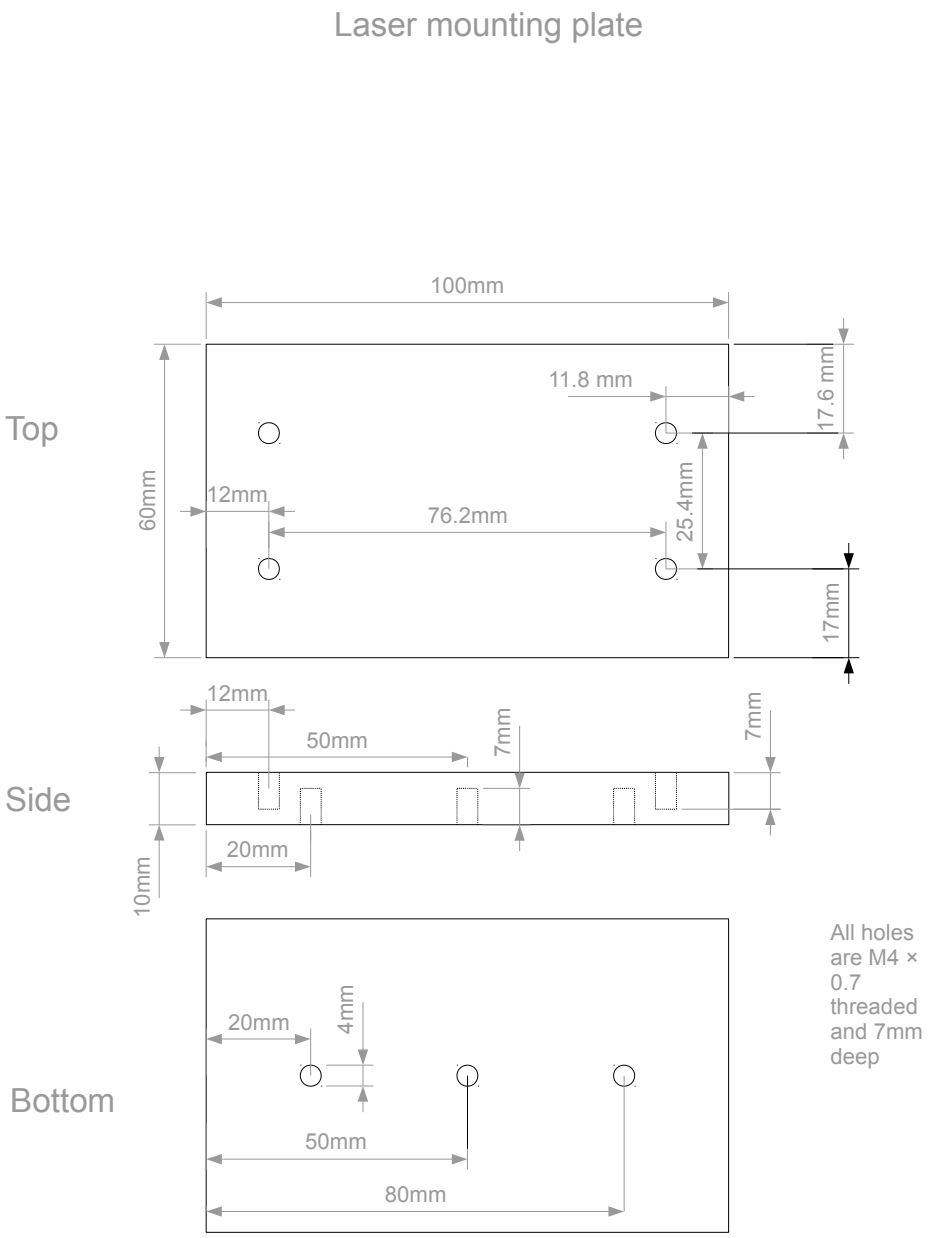


FIGURE 5.3: Design for the mounting plate for the IR Laser used in the optical trap.

# Bibliography

Adler, J. (1973). "A Method for Measuring Chemotaxis and Use of the Method to Determine Optimum Conditions for Chemotaxis by Escherichia coli". In: *Journal of General Microbiology* 74.1, pp. 77–91. ISSN: 0022-1287. DOI: 10.1099/00221287-74-1-77. URL: http://mic.microbiologyresearch.org/content/journal/micro/10.1099/00221287-74-1-77.

Adler, J (1975). "Chemotaxis in Bacteria". In: *Annual Review of Biochemistry* 44.1, pp. 341–356. ISSN: 0066-4154. DOI: 10.1146/annurev.bi.44.070175.002013.

Adler, J, G L Hazelbauer, and M M Dahl (1973). "Chemotaxis toward sugars in Escherichia coli". In: *Journal of Bacteriology* 115.3, pp. 824–847. ISSN: 00219193.

Adler, J. et al. (1988). "Osmotaxis in Escherichia coli". In: *Cold Spring Harbor Symposia on Quantitative Biology* 53.1, pp. 19–22. ISSN: 00917451. DOI: 10.1101/SQB.1988.053.01.005.

Allersma, Miriam W et al. (1998). "Two-Dimensional Tracking of ncd Motility by Back Focal Plane Interferometry". In: *Biophysical Journal* 74.2, pp. 1074–1085. ISSN: 00063495. DOI: 10.1016/S0006-3495(98)74031-7.

Armitage, JP (1999). "Bacterial tactic response". In: *Adv Microb Physiol* 41, pp. 229–289.

Ashkin, A. (1992). "Forces of a single-beam gradient laser trap on a dielectric sphere in the ray optics regime". In: *Biophysical Journal* 61.2, pp. 569–582. ISSN: 00063495. DOI: 10.1016/S0006-3495(92)81860-X.

Ashkin, A et al. (1986). "Observation of a single-beam gradient force optical trap for dielectric particles." In: *Optics letters* 11.5, p. 288. ISSN: 0146-9592. DOI: https://doi.org/10.1364/OL.11.000288. eprint: 1411.1912.

Ashkin, A., J. M. Dziedzic, and T. Yamane (1987a). "Optical trapping and manipulation of single cells using infrared laser beams". In: *Nature* 330.6150, pp. 769–771. ISSN: 0028-0836. DOI: 10.1038/330769a0.

Ashkin, A and J M Dziedzic (1987b). "Optical trapping and manipulation of viruses and bacteria". In: *Science* 235.1984, pp. 1517–1520. ISSN: 0036-8075. DOI: 10.1126/science.3547653.

Bai, Fan et al. (2010). "Conformational spread as a mechanism for cooperativity in the bacterial flagellar switch." In: *Science* 327.5966, pp. 685–689. ISSN: 0036-8075. DOI: 10.1126/science.1182105.

Bai, Fan et al. (2013). "Populational heterogeneity vs. temporal fluctuation in escherichia coli flagellar motor switching". In: *Biophysical Journal* 105.9, pp. 2123–2129. ISSN: 00063495. DOI: 10.1016/j.bpj.2013.09.043.

Baldwin, W. W. et al. (1995). "Growth and buoyant density of Escherichia coli at very low osmolarities". In: *Journal of Bacteriology* 177.1, pp. 235–237. ISSN: 00219193. DOI: 10.1128/jb.177.1.235-237.1995.

Barnakov, Alexander N., Ludmila A. Barnakova, and Gerald L. Hazelbauer (1998). "Comparison in vitro of a high- and a low-abundance chemoreceptor of Escherichia coli: Similar kinase activation but different methyl-accepting activities". In: *Journal of Bacteriology* 180.24, pp. 6713–6718. ISSN: 00219193.

Berg, HOWARD C. and DOUGLAS A. BROWN (1972). "Chemotaxis in Escherichia coli analysed by Three-dimensional Tracking". In: *Nature* 239.5374, pp. 500–504. ISSN: 0028-0836. DOI: 10.1038/239500a0.

Berg, Howard C and Linda Turner (1993a). "Torque generated by the Flagellar motor of Escherichia coli". In: *Biophysical Journal* 65.5, pp. 2201–2216. ISSN: 0006-3495. DOI: 10.1016/S0006-3495(93)81278-5.

— (1993b). "Torque generated by the Flagellar motor of Escherichia coli". In: *Biophysical Journal* 65.5, pp. 2201–2216. ISSN: 0006-3495. DOI: 10.1016/S0006-3495(93)81278-5.

Berne, B. J. and R. Pecora (2000). *Dyanmic Light Scattering*. Dover, New York.

Bettelheim, K A et al. (1974). "Escherichia coli serotype distribution in man and animals." In: *The Journal of hygiene* 73.3, pp. 467–71. ISSN: 0022-1724.

Bibikov, Sergei I. et al. (2004). "Methylation-independent aerotaxis mediated by the Escherichia coli Aer protein". In: *Journal of Bacteriology* 186.12, pp. 3730–3737. ISSN: 00219193. DOI: 10.1128/JB.186.12.3730-3737.2004.

Blattner, F. R. et al. (1997). "The Complete Genome Sequence of Escherichia coli K-12". In: *Science* 277.September, pp. 1453–1462.

Block, S M, L S Goldstein, and B J Schnapp (1990). "Bead movement by single kinesin molecules studied with optical tweezers." In: *Nature* 348.6299, pp. 348–52. ISSN: 0028-0836. DOI: 10.1038/348348a0.

Born, Max and Emil Wolf (1999). *Principles of Optics (7th Ed)*. Cambridge University Press.

Bower, Jean M., Danelle S. Eto, and Matthew A. Mulvey (2005). "Covert Operations of Uropathogenic Escherichia coli within the Urinary Tract". In: *Traffic* 6.1, pp. 18–31. ISSN: 1398-9219. DOI: 10.1111/j.1600-0854.2004.00251.x.

Branch, Richard W. et al. (2014). "Adaptive remodelling by FliN in the bacterial rotary motor". In: *Journal of Molecular Biology* 426.19, pp. 3314–3324. ISSN: 10898638. DOI: 10.1016/j.jmb.2014.07.009.

Braun, Timothy F et al. (2004). "Arrangement of core membrane segments in the MotA/MotB proton-channel complex of Escherichia coli." In: *Biochemistry* 43.1, pp. 35–45. ISSN: 0006-2960. DOI: 10.1021/bi035406d.

Briegel, A. et al. (2012). "Bacterial chemoreceptor arrays are hexagonally packed trimers of receptor dimers networked by rings of kinase and coupling proteins". In: *Proceedings of the National Academy of Sciences* 109.10, pp. 3766–3771. ISSN: 0027-8424. DOI: 10.1073/pnas.1115719109.

Cantwell, Brian J. et al. (2003). "CheZ phosphatase localizes to chemoreceptor patches via CheA-short". In: *Journal of Bacteriology* 185.7, pp. 2354–2361. ISSN: 00219193. DOI: 10.1128/JB.185.7.2354-2361.2003.

Cayley, D Scott, Harry J Guttman, and M Thomas Record, Jr. (2000). "Biophysical characterization of changes in amounts and activity of Escherichia coli cell and compartment water and turgor pressure in response to osmotic stress." In: *Biophysical journal* 78.April, pp. 1748–1764. ISSN: 00063495. DOI: 10.1016/S0006-3495(00)76726-9.

Chen, Songye et al. (2011). "Structural diversity of bacterial flagellar motors". In: *The EMBO Journal* 30.14, pp. 260–275. ISSN: 0261-4189. DOI: 10.1038/emboj.2011.186.

Chen, X and Howard C. Berg (2000a). "Torque-speed relationship of the flagellar rotary motor of Escherichia coli." In: *Biophysical journal* 78.2, pp. 1036–1041. ISSN: 00063495. DOI: 10.1016/S0006-3495(00)76662-8.

— (2000b). "Torque-speed relationship of the flagellar rotary motor of Escherichia coli." In: *Biophysical journal* 78.2, pp. 1036–1041. ISSN: 00063495. DOI: 10.1016/S0006-3495(00)76662-8.

Chong, Yuwen et al. (2007). "Human intestinal tissue tropism in Escherichia coli O157:H7 - Initial colonization of terminal ileum and Peyer's patches and minimal colonic adhesion ex vivo". In: *Microbiology* 153.3, pp. 794–802. ISSN: 13500872. DOI: 10.1099/mic.0.2006/003178-0.

Clarke, S and D E Koshland (1979). "Membrane-Receptors for Aspartate and Serine in Bacterial Chemotaxis". In: *Journal of Biological Chemistry* 254.19, pp. 9695–9702.

Cluzel, P. (2000). "An Ultrasensitive Bacterial Motor Revealed by Monitoring Signaling Proteins in Single Cells". In: *Science* 287.5458, pp. 1652–1655. ISSN: 00368075. DOI: 10.1126/science.287.5458.1652. URL: http://www.sciencemag.org/cgi/doi/10.1126/science.287.5458.1652.

Csonka, L N and A D Hanson (1991). "Prokaryotic Osmoregulation: Genetics and Physiology". In: *Annual Review of Microbiology* 45.1, pp. 569–606. ISSN: 0066-4227. DOI: 10.1146/annurev.mi.45.100191.003033.

Darnton, Nicholas C. et al. (2007). "On torque and tumbling in swimming Escherichia coli". In: *Journal of Bacteriology* 189.5, pp. 1756–1764. ISSN: 00219193. DOI: 10.1128/JB.01501-06.

Dawes, E A and D W Ribbons (1965). "Studies on the Endogenous Metabolism of Escherichia Coli." In: *The Biochemical journal* 95, pp. 332–343. ISSN: 02646021.

Delalez, Nicolas J., Richard M. Berry, and Judith P. Armitage (2014). "Stoichiometry and turnover of the bacterial flagellar switch protein FliN". In: *mBio* 5.4, pp. 1–5. ISSN: 21507511. DOI: 10.1128/mBio.01216-14.

Demir, Mahmut and Hanna Salman (2012). "Bacterial thermotaxis by speed modulation". In: *Biophysical Journal* 103.8, pp. 1683–1690. ISSN: 00063495. DOI: 10.1016/j.bpj.2012.09.005.

DeRosier, David (2006). "Bacterial Flagellum: Visualizing the Complete Machine In Situ". In: *Current Biology* 16.21, pp. 928–930. ISSN: 09609822. DOI: 10.1016/j.cub.2006.09.053.

Elsas, Jan Dirk van et al. (2011). "Survival of Escherichia coli in the environment: fundamental and public health aspects". In: *The ISME Journal* 5.2, pp. 173–183. ISSN: 1751-7362. DOI: 10.1038/ismej.2010.80.

Fahrner, Karen A., William S. Ryu, and Howard C. Berg (2003). "Bacterial flagellar switching under load". In: *Nature* 423.June, p. 2003. ISSN: 00280836. DOI: 10.1038/423938a.

Fällman, Erik and Ove Axner (2003). "Influence of a Glass-Water Interface on the On-Axis Trapping of Micrometer-Sized Spherical Objects by Optical Tweezers". In: *Applied Optics* 42.19, pp. 3915–3926. ISSN: 0003-6935. DOI: 10.1364/AO.42.003915.

Feng, Xiuhong, Angela A. Lilly, and Gerald L. Hazelbauer (1999). "Enhanced function conferred on low-abundance chemoreceptor trg by a methyltransferase-docking site". In: *Journal of Bacteriology* 181.10, pp. 3164–3171. ISSN: 00219193.

Francis, Noreen R. et al. (1994). "Isolation, Characterization and Structure of Bacterial Flagellar Motors Containing the Switch Complex". In: *Journal of Molecular Biology* 235.4, pp. 1261–1270. ISSN: 00222836. DOI: 10.1006/jmbi.1994.1079.

Fukuoka, Hajime et al. (2014). "Direct Imaging of Intracellular Signaling Components That Regulate Bacterial Chemotaxis". In: *Sci. Signal.* 7.319, ra32–ra32. ISSN: 1945-0877, 1937-9145. DOI: 10.1126/scisignal.2004963.

Fung, D C and H C Berg (1995). "Powering the flagellar motor of Escherichia coli with an external voltage source". In: *Nature* 375.6534, pp. 809–812. ISSN: 0028-0836. DOI: 10.1038/375809a0.

Gabel, Christopher V and Howard C Berg (2003). "The speed of the flagellar rotary motor of Escherichia coli varies linearly with protonmotive force." In: *Proceedings of the National Academy of Sciences of the United States of America* 100, pp. 8748–8751. ISSN: 0027-8424. DOI: 10.1073/pnas.1533395100.

Ghislain, Lucien P., Neil A. Switz, and Watt W. Webb (1994). "Measurement of small forces using an optical trap". In: *Review of Scientific Instruments* 65.9, pp. 2762–2768. ISSN: 00346748. DOI: 10.1063/1.1144613.

Gittes, Frederick and Christoph F Schmidt (1998). "Interference model for back-focal-plane displacement detection in optical tweezers". In: *Optics Letters* 23.1, p. 7. ISSN: 0146-9592. DOI: 10.1364/OL.23.000007.

Grange, Wilfried et al. (2002). "Optical tweezers system measuring the change in light momentum flux". In: *Review of Scientific Instruments* 73.6, p. 2308. ISSN: 00346748. DOI: 10.1063/1.1477608.

Greenfield, Derek et al. (2009). "Self-organization of the Escherichia coli chemotaxis network imaged with super-resolution light microscopy". In: *PLoS Biology* 7.6. ISSN: 15449173. DOI: 10.1371/journal.pbio.1000137.

Hazelbauer, G. L., P. Engstrom, and S. Harayama (1981a). "Methyl-accepting chemotaxis protein III and transducer gene trg". In: *Journal of Bacteriology* 145.1, pp. 43–49. ISSN: 00219193.

Hazelbauer, G. L. and P. Engstrom (1981b). "Multiple forms of methyl-accepting chemotaxis proteins distinguished by a factor in addition to multiple methylation". In: *Journal of Bacteriology* 145.1, pp. 35–42. ISSN: 00219193.

Hess, J Fred, Robert B Bourret, and Melvin I Simon (1988). "Histidine phosphorylation and phosphoryl group transfer in bacterial chemotaxis". In: *Nature* 336.10.Nov. Pp. 139–143. ISSN: 0028-0836. DOI: 10.1038/336139a0.

Hosu, Basarab G., Vedavalli S. J. Nathan, and Howard C. Berg (2016). "Internal and external components of the bacterial flagellar motor rotate as a unit". In: *Proceedings of the National Academy of Sciences* 113.17, p. 201511691. ISSN: 0027-8424. DOI: 10.1073/pnas.1511691113.

Ishii, Satoshi and Michael J. Sadowsky (2008). "Escherichia coli in the Environment: Implications for Water Quality and Human Health". In: *Microbes and Environments* 23.2, pp. 101–108. ISSN: 1342-6311. DOI: 10.1264/jsme2.23.101.

Jasuja, Ravi et al. (1999). "Chemotactic Responses of Escherichia coli to Small Jumps of Photoreleased l-Aspartate". In: *Biophysical Journal* 76.3, pp. 1706–1719. ISSN: 00063495. DOI: 10.1016/S0006-3495(99)77329-7.

Jones, C.L. (2015). "HHS Public Access". In: 33.4, pp. 395–401. ISSN: 1527-5418. DOI: 10.1038/nbt.3121.ChIP-nexus. arXiv: 15334406.

Kehry, M. R., T. G. Doak, and F. W. Dahlquist (1984). "Stimulus-induced changes in methylesterase activity during chemotaxis in Escherichia coli". In: *Journal of Biological Chemistry* 259.19, pp. 11828–11835. ISSN: 00219258.

— (1985). "Sensory adaptation in bacterial chemotaxis: Regulation of demethylation". In: *Journal of Bacteriology* 163.3, pp. 983–990. ISSN: 00219193.

Kentner, David et al. (2006). "Determinants of chemoreceptor cluster formation in Escherichia coli". In: *Molecular Microbiology* 61.2, pp. 407–417. ISSN: 0950382X. DOI: 10.1111/j.1365-2958.2006.05250.x.

Kojima, S. and D. F. Blair (2001). "Conformational change in the stator of the bacterial flagellar Motor". In: *Biochemistry* 40.43, pp. 13041–13050. ISSN: 00062960. DOI: 10.1021/bi011263o.

Kojima, Seiji and David F Blair (2004). "Solubilization and purification of the MotA/MotB complex of Escherichia coli." In: *Biochemistry* 43, pp. 26–34. ISSN: 0006-2960. DOI: 10.1021/bi0354051.

Kondoh, H, C B Ball, and J Adler (1979). "Identification of a methyl-accepting chemotaxis protein for the ribose and galactose chemoreceptors of Escherichia coli." In: *Proceedings of the National Academy of Sciences of the United States of*

*America* 76.1, pp. 260–264. ISSN: 0027-8424. DOI: 10.1073/pnas.76.1.260.

Krembel, Anna K., Silke Neumann, and Victor Sourjik (2015). "Universal response-adaptation relation in bacterial chemotaxis". In: *Journal of Bacteriology* 197.2, pp. 307–313. ISSN: 10985530. DOI: 10.1128/JB.02171-14.

Lackraj, Tracy et al. (2016). "Differential modulation of flagella expression in enterohaemorrhagic Escherichia coli O157: H7 by intestinal short-chain fatty acid mixes". In: *Microbiology (United Kingdom)* 162.10, pp. 1761–1772. ISSN: 14652080. DOI: 10.1099/mic.0.000357.

Leake, Mark C et al. (2006). "Stoichiometry and turnover in single, functioning membrane protein complexes." In: *Nature* 443.7109, pp. 355–358. ISSN: 0028-0836. DOI: 10.1038/nature05135.

Lee, Lawrence K et al. (2010). "Structure of the torque ring of the flagellar motor and the molecular basis for rotational switching." In: *Nature* 466.7309, pp. 996–1000. ISSN: 0028-0836. DOI: 10.1038/nature09300.

Lele, Pushkar P, Basarab G Hosu, and Howard C Berg (2013). "Dynamics of mechanosensing in the bacterial flagellar motor." In: *Proceedings of the National Academy of Sciences of the United States of America* 110.29, pp. 11839–44. ISSN: 1091-6490. DOI: 10.1073/pnas.1305885110.

Levenson, Robert, Hongjun Zhou, and Frederick W Dahlquist (2012). "Structural Insights into the Interaction between the Bacterial Flagellar Motor Proteins FliF and FliG". In: *Biochemistry* 51.25, pp. 5052–5060. ISSN: 0006-2960. DOI: 10.1021/bi3004582.

Li, C et al. (1988). "Osmotaxis in Escherichia coli". In: 85.December, pp. 19–22. DOI: 10.1101/SQB.1988.053.01.005.

Li, C. and J. Adler (1993). "Escherichia coli shows two types of behavioral responses to osmotic upshift". In: *Journal of Bacteriology* 175.9, pp. 2564–2567. ISSN: 00219193.

Li, Mingshan and Gerald L. Hazelbauer (2004). "Cellular stoichiometry of the components of the chemotaxis signaling complex". In: *Journal of Bacteriology* 186.12, pp. 3687–3694. ISSN: 00219193. DOI: 10.1128/JB.186.12.3687-3694.2004.

Licata, Nicholas A. et al. (2016). "Diffusion of Bacterial Cells in Porous Media". In: *Biophysical Journal* 110.1, pp. 247–257. ISSN: 15420086. DOI: 10.1016/j.bpj.2015.09.035.

Lo, Chien-Jung et al. (2007). "Nonequivalence of Membrane Voltage and Ion-Gradient as Driving Forces for the Bacterial Flagellar Motor at Low Load". In: *Biophysical Journal* 93.1, pp. 294–302. ISSN: 00063495. DOI: 10.1529/biophysj.106.095265.

Lo, Chien-Jung et al. (2013). "Mechanism and kinetics of a sodium-driven bacterial flagellar motor". In: *Pnas*, E2544–E2551. DOI: 10.1073/pnas.1301664110/-/DCSupplemental.www.pnas.org/cgi/doi/10.1073/pnas.1301664110.

Lovely, P. and F. Dahlquist (1975). "Statistical measures of bacterial motility and chemotaxis". In: *J Theor Biol* 50.2, pp. 477–496.

Lux, R et al. (1999). "Elucidation of a PTS-carbohydrate chemotactic signal pathway in Escherichia coli using a time-resolved behavioral assay." In: *Molecular biology of the cell* 10.4, pp. 1133–1146. ISSN: 1059-1524.

Lynch, Michael J. et al. (2017). "Co-Folding of a FliF-FliG Split Domain Forms the Basis of the MS:C Ring Interface within the Bacterial Flagellar Motor". In: *Structure* 25.2, pp. 317–328. ISSN: 09692126. DOI: 10.1016/j.str.2016.12.006.

Ma, Qi et al. (2016). "Bacterial Flagellar Motor Switch in Response to CheY-P Regulation and Motor Structural Alterations". In: *Biophysical Journal* 110.6, pp. 1411–1420. ISSN: 15420086. DOI: 10.1016/j.bpj.2016.02.023.

Mandadapu, Kranthi K et al. (2015). "Mechanics of torque generation in the bacterial flagellar motor". In: *Pnas* 112.32, E4281–E4389. ISSN: 0027-8424. DOI: 10.1073/pnas.1501734112. arXiv: arXiv:1501.02883v1.

Manson, M D et al. (1986). "Peptide chemotaxis in E. coli involves the Tap signal transducer and the dipeptide permease." In: *Nature* 321.6067, pp. 253–6. ISSN: 0028-0836. DOI: 10.1038/321253a0.

Mao, H., P. S. Cremer, and M. D. Manson (2003). "A sensitive, versatile microfluidic assay for bacterial chemotaxis". In: *Proceedings of the National Academy of Sciences* 100.9, pp. 5449–5454. ISSN: 0027-8424. DOI: 10.1073/pnas.0931258100.

Martinez, Vincent A. et al. (2012). "Differential dynamic microscopy: A high-throughput method for characterizing the motility of microorganisms". In: *Biophysical Journal* 103.8, pp. 1637–1647. ISSN: 00063495. DOI: 10.1016/j.bpj.2012.08.045. arXiv: 1202.1702.

Martinez, Vincent A. et al. (2014). "Flagellated bacterial motility in polymer solutions". In: *Proceedings of the National Academy of Sciences* 111.50, pp. 17771–

17776. ISSN: 0027-8424. DOI: 10.1073/pnas.1415460111. arXiv: 1411.5950.

Meacci, Giovanni and Yuhai Tu (2009). "Dynamics of the bacterial flagellar motor with multiple stators." In: *Proceedings of the National Academy of Sciences of the United States of America* 106.10, pp. 3746–51. ISSN: 1091-6490. DOI: 10.1073/pnas.0809929106. arXiv: arXiv:0901.0936v1.

Meir, Yigal et al. (2010). "Precision and kinetics of adaptation in bacterial chemotaxis". In: *Biophysical Journal* 99.9, pp. 2766–2774. ISSN: 00063495. DOI: 10.1016/j.bpj.2010.08.051.

Mesibov, R and J Adler (1972). "Chemotaxis toward amino-acids in Escherichia coli". In: *Journal of Bacteriology* 112.1, 315–&. ISSN: 0021-9193.

Min, T. L. et al. (2012). "Chemotactic adaptation kinetics of individual Escherichia coli cells". In: *Proceedings of the National Academy of Sciences* 109.25, pp. 9869–9874. ISSN: 0027-8424. DOI: 10.1073/pnas.1120218109.

Min, Taejin L et al. (2009). "High-resolution, long-term characterization of bacterial motility using optical tweezers." In: *Nature methods* 6.11, pp. 831–835. ISSN: 1548-7091. DOI: 10.1038/nmeth.1380.

Mirsaidov, Utkur et al. (2008). "Optimal optical trap for bacterial viability". In: pp. 1–7. DOI: 10.1103/PhysRevE.78.021910.

Moxley, Rodney A (2004). "Escherichia coli O157 : H7 : an update on intestinal colonization and virulence mechanisms". In: *Health (San Francisco)* 5.1, pp. 15–34. ISSN: 14752654. DOI: 10.1079/AHRR200463.

Nakamura, Shuichi et al. (2010). "Evidence for symmetry in the elementary process of bidirectional torque generation by the bacterial flagellar motor." In: *Proceedings of the National Academy of Sciences of the United States of America* 107, pp. 17616–17620. ISSN: 0027-8424. DOI: 10.1073/pnas.1007448107.

Neuman, K C et al. (1999). "Characterization of photodamage to Escherichia coli in optical traps." In: *Biophysical journal* 77.5, pp. 2856–63. ISSN: 1542-0086. DOI: 10.1016/S0006-3495(99)77117-1.

Neuman, Keir C. and Steven M. Block (2004). "Optical trapping". In: *Review of Scientific Instruments* 75.9, pp. 2787–2809. ISSN: 00346748. DOI: 10.1063/1.1785844.

Neumann, Silke, Karin Grosse, and Victor Sourjik (2012). "Chemotactic signaling via carbohydrate phosphotransferase systems in Escherichia coli".

In: *Proceedings of the National Academy of Sciences* 109.30, pp. 12159–12164. ISSN: 0027-8424. DOI: 10.1073/pnas.1205307109.

Neumann, Silke et al. (2014). "Imprecision of adaptation in Escherichia coli chemotaxis". In: *PLoS ONE* 9.1, pp. 1–6. ISSN: 19326203. DOI: 10.1371/journal.pone.0084904.

Nirody, Jasmine A., Yi-Ren Sun, and Chien-Jung Lo (2017). "The biophysicist's guide to the bacterial flagellar motor". In: *Advances in Physics: X* 2.2, pp. 324–343. DOI: 10.1080/23746149.2017.1289120.

Nishiyama, Masayoshi et al. (2013). "High hydrostatic pressure induces counterclockwise to clockwise reversals of the Escherichia coli flagellar motor". In: *Journal of Bacteriology* 195.8, pp. 1809–1814. ISSN: 00219193. DOI: 10.1128/JB.02139-12.

Parkinson, John S., Gerald L. Hazelbauer, and Joseph J. Falke (2015). "Signaling and sensory adaptation in Escherichia coli chemoreceptors: 2015 update". In: *Trends in Microbiology* 23.5, pp. 257–266. ISSN: 18784380. DOI: 10.1016/j.tim.2015.03.003.

Parsegian, V a, R P Rand, and D C Rau (2000). "Osmotic stress, crowding, preferential hydration, and binding: A comparison of perspectives." In: *Proceedings of the National Academy of Sciences of the United States of America* 97.8, pp. 3987–3992. ISSN: 0027-8424. DOI: 10.1073/pnas.97.8.3987.

Partridge, Jonathan D., Vincent Nieto, and Rasika M. Harshey (2015). "A new player at the flagellar motor: FliL controls both motor output and bias". In: *mBio* 6.2, pp. 1–11. ISSN: 21507511. DOI: 10.1128/mBio.02367-14.

Perroud, Bertrand and Daniel Le Rudulier (1985). "Glycine betaine transport in Escherichia coli: osmotic modulation". In: *Journal of Bacteriology* 161.1, pp. 393–401. ISSN: 0021-9193.

Pfeffer, W. (1888). "'Uber Chemotaktische Bewegungen von Bacterien, Flagellaten, und Volvocineen ". In: *Untersuchungen aus dem Botanischen Institut in T'ubingen* 2, pp. 582–661.

Pilizota, Teuta et al. (2007). "A Programmable Optical Angle Clamp for Rotary Molecular Motors". In: *Biophysical Journal* 93.1, pp. 264–275. ISSN: 00063495. DOI: 10.1529/biophysj.106.091074.

Pilizota, Teuta and Joshua W. Shaevitz (2012). "Fast, multiphase volume adaptation to hyperosmotic shock by escherichia coli". In: *PLoS ONE* 7.4, pp. 1–10. ISSN: 19326203. DOI: 10.1371/journal.pone.0035205.

— (2013). "Plasmolysis and cell shape depend on solute outer-membrane permeability during hyperosmotic shock in E. coli". In: *Biophysical Journal* 104.12, pp. 2733–2742. ISSN: 00063495. DOI: 10.1016/j.bpj.2013.05.011.

— (2014). "Origins of escherichia coli growth rate and cell shape changes at high external osmolality". In: *Biophysical Journal* 107.8, pp. 1962–1969. ISSN: 15420086. DOI: 10.1016/j.bpj.2014.08.025.

Qi, Y L and Julius Adler (1989). "Salt taxis in Escherichia coli bacteria and its lack in mutants." In: *Proceedings of the National Academy of Sciences of the United States of America* 86.21, pp. 8358–8362. ISSN: 0027-8424. DOI: 10.1073/pnas.86.21.8358.

Reader, R W et al. (1979). "Pleiotropic aspartate taxis and serine taxis mutants of Escherichia coli." In: *Journal of general microbiology* 111.2, pp. 363–74. ISSN: 0022-1287. DOI: 10.1099/00221287-111-2-363.

Reid, Stuart W et al. (2006). "The maximum number of torque-generating units in the flagellar motor of Escherichia coli is at least 11." In: *Proceedings of the National Academy of Sciences of the United States of America* 103.21, pp. 8066–8071. ISSN: 0027-8424. DOI: 10.1073/pnas.0509932103.

Reppas, Christos et al. (2015). "Characterization of Contents of Distal Ileum and Cecum to Which Drugs/Drug Products are Exposed during Bioavailability/Bioequivalence Studies in Healthy Adults". In: *Pharmaceutical Research* 32.10, pp. 3338–3349. ISSN: 1573904X. DOI: 10.1007/s11095-015-1710-6.

Ryu, W S, R M Berry, and H C Berg (2000). "Torque-generating units of the flagellar motor of Escherichia coli have a high duty ratio." In: *Nature* 403.6768, pp. 444–447. ISSN: 0028-0836. DOI: 10.1038/35000233.

Sagawa, Takashi et al. (2014). "Single-cell E. coli response to an instantaneously applied chemotactic signal". In: *Biophysical Journal* 107.3, pp. 730–739. ISSN: 15420086. DOI: 10.1016/j.bpj.2014.06.017.

Sarkar, Mayukh K, Koushik Paul, and David F. Blair (2010). "Chemotaxis signaling protein CheY binds to the rotor protein FliN to control the direction of flagellar rotation in Escherichia coli." In: *Proceedings of the National Academy of Sciences of the United States of America* 107.20, pp. 9370–9375. ISSN: 0027-8424. DOI: 10.1073/pnas.1000935107.

Savageau, Michael A (1983). "Escherichia coli Habitats , Cell Types , and Molecular Mechanisms of Gene Control". In: 122.6, pp. 732–744.

Scharf, Birgit E., Karen A. Fahrner, and Howard C. Berg (1998). "Chez has no effect on flagellar motors activated by CheY(13DK106YW)". In: *Journal of Bacteriology* 180.19, pp. 5123–5128. ISSN: 00219193.

Schnitzer, M. (1993). " Theory of continuum random walks and application to chemotaxis". In: *Physical Review E* 48.4, 2553—2568.

Schnitzer, M. et al. (1990). "Strategies for chemotaxis". In: *Symp Soc Gen Microbiol* 46, pp. 15–33.

Schwarz-Linek, Jana et al. (2016). "Escherichia coli as a model active colloid: A practical introduction". In: *Colloids and Surfaces B: Biointerfaces* 137, pp. 2–16. ISSN: 18734367. DOI: 10.1016/j.colsurfb.2015.07.048. eprint: 1506.04562v1.

Segall, J E, S M Block, and H C Berg (1986). "Temporal comparisons in bacterial chemotaxis." In: *Proceedings of the National Academy of Sciences of the United States of America* 83.23, pp. 8987–8991. ISSN: 0027-8424. DOI: 10.1073/pnas.83.23.8987.

Sourjik, Victor and Howard C Berg (2002). "Receptor sensitivity in bacterial chemotaxis". In: *Proceedings of the National Academy of Sciences of the United States of America* 99.1, pp. 123–127. ISSN: 0027-8424. DOI: 10.1073/pnas.011589998.

— (2004). "Functional interactions between receptors in bacterial chemotaxis". In: *Nature* 428.March, pp. 1–4. ISSN: 0028-0836. DOI: 10.1038/nature02371.1..

Sowa, Yoshiyuki et al. (2005). "Direct observation of steps in rotation of the bacterial flagellar motor." In: *Nature* 437.7060, pp. 916–919. ISSN: 0028-0836. DOI: 10.1038/nature04003.

Sowa, Yoshiyuki and Richard M Berry (2008). "Bacterial flagellar motor". In: *Quarterly Reviews of Biophysics* 41.2, pp. 103–132. ISSN: 09609822. DOI: 10.1017/S003358350800469.

Stadmiller, Samantha S. et al. (2017). "Osmotic Shock Induced Protein Destabilization in Living Cells and Its Reversal by Glycine Betaine". In: *Journal of Molecular Biology* 429.8, pp. 1155–1161. ISSN: 10898638. DOI: 10.1016/j.jmb.2017.03.001.

Studdert, Claudia A. and John S. Parkinson (2004). "Crosslinking snapshots of bacterial chemoreceptor squads". In: *Proceedings of the National Academy of Sciences* 101.7, pp. 2117–2122. ISSN: 0027-8424. DOI: 10.1073/pnas.0308622100.

Suzuki, Hirofumi, Koji Yonekura, and Keiichi Namba (2004). "Structure of the Rotor of the Bacterial Flagellar Motor Revealed by Electron Cryomicroscopy and Single-particle Image Analysis". In: *Journal of Molecular Biology* 337.1, pp. 105–113. ISSN: 00222836. DOI: 10.1016/j.jmb.2004.01.034.

Tamar, Einat, Moriah Koler, and Ady Vaknin (2016). "The role of motility and chemotaxis in the bacterial colonization of protected surfaces". In: *Scientific Reports* 6.January, p. 19616. ISSN: 2045-2322. DOI: 10.1038/srep19616.

Thomas, D R, D G Morgan, and D J DeRosier (1999). "Rotational symmetry of the C ring and a mechanism for the flagellar rotary motor." In: *Proceedings of the National Academy of Sciences of the United States of America* 96.18, pp. 10134–9. ISSN: 0027-8424. DOI: 10.1073/pnas.96.18.10134.

Thomas, Dennis R. et al. (2006). "The three-dimensional structure of the flagellar rotor from a clockwise-locked mutant of Salmonella enterica serovar typhimurium". In: *Journal of Bacteriology* 188.20, pp. 7039–7048. ISSN: 00219193. DOI: 10.1128/JB.00552-06.

Tipping, Murray J. et al. (2013a). "Load-dependent assembly of the bacterial flagellar motor". In: *mBio* 4.4, pp. 1–6. ISSN: 21612129. DOI: 10.1128/mBio.00551-13.

Tipping, Murray J. et al. (2013b). "Quantification of flagellar motor stator dynamics through in vivo proton-motive force control". In: *Molecular Microbiology* 87.2, pp. 338–347. ISSN: 0950382X. DOI: 10.1111/mmi.12098.

Toker, A S and R M Macnab (1997). "Distinct regions of bacterial flagellar switch protein FliM interact with FliG, FliN and CheY." In: *Journal of molecular biology* 273.3, pp. 623–634. ISSN: 0022-2836. DOI: 10.1006/jmbi.1997.1335.

Tso, Wung-wai and Julius Adler (1974). "Negative Chemotaxis in Escherichia coli Negative Chemotaxis in Escherichia coli". In: 118.2, pp. 560–576.

Turner, L, W S Ryu, and H C Berg (2000). "Real-time imaging of fluorescent flagellar filaments." In: *Journal of bacteriology* 182.10, pp. 2793–801. ISSN: 0021-9193. DOI: 10.1128/JB.182.10.2793-2801.2000.Updated.

Ueno, T, K Oosawa, and S Aizawa (1992). "M ring, S ring and proximal rod of the flagellar basal body of Salmonella typhimurium are composed of subunits of a single protein, FliF." In: *Journal of Molecular Biology* 227.3, pp. 672–677.

Vaknin, Ady and Howard C Berg (2006). "Osmotic stress mechanically perturbs chemoreceptors in Escherichia coli." In: *Proceedings of the National Academy of Sciences of the United States of America* 103.3, pp. 592–596. ISSN: 0027-8424. DOI: 10.1073/pnas.0510047103.

Van Den Berg, Jonas, Arnold J. Boersma, and Bert Poolman (2017). "Microorganisms maintain crowding homeostasis". In: *Nature Reviews Microbiology* 15.5, pp. 309–318. ISSN: 1740-1526. DOI: 10.1038/nrmicro.2017.17.

Vladimirov, Nikita and Victor Sourjik (2009). "Chemotaxis: How bacteria use memory". In: *Biological Chemistry* 390.11, pp. 1097–1104. ISSN: 14316730. DOI: 10.1515/BC.2009.130.

Wadhams, George H. and Judith P. Armitage (2004). "Making sense of it all: bacterial chemotaxis". In: *Nature Reviews Molecular Cell Biology* 5.12, pp. 1024–1037. ISSN: 1471-0072. DOI: 10.1038/nrm1524.

Wang, E A et al. (1982). "Tandem duplication and multiple functions of a receptor gene in bacterial chemotaxis". In: *J Biol Chem* 257.9, pp. 4673–4676.

Wilson, L. G. et al. (2011). "Differential dynamic microscopy of bacterial motility". In: *Physical Review Letters* 106.1, pp. 7–10. ISSN: 00319007. DOI: 10.1103/PhysRevLett.106.018101. eprint: 1004.4764.

Wolfe, A J and H C Berg (1989). "Migration of bacteria in semisolid agar." In: *Proceedings of the National Academy of Sciences of the United States of America* 86.18, pp. 6973–6977. ISSN: 0027-8424. DOI: 10.1073/pnas.86.18.6973.

Wood, J M (1999). "Osmosensing by bacteria: signals and membrane-based sensors." In: *Microbiology and molecular biology reviews : MMBR* 63.1, pp. 230–262. ISSN: 1092-2172.

Wu, Jiongru et al. (1996). "The receptor binding site for the methyltransferase of bacterial chemotaxis is distinct from the sites of methylation". In: *Biochemistry* 35.15, pp. 4984–4993. ISSN: 00062960. DOI: 10.1021/bi9530189.

Yuan, Junhua and Howard C Berg (2008). "Resurrection of the flagellar rotary motor near zero load." In: *Proceedings of the National Academy of Sciences of the United States of America* 105.4, pp. 1182–5. ISSN: 1091-6490. DOI: 10.1073/pnas.0711539105.

Yuan, Junhua, Karen A. Fahrner, and Howard C. Berg (2009). "Switching of the Bacterial Flagellar Motor Near Zero Load". In: *Journal of Molecular Biology* 390.3, pp. 394–400. ISSN: 00222836. DOI: 10.1016/j.jmb.2009.05.039. eprint: NIHMS150003.

Yuan, Junhua et al. (2010). "Asymmetry in the clockwise and counterclockwise rotation of the bacterial flagellar motor." In: *Proceedings of the National Academy of Sciences of the United States of America* 107.29, pp. 12846–12849. ISSN: 0027-8424. DOI: 10.1073/pnas.1007333107.

Zhou, Jiadong, Scott A Lloyd, and David F Blair (1998). "Electrostatic interactions between rotor and stator in the bacterial flagellar motor". In: *Proceedings of the National Academy of Sciences of the United States of America* 95.11, pp. 6436–41. ISSN: 0027-8424. DOI: 10.1073/pnas.95.11.6436.